Synthesis and characterization of transition metal doped CdSe dilute magnetic nanostructures

A THESIS

Submitted to the

FACULTY OF SCIENCE

THAPAR UNIVERSITY, PATIALA

for the degree of

Doctor of Philosophy

By

JASPAL SINGH

Regn. No. 900912021

School of Physics & Materials Science

Thapar University

Patiala - 147 004

INDIA

April 2014

DECLARATION

It is certified that the thesis is entirely my own and that the ideas and references cited herein have been duly acknowledged.

(Jaspal Singh)

Attestation by supervisor

(Dr. N. K. Verma)

Senior Professor

School of Physics and Materials Science,

Thapar University,

Patiala – 147 004

INDIA

CERTIFICATE

This is to certify that the thesis entitled, "Synthesis and characterization of transition metal doped CdSe dilute magnetic nanostructures", submitted by Mr. Jaspal Singh in the fulfillment of the requirement for the award of the degree of Doctor of Philosophy in the School of Physics and Materials Science, Thapar University, Patiala, is a record of candidate's own work carried out by him under my supervision and guidance. The matter presented in this thesis has not been submitted in part or full for the award of any degree in any other University or Institute.

Attestation by supervisor

(Dr. N. K. Verma)

Senior Professor

School of Physics and Materials Science,

Thapar University,

Patiala – 147 004

INDIA

ACKNOWLEDGEMENT

This doctoral dissertation has been successfully completed with the support and encouragement of number of people.

First and foremost, I would like to express my sincere gratitude to my supervisor Dr. N. K. Verma for his precious advices, continuous guidance and patience. He is the first person who has given me a chance to explore the fascinating field of research especially nanoscience and nanotechnology. Apart from research, he inculcated in me the habit of being always positive even under adverse circumstances. Today I can decisively say that I am an entirely changed man – turned into a positive-thinking guy. I also extend my gratitude to Mrs. (Dr.) Rama Verma for her motherly affection and care.

I also express my sincere thanks to Dr. Sanjeev Kumar, PEC University of Technology, Chandigarh for his valuable suggestions, moral support and timely help.

I am grateful to Thapar University management for awarding me Teaching Associateship during my research work. I also gratefully acknowledge Defense Research & Development Organization (DRDO), India, for awarding me JRF and SRF as well as funds to carry out this research work.

I would like to thank my Doctoral Committee comprising Dr. S. D. Tiwari, Dr. B. N. Chudasama, Dr. Bonamali Pal for their encouragement, constructive comments and guidance through all these years.

I am obliged to Professor Prakash Gopalan, Director, for providing me the requisite facilities to carry out the research work. I would like to express my gratitude to Dr. Kulvir Singh, Head,

School of Physics and Materials Science, for his encouragement and full-hearted support. I am also thankful to the all faculty members of School of Physics and Materials Science for their time to time support and encouragement. I am also thankful to the technical and secretariat staff for their assistance.

I would like to thank my seniors Dr. Zinki Jindal and Dr. Sanjeev Kumar for their guidance, suggestions and inspiration.

My colleagues Dr. Gurmeet Singh Lotey, Lavanya Khanna, Dr. Manveen Kaur, Gitanjali Dhir, Kamaldeep Kaur and Sunil Kumar have always been a source of motivation, support, and laughter as well as fights throughout this journey. I am thankful to my friends Rohit Singh, Bhupinder Thakur and Inderpreet Singh Grover of School of Chemistry & Biochemistry (SCBC), Thapar University, for their help and good time which we have spent together. I am especially indebted to my friends Mr. Rampal Shukla and Mr. Harmanpreet Singh who were always there for moral support, whenever I felt exhausted or frustrated during the work.

My mother Mrs. Usha Rani's patience and support during all these years have been beyond measures. It is only due to her blessings that I could complete my PhD so successfully. At the same time, I am thankful to my brother, Rashpal Singh, for his love and cooperation.

Above all, I am obliged to Almighty God for giving me strength to complete this project smoothly and successfully as well as on time.

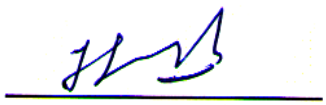

(Jaspal Singh)

CONTENTS

Chapter 3 Results & Discussions

LIST OF FIGURES

LIST OF TABLES

LIST OF PUBLICATIONS

I. SCI publications

1. Jaspal Singh, N. K. Verma, "Synthesis and characterization of Fe-Doped CdSe nanoparticles as dilute magnetic semiconductor", Journal of Superconductivity and Novel Magnetism **25** (2012) 2425-2430.
2. Jaspal Singh, N.K. Verma, "Ferromagnetism in Fe-doped CdSe nanorods prepared by solvothermal route", Journal of Materials Science: Materials in Electronics **24** (2013) 4464-4470.
3. Jaspal Singh, Sanjeev Kumar, N.K. Verma," Enhancement of room temperature ferromagnetism in $Cd_{1-x}Ni_xSe$ nanoparticles", Journal of Materials Science: Materials in Electronics **25** (2014) 2267-2272.
4. Jaspal Singh, N.K. Verma, "Structural, optical and magnetic properties of cobalt-doped CdSe nanoparticles", Journal of Bulletin of Materials Science **37** (2014) 1-7.
5. Jaspal Singh, Sanjeev Kumar, N.K. Verma," Effect of Ni-doping concentration on structural, optical and magnetic properties of CdSe nanorods", Journal of Material Science in Semiconductor Processing **26** (2014) 1-6.

II. Other SCI publications (research work done during PhD but not included in the objectives)

1. Jaspal Singh, G. S. Lotey, N. K. Verma, "Structural, optical and magnetic properties of Cr- doped CdSe nanoparticles", Digest Journal of Nanomaterials and Biostructures **6** (2011) 1733-1740.
2. Gurmeet Singh Lotey, Jaspal Singh, N. K. Verma, "Room temperature ferromagnetism in Tb-doped ZnO dilute magnetic semiconducting nanoparticles", Journal of Materials Science: Materials in Electronics **24** (2013) 3611-3616.

III. Non-SCI publications

1. Jaspal Singh, N.K. Verma, "Surfactant induced phase control of CdSe nanoparticles", AIP Conference Proceedings **1536** (2013) 43-44.
2. Jaspal Singh and N. K. Verma, "Room temperature ferromagnetism in CdSe nanorods", Excel India Publishers (2013) 2143-2148.

IV. Paper communicated

1. Jaspal Singh, N.K. Verma, Structure dependent ferromagnetism in cobalt doped CdSe nanorods, Physica E: Low dimensional systems and structures, Elesvier.

V. Papers in Conference Proceedings:

1. Jaspal Singh and N. K. Verma, "Room temperature ferromagnetism behavior of Cr-doped CdSe nanoparticles" Proceedings of national conference on Recent Advances in Polymer Nanocomposites, January 14-15, 2011, Organised by Department of Physics, Zakir Hussain College, University of Delhi, New Delhi, India, p. 55.
2. Jaspal Singh and N. K. Verma, "Optical and magnetic properties of cobalt doped CdSe dilute magnetic nanoparticles", 4th Bangalore Nano Conference, December 8-9, 2011, Organized by JNCASR, p. 84.
3. Jaspal Singh and N. K. Verma, "Magnetic study of Fe-doped CdSe nanoparticles", 23rd Annual general meeting, Materials Research Society of India (MRSI), February 13-15, 2012, Organized by Thapar University, Patiala, India, p. 64.
4. Jaspal Singh and N. K. Verma, "Structural, optical and magnetic study of Fe-doped CdSe nanoparticles", (ICWNCN) International Conference and Workshop on

Nanostructures Ceramics & Other Nanomaterials, March, 13-16, 2012, organized by Delhi University, Delhi, India, p. 437.

5. Jaspal Singh and N. K. Verma, "Room temperature ferromagnetism in Ni-doped CdSe nanoparticles", International Conference on Nanotechnology in the Service of Health, Environment & Society, February 13-15, 2014, Organized by Panjab University, Chandigarh, India, p. 50.

ABSTRACT

Spintronics represent field of electronics, in which the spin of electron is exploited along with its charge. DMS materials are promising for future spintronic device applications. A lot of research has been devoted to generate magnetism in semiconductor materials via doping of transition metals, known as DMS materials. However, origin of magnetism remains still debatable till date. Also, from the application point of view, low Curie temperature (T_C) further hinders their practical utility, and thus, many efforts have been made to find ferromagnetic DMS having T_C higher than room temperature. This has motivated us to carry out investigations in order to achieve ferromagnetism at room temperature and understand its origin, as well.

In the present thesis work, synthesis of pure CdSe and Fe, Ni, and Co-doped CdSe nanostructures (nanoparticles and nanorods) have been carried out by chemical route. Their structural, morphological, elemental, optical and magnetic properties have been studied using various characterization techniques such as XRD, Raman spectroscopy, TEM, EDS, PL, UV-visible, ESR and VSM/SQUID. The observations and their possible origins have been discussed in detail. Magnetic study revealed presence of room temperature ferromagnetism in both pure and doped CdSe nanostructures. However, observation of weak ferromagnetism in CdSe nanostructures is ascribed to defects and small particle size. Nature of dopant and its concentration both have been found to play a crucial role in deciding the overall magnetic behavior of the system and is attributed to exchange interactions between dopant ions.

PREFACE

This thesis presents the synthesis and characterization of transition metal doped CdSe nanostructures by chemical synthesis route. The structural, optical, morphological and magnetic properties of the synthesized nanostructures have been observed using various characterization techniques. The possible origin of magnetism has been discussed in detail. The chapter-wise description of the thesis has been given below:

Chapter 1 gives an introduction to the need and importance of DMS materials. A brief of various mechanisms or theories discussing the origin of magnetism in DMS materials have been included in this chapter. The literature review has been given along with motivation to carry out this work. CdSe emerges as a potential candidate as a DMS material. It also provides information regarding the materials and their properties used in the present work.

Chapter 2 it describes the synthesis procedure adopted for pure and Fe, Ni, and Co-doped CdSe nanostructures (nanoparticles and nanorods). Also, it includes various characterization techniques employed for the study of doped CdSe nanostructures as DMS material. The introduction, theory, instrumentation, working and applications of each characterization technique have been described in detail.

Chapter 3 presents results and their discussions for Fe, Ni and Co-doped CdSe nanostructures (nanoparticles and nanorods). The synthesized nanostructures have been characterized through XRD, TEM, EDS, UV-visible, PL spectroscopy, Raman spectroscopy, ESR and VSM/SQUID. The origin of magnetism has been discussed in detail. The magnetic analysis leads to the conclusion that there are different reasons for observed ferromagnetism in doped CdSe nanostructures depending on the type of dopant used.

Chapter 4 includes conclusion of the research work undertaken along with achievements and future scope of the work.

Chapter 1

Introduction

Chapter 1

Introduction

This chapter gives an introduction to the need and importance of DMS materials. A brief of various mechanisms or theories discussing the origin of magnetism in DMS materials have been included in this chapter. The literature review has been given along with motivation to carry out this work. CdSe emerges as a potential candidate for DMS materials.

1.1 Moore's law

In December 1947, invention of the transistor by William Shockley, John Bardeen and Walter Brattain at Bell Laboratory began a new era of solid-state electronics by controlling the flow of charge carriers (electrons or holes) [1]. The tremendous progress in the integrated chip (IC) design technology having transistor as a basic component been made by microelectronics industry. It has been successfully used in different applications, such as data storage, sensors and electronic devices. The extensive use of semiconductors and the demand for cheaper, faster and more compact electronic devices have increased dramatically over the past few decades. The miniaturization of electronic devices with growing demand has been made possible by the lithographic patterning technique [2]. In 1965 Gordon Moore, predicted that the number of transistors would be doubled on an IC chip in every 18 months resulting from the miniaturization of electronic devices [3]. However, miniaturization results in physical limits of the currently used materials and we are approaching towards atomic scale dimensions. Under such circumstances it would not be possible to continue Moore's law in future with present technology. On the other

hand magnetic materials are used for information storage due to their capability to preserve the magnetization in a fixed direction without power supply (non-volatile memory). Magnetic materials, such as ferromagnetic materials, are the key materials for memory elements in writeable and readable heads. In order to overcome above problems spintronics emerges as a new hope for microelectronics industry [4, 5]. The idea is to combine the magnetic and semiconducting properties into a single material which would result in the generation of new devices that are smaller, energy efficient, non-volatile and much faster as compared with existing one at present.

1.2 Spintronics

Spintronics is spin based electronics, in which researchers are trying to exploit the spin of electron along with its charge in one spintronic device [6, 7]. The data can be stored in particular spin orientation (up or down), which can be carried out by the electrons as spin is attached with it and finally the data can be read at other terminal. At present, electronic devices processed the information by semiconductor chips and magnetic disk drives are used to store the information. The future technology devices may possibly be based on spintronics, i.e., both semiconductivity (charge to carry information) and magnetism (spin to store information), combined in one device. But the major challenges in the field of spintronics are injection, transport, and detection of spin-polarization as well as spin-polarized currents from ferromagnetic material into semiconductor in spintronics devices. The resistance mis-match between ferromagnetic/semiconductor interface, hinders the effective spin injection and therefore, much of interest has been focused on the development of ferromagnetism in semiconductor materials, which is commonly known as dilute magnetic semiconductor (DMS) materials.

The significance achievement in the area of spintronics is Giant Magneto Resistance (GMR) effect discovered by Abert Fert and Peter Grunberg in 1988 [8, 9]. The change in electrical resistance of some materials in response to an applied magnetic field is known as magneto resistance but when magnetic field is applied to thin films composed of alternate ferromagnetic and non-ferromagnetic layers such as Fe/Cr, a large change in resistance has been observed known as GMR effect. The GMR effect and the theoretical model of Datta-Das field effect transistor in 1990 [10], further revolutionized the minds of researchers to quest for suitable materials for read and write head memory devices and DMS materials are very promising in this regards.

1.3 Dilute magnetic semiconductor

The idea is to use materials joining both the characteristics of semiconductors and magnetic materials, known as Dilute Magnetic Semiconductors (DMS) or sometimes referred to as semimagnetic semiconductors for electronic and memory elements [11].

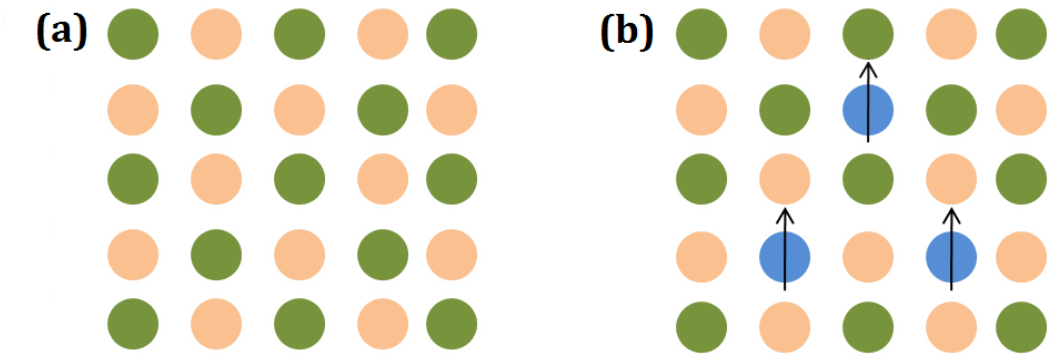

Figure 1.1 (a) Non magnetic host semiconductor material and (b) DMS material; where blue dots having arrows represent the magnetic dopant atoms

DMS are semiconducting materials in which a fraction of host cations can be substitutionally replaced by transition metal (Fe, Ni, Co etc) or appropriate rare earth elements (Gd, Tb etc) as shown in Figure 1.1. In recent years, DMS have emerged as a much researched field due to the possibility of manipulating charge and spin degree of freedom of electron. DMS materials are believed to be the ideal candidate for spintronic applications. There are two major criteria for selecting the most promising materials for semiconductor spintronics [12]. Firstly, ferromagnetism should be retained to practical temperatures (i.e. $\geq$ 300 K). Secondly, it would be a major advantage if there were already an existing technology base for the material in other applications.

1.4 Mechanisms (or theories) explaining the magnetism in DMS materials

Till date the origin of magnetism remains controversial in DMS materials. The various mechanisms (or theories) have been proposed in order to explain the origin of magnetism in these DMS materials and are summarized below.

1.4.1 Ruderman-Kittel-Kasuya-Yosida (RKKY)

The indirect exchange interaction between magnetic dopant ions and delocalized conduction band electrons of host material is known as RKKY type exchange interactions [13, 14]. The d-orbital electrons of dopant interact via conduction band electrons of host, giving rise to ferromagnetism or antiferromagnetism depending on distance between two dopant ions. These are dominant exchange inter actions in metallic ferromagnets and can be used to explain the magnetism in DMS materials which possess high delocalized carrier density. The magnitude of RKKY exchange interactions can be estimated from the following equation [15],

$$J(r) \sim \frac{\cos(2k_F \cdot r)}{r^3}$$

Where *J(r)* is the exchange interaction constant, k_F is the Fermi wave vector, and r is the distance between two ions. The exchange constant J(r) is oscillatory in nature and acquires positive (ferromagnetism) or negative (antiferromagnetism) values depending on distance between the dopant ions. The spin glass behavior in DMS materials can also be understood by RKKY type exchange interactions.

1.4.2 Double exchange interactions

The double exchange interactions have been proposed by Zener in 1951, in order to explain the ferromagnetism in manganite materials [16]. Double exchange interactions demand magnetic ions in different charge states interact via hopping of electron from one ion to other (two neighboring magnetic ions). The spin flips are not allowed in this mechanism. This mechanism can also be used to explain the ferromagnetism in DMS materials [17]. In DMS materials, TM having different charge state interacts through p-orbital of host semiconductor via hopping of electron as shown in Figure 1.2. This interaction leads to the observed ferromagnetism in DMS materials.

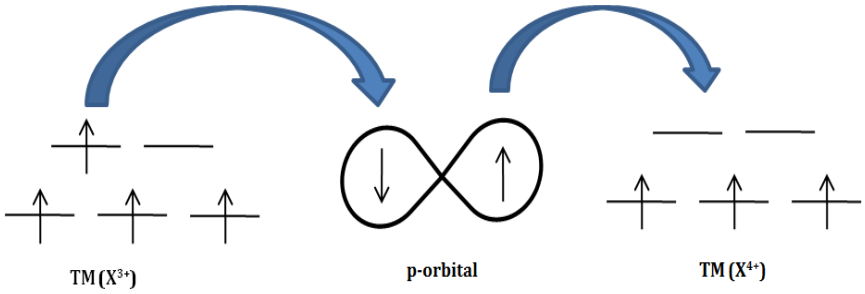

Figure 1.2 Schematic representation of double exchange mechanism in DMS materials [16].

1.4.3 Super exchange interactions

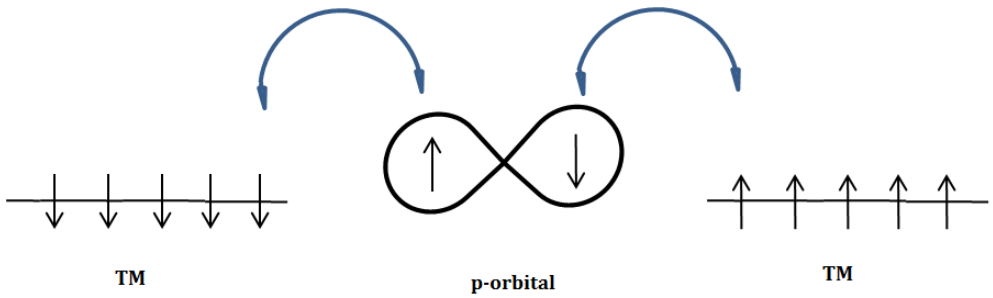

Figure 1.3 Schematic representation of superexchange mechanism in DMS materials [18, 19].

This mechanism was first proposed by Krammers in 1934 [18] and further detailed study was conducted by Anderson in 1950 [19]. In this mechanism the spins of half filled d-shell electrons of TM ions interact with completely filled p-orbitals of host semiconductor as shown in Figure 1.3. The spatial distribution of spins according to Pauli's exclusion principle leads to opposite spins of d-shell electrons of TM ions, which results in antiferromagnetism in a given DMS material.

1.4.4 Bound magnetic polaron (BMP)

BMP is a magnetization cloud formed by the exchange interactions of charge carriers (e^- or h^+) at the vicinity of dopant in host semiconductor material. The overlapping of large number of neighboring BMPs led to long-range ferromagnetic ordering in DMS materials. Recently, Coey et al. [20] proposed BMP model for the observed magnetism in oxides based DMS materials as shown in Figure 1.4. The small circles show cation ions of host oxide and square shows oxygen vacancy. The circles marked by arrow are magnetic dopant atoms. The charge carriers (e^- or h^+)

are trapped in the vacancy sites and magnetic dopant interact via trapped charge carriers which result in effective magnetic field. This tends to align nearby charge carriers in their direction, resulting in the formation of BMP. Further, BMPs may overlap with each other (Figure 1.4) resulting in ferromagnetic ordering in DMS materials.

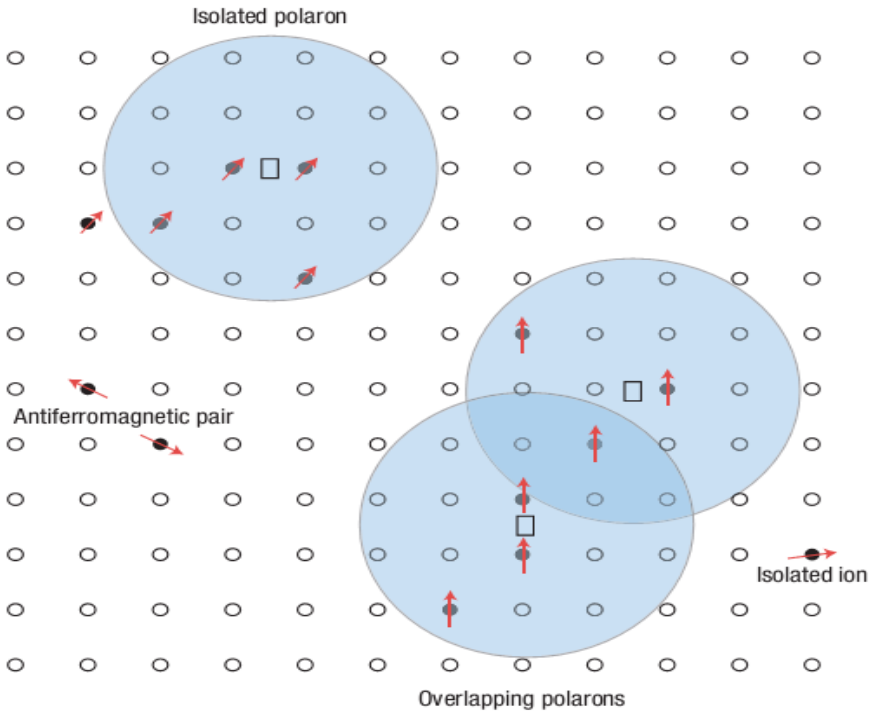

Figure 1.4 Schematic representation of BMP mechanism in DMS materials [20]

1.5 Literature review

The literature was reviewed in detail in order to learn and gather optimum information as to the genesis and the technical applications of work and is given as under:

The first report on ferromagnetic and semiconducting properties of $CrBr_3$ was reported in 1960 but T_c was found to be very low about 37 K. After this, studies on various materials like EuO,

MnAs, MnSb, $CdCr_2S_4$, Sr_2FeMnO_6, Fe_3O_4, $YTiO_3$, $SeCuO_3$, $BiMnO_3$, have been reported, but a little improvement in T_c was found [21].

Dietl et al. [22] in 2000 theoretically proposed number of materials that can show DMS behavior. But, p-type GaN and ZnO semiconductor doped with 5% Mn shows room temperature ferromagnetism. After this prediction, number of reports were published on room temperature ferromagnetic behavior of different materials ; III-V compounds (Ga,Mn)As, (In,Mn)As, (Ga,Mn)P, (Ga,Mn)N, II-VI compounds (Zn,Mn)Se, (Zn,Cr)Te, (Zn,Cr)Se, (Cd,Mn)Te, (Cd,Mn)Se, IV-VI compounds (Pb,Mn)Te, (Pb,SnMn)Te, VI compounds GeMn, (Si,Mn)C, and Oxides ZnO, TiO_2, SnO_2, Cu_2O [12, 23-25].

The group II-VI and III-V based doped semiconductors are potential candidates for spintronic applications. DMS based on III–V semiconductors have attracted a great deal of attention because of their compatibility with existing electronic technology. The lower solubility of transition metal in these semiconductors further hampered their utility in practical applications. The non-equilibrium growth techniques such as molecular beam epitaxy (MBE) and chemical vapour deposition (CVD) were used to incorporate transition metal in given III-V based host semiconductor material. However, limited percentage of doping could be achieved in these semiconductor materials and the highest T_c obtained are $T_C \sim 5$ K for (In,Mn)As [26], $T_C \sim 110$ K for (Ga,Mn)As [27] and, very recently, a report of $T_C \sim 940$ K for (Ga,Mn)N [28]. Also, there are reports on the doping with other transition metal ions in III-V nitride materials, such as Mn-doped AlN [29], Cr-doped GaN [30], Cr-doped AlN [31, 32], Co-implanted GaN [33], Fe-implanted p-type GaN epilayer [34], Gd-doped GaN films [35], and V-doped GaN [33]. Moreover, for III–V DMS, ferromagnetism with T_C often above room temperature has been

found in several other DMS, including $Ge_{1-x}Mn_x$ [36], $Ti_{1-x}Co_xO_2$ [37], and $Zn_{1-x}Co_xO$ [38]. The major challenges in III-V doped semiconductor is lower solubility of transition metals in these host semiconductor materials, lower T_c values and origin of observed magnetism. These are very important materials in industry for applications in electronics, light emitting diodes, laser etc. In the end of 1990 thin films were grown by molecular beam epitaxy (MBE). Previously it was not possible to add magnetic impurity in III-V semiconductor beyond their solubility limit of 10^{18} cm^{-3} but it has now become possible to go beyond solubility limit with these newly developed techniques like MBE, metal-organic chemical vapour deposition (MOCVD), chemical vapour deposition (CVD), radio frequency sputtering (rf-sputter). But these synthesis techniques are very costly, time consuming process, required high purity precursors, and high vacuum system for the growth [39].

However, II–VI compounds such as CdTe, ZnSe, CdSe, CdS doped with Mn substituting their original cations are the most common DMS studied in early period of this field. The low T_c and difficulty in doping make these II–VI-based DMS materials less attractive for applications [11]. The conventional III–V semiconductors on the other hand have been widely used for high speed electronic and optoelectronic devices. Rare-earth and transition-metal-doped II-VI semiconductors such as CdS, ZnS, CdSe, ZnSe, CdTe and ZnTe based nanostructures are current interest of research, because of their unique optical and magnetic properties. Doping of such nanostructures with rare-earth or transition-metal ions will, in particular, allow an additional control of their optical properties by magnetic field and vice-versa.

But the major hindrance for practical implementation of spin concepts is the difficulty in preparing suitable materials with desired properties, which can serve as a high efficiency source

of charge carriers with well defined spin, yet be compatible with existing semiconductor technologies.

In the past few decades, numbers of researchers are working to find suitable materials as DMS. The much of the work has been done on II-VI semiconductor nanoparticles doped with magnetic impurities. The semiconducting materials such as CdSe [40], CdS [41], ZnSe [42], ZnS [43], CdTe [44], ZnTe [45] doped with transition or rare earth metal ions are the most promising DMS materials. Among these, the extensive research has been focused on CdSe nanomaterial as a host, and doping of suitable ions such as transition metal to explore its DMS behavior [40]. CdSe nanoparticles being a direct band gap semiconductor shows very interesting properties such as energy band gap tuning, optical, electronic, and electrical properties just by varying its dimensions and addition of suitable dopant.

In the 1970 Robert R. Galazka group report, the growth of II-VI alloys [46]. The various properties such as magneto-optical and magneto-transport were studied. But, T_c was found to be very low. These materials shows other interesting properties such as tuning of energy gap by addition of suitable dopant, magneto-optical effects, exchange interactions, spin glass behavior, giant Zeeman splitting, Faraday rotation.

Furdyna et al. [47] in 1982 reported the interface in semiconductors physics and magnetism presented in DMS, the ternary semiconductors alloys like $Cd_{1-x}Mn_xTe$ and $Hg_{1-x}Mn_xTe$ displays variation in energy band gap and effective mass with change in composition. But it has been observed that the substitution of magnetic ions in these alloys leads to spin-spin exchange interaction between localized magnetic moments and band electrons. This results in extremely large, temperature dependent g-factors of electrons and holes; in gigantic values of Faraday

rotation; in anomalously large negative magneto resistance; and formation of bound magnetic polaron.

Furdyna et al. [48] in 1986 reported the different issues like, crystallography, band structure, optical, electrical and magnetic properties of ternary alloys of $A^{II}_{1-x}Mn_xB^{IV}$ type dilute magnetic semiconductors. The special attention was paved to novel effects arise from selective enhancement of spin dependent properties due to interaction between localized magnetic moments and band electrons. The exchange interaction can be controlled by controlling impurities and defects in DMS.

Furdyna et al. [11] in 1988 described, the cause of magnetism in $A^{II}_{1-x}Mn_xB^{IV}$ based alloys. The Mn^{2+}-Mn^{2+} exchange interactions lead to spin glass behavior, antiferromagnetic order, giant Faraday rotation, bound magnetic polaron. Also, various nanostructures such as quantum wells, super-lattices, and hetrostructures were successfully prepared. The metal-insulator-semiconductor structure of $A^{II}_{1-x}Mn_xB^{IV}$ involve two dimensional electron gas, results in interesting effects like the Shubnikov de-Haas oscillations, splitting of Landau levels, quantum hall effect. The electronic, optical, magnetic properties of quantum wells and super-lattices were also quite different from their bulk counterpart, but the major problem with these structures is that they are substantially grown on each other which lead to strain in these structures which affect their properties.

After 1990, the developments in chemical techniques such as solvothermal/hydrothermal [49-51], microemulsion [52, 53], sol-gel [54], colloidal [55, 56], template-assisted [57, 58] microwave [59, 60] etc. leads to synthesis of nanostructures. These techniques are simple, cost

effective and nanostructures of different morphologies have been synthesized by controlling reaction parameters.

Mikulec et al. [61] in 2000 described, the problem related doping of transition metals in II-VI compound semiconductors nanocrystals. The spectroscopic analysis of Mn-doped CdSe nanocrystals has been done. EPR study revealed that the most of dopant atoms reside on the surface layers of inorganic lattice. The optical study gives that Mn-doped CdSe quantum dot behaves like undoped quantum dot in the presence of external magnetic field because of interaction of electron/hole spin with paramagnetic impurities.

Hanif et al. [62] in 2002 reported the magnetic ordering in Co-doped CdSe DMS quantum dots. The structural and magnetic properties of Co-doped CdSe quantum dots were elaborated. The super paramagnetic behavior of quantum dots (QDs) were observed due to the antiferromagnetic (AFM) interactions which can be arise between Co spins in an isolated particle (intra-particle) or AFM interactions between spins in neighboring particles (inter-particle).The enhanced values of exchange integral by an order of magnitude in QDs compared to bulk, may be due to resulting from an increase in Co d-orbital overlap with CdSe valence band minimum. The correlation of studies suggest that the observed enhancement in magnetic super-exchange interactions between Co^{2+} dopant ions in CdSe quantum dots are due to changes in nature of coupling in size-restricted materials.

In 2003, Jian et al. studied that dynamic magnetic properties of $Cd_{1-x}Mn_xSe$ dilute magnetic semiconductor [63]. EPR spectra revealed that the interactions between the Mn-Mn dopants are enhanced and spin coherence length is improved due to quantum confinement effect in quantum dots.

Meulenberg et al. [64] in 2004 reported the electronic and chemical structure of Cu-doped CdSe nanocrystals by employing X-ray absorption near edge spectroscopy (XANES). This study revealed that in the local environment of Cu, in CdSe it exist in +1 oxidation state, which leads to charge imbalance. The charge imbalance present in Cu-doped CdSe nanocrystals induces defects and PL spectra get quenched as doping concentration is increased.

Magana et al. [65] in 2006 reported the super paramagnetic behavior of Mn-doped CdSe quantum dots. After thermal annealing, as grown Mn^{2+} doped of CdSe quantum dots from a cubic single source precursor that is super paramagnetic in nature with a blocking temperature of 40 K. But before thermal annealing, the 4 nm Mn-doped CdSe (1% Mn) quantum dots show paramagnetic behavior between 300 and 2 K, with a weak antiferromagnetic exchange. With thermal annealing, quantum dots show high-temperature ferromagnetic exchange. The switching-on of super paramagnetic behavior is due to migration and formation of $(Se\text{-}Mn\text{-}Se\text{-}Mn\text{-}Se\text{-}Mn)_n$ centers within nanocrystals that exhibit coupled magnetic moments.

Archer et al. [66] in 2007 reported the sp-d exchange interactions which are responsible for magnetism in Mn^{2+} and Co^{2+} doped CdSe quantum dots.

The doping and existence of giant excitonic Zeeman splitting in both Mn^{2+} and Co^{2+} doped CdSe quantum dots were demonstrated by magnetic circular dichroism spectroscopy (MCD). The study confirmed that such transition metal doped CdSe nanocrystals are promising candidates for studying the spin based effects and are relevant to spin based information storage processing.

Singh et al. [67] in 2008 presented the room temperature ferromagnetism in thiol-capped CdSe nanoparticles. Also, the effect of Cu doping on magnetic properties CdSe nanoparticles has been

explored. The well defined hysteresis loop with saturation magnetization has been observed for pure thiol capped CdSe nanoparticles at room temperature. But with the addition of Cu ions in CdSe, saturation magnetization increases at low concentration, then decreases consistently with increases in doping concentration. At higher concentration of dopant ≈17.2% the magnetization decreases due to direct exchange interaction between Cu-Cu ions which leads to antiferromagnetic character. Also, the observed magnetization does not vary with temperature range 300-420K.

Beaulac et al. [40] reported the spin based electronics and photonics properties of Mn^{2+} doped CdSe quantum dots. The paper describes progress in Mn^{2+} doped CdSe quantum dots; in development of free standing colloidal, basic electronic properties, self assembly on nanocrystals, photoluminescence properties and giant Zeeman splitting. The effect of size on various physical, chemical, and magnetic properties was presented. It has been found that photon polarization in Mn^{2+} doped CdSe quantum dots can be converted to electron spin polarization and polarized spins recombine to yield circularly polarized photons. Such transduction functionality represent that these quantum dots are basic building blocks of spin-electronics, spin-photonic, or spin-optoelectronic.

Seehra et al. [68] observed size dependent ferromagnetism in trioctylphosphineoxide (TOPO) capped CdSe quantum dots. The ferromagnetic behavior of these quantum dots is due to charge transfer from Cd ion d-band to oxygen atoms of TOPO.

Sudaresan et al. [69] in 2009 shows room temperature ferromagnetism in various different types of nanoparticles such as oxides; CeO_2, TiO_2, Al_2O_3, MgO, nitrides; GaN, chalcogenides; CdS, CdSe, superconductors; $YBa_2Cu_3O_7$. It has been found that the room temperature

ferromagnetism is universal in nanoparticles of inorganic materials. Till date there is no complete theoretical model which can explain the mechanism of observed magnetism into these DMS materials.

Singh et al. [70] presented the optical and magnetic properties of Fe substituted CdSe nanoparticles. Mossbauer and EPR confirmed that Fe presented in +3 oxidation state in CdSe. The CdSe nanoparticles capped with thiol showed room temperature ferromagnetic behavior. The saturation magnetization in Fe-doped CdSe nanoparticles increases upto 8.58 % dopant concentration. With further increase in Fe concentration ferromagnetic to paramagnetic behavior has been observed. Also, with change in temperature the magnetization first increases upto 100 K and then decreases upto 200 K, after this saturation magnetization becomes constant. Magnetic behavior of Fe-doped CdSe nanoparticles have been explained on the basis of F-centre exchange mechanism i.e. bound magnetic polarons, charge imbalance, defects.

Sunil et al. [71] 2010 observed room temperature ferromagnetism in Ni-doped CdSe nanoparticles synthesized by wet chemical precipitation method. The magnetic studies revealed that pure CdSe nanoparticles exhibit diamagnetic behavior at 300 K, whereas 5% Ni doped CdSe nanoparticles shows mixed behavior posses both paramagnetic and ferromagnetic character.

Meulenberg et al. [72] reported surface manipulation of magnetic properties of CdSe quantum dots. The comparison of three surfactants such as hexadecylamine (HAD), trioctylphosphine-oxide (TOPO), and dodecanenitrile (DDN) were studied using XANES, superconducting quantum interference device magnetometry (SQUID) and x-ray magnetic circular dichroism (XMCD) techniques. They give the evidence that a π-backbonding mechanism between surface

Cd atoms and organic surfactants were responsible for observed magnetism in capped CdSe quantum dots.

Jun et al. [73] presented the first principle based theoretical investigation on Ti, V, Cr doped CdSe within generalized gradient approximation for the exchange-correlation function based density functional theory. It has been observed that the Cr and Mn-doped CdSe show half-metallic ferromagnetic behavior with 100 % spin polarization at Fermi level.

Zheng et al. [74] in 2011 reported the size dependent magnetism in Mn-doped CdSe quantum dots. Antiferromagnetic to superparamagnetic behavior has been observed with decrease in size of quantum dots from 5.8 to 2.8 nm. They found that surface capping layer induced charge carrier concentration play a vital role in the observed magnetic behavior of CdSe quantum dots. The increase of carrier concentration with decrease of quantum dot size leads to the onset of superparamagnetism in Mn-doped CdSe quantum dots, which can be explained by carrier mediated RKKY type of exchange interactions.

Li et al. [75] synthesized the Co-doped CdSe nanowires. The weak sp-d exchange interactions as compared with quantum dots has been observed, which can be attributed to large diameter of synthesized nanowires ($D_{average}$ = 14 nm). However, anomalous photoluminescence properties of doped nanowires have been observed with temperature as compared to undoped one.

Kumar et al. [76] in 2011 observed the weak room temperature ferromagnetism in pure and Ni-doped CdSe nanorods synthesized by solvothermal route.

Fainblat et al. [77] in 2012 developed Mn-doped CdSe quantum well nanoribbons. The exchange interaction constants ($N_0\alpha$ and $N_0\beta$) have been calculated using magnetic circular spectroscopy.

The giant Zeeman effect (g-factor ≈ 13) has been observed at room temperature which indicate the presence of strong exchange interactions in Mn-doped CdSe quantum well nanoribbons, making them a potential candidate for spintronic applications.

1.6 Challenges with DMS and research motivations

The doping of transition metals that have partially filled d-states (Sc, Ti, V, Cr, Mn, Fe, Co, Ni, and Cu) and rare earth elements that have partially filled f-states (e.g. Eu, Gd, Er) have been used as magnetic atoms in DMS materials. The combination of both these properties (semiconducting as well as magnetic) in a single material called DMS leads to interesting properties like magneto-resistance, magneto-optical effect, spin manipulation and quantum hall effect. DMS are very promising materials for future device applications which find technological importance and help to understand basic fundamentals. The transition metal doped CdSe semiconductor nanoparticles are found to be a one of promising candidate for spintronic applications.

But from application point of view, low T_c of the investigated DMS represents serious challenges, and many efforts have been devoted to find ferromagnetic DMS with T_C higher than room temperature. To use DMS materials for spintronics applications the high T_c is still a challenging task, because of their complex mechanism to understand magnetic behavior. This has motivated us to carry out investigations in order to achieve and understand the observed magnetism in DMS materials.

1.7 CdSe nanostructures as potential DMS material

The nanomaterials have attracted a great attention due to their size dependent physical, chemical, magnetic, electronic, optical and biological properties which arise due to large surface to volume ratio and quantum confinement. The nanomaterials of different morphologies have been synthesized including dots, wires, rods, rings, CNTs, thin films and various other shapes [78-81]. These nanostructures with different morphologies are very promising for a variety of technological applications [82-84].

CdSe is one of the most important II-VI semiconductor materials and has exclusive physical properties such as direct band gap of 1.74 eV (bulk) and electron mobility of 450-900 cm^2/Vs. It is a n-type semiconductor material, which finds applications in IR optics, polarizers, and beam splitters. The current research has been focused on CdSe nanostructures because of their interesting optical, electrical, magnetic properties and potential applications in field effect transistors (FETs), solar cells, biological labeling, DMS, and luminescent devices [85-88]. A variety of nanostructures has been synthesized such as quantum dots, nanoparticles, nanorods, nanowires, tetrapods and branched shaped [89-92]. These nanostructures show interesting shape and size dependent properties as compared to their bulk counterpart, for example in CdSe quantum dots, luminescent emission can be tuned from blue to red as shown in Figure 1.5, depending upon the radius of quantum dots. The quantum effect comes into picture when radius of quantum dots becomes less than the Bohr exciton radius (for CdSe 5.5 nm) for a given material.

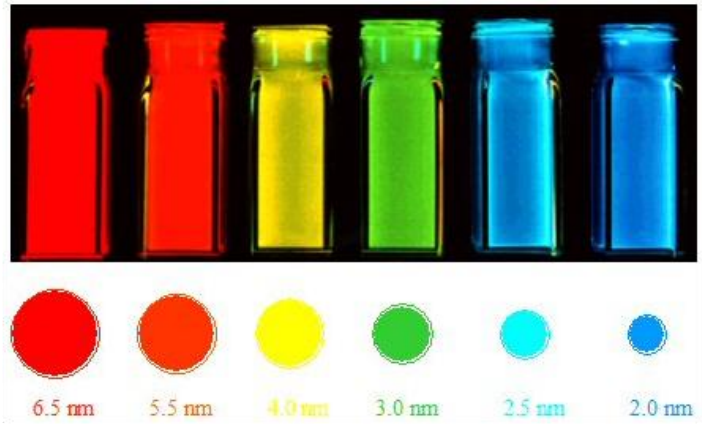

Figure 1.5 Pictorial view of quantum confinement effect in CdSe quantum dots [93]

Recently, induced magnetism has been observed in CdSe nanoparticles, which can be attributed to a variety of sources such as dangling bonds, surface ligands (or capping agent), dopant and defects. The magnetic behavior of CdSe nanoparticles can be enhanced by variation of functional group of surface ligand (or capping agent). The synthesis of DMS nanostructures are of great interest as semiconducting and magnetic properties are combined in one nanostructure. Therefore, ordered arrays of nanometer-sized magnetic semiconductors are promising components for magneto or spin electronics (e.g., magnetic hard disk media, non-volatile computer memory chips) devices. The miniaturization of these DMS materials lead to zero, one, or two-dimensional nanostructures, i.e., quantum dots, quantum wires, and quantum wells.

It has been found that electronic as well as magnetic properties of such DMS nanostructures are affected by reduced dimensionality. The understanding of change in the magnetic behavior at reduced dimensions is essential for device miniaturization. However, little efforts have been extended in research associated with room temperature ferromagnetism study on transition metal doped CdSe nanostructures. To date, there is no universal model which could explain the

possible cause of magnetism in doped CdSe nanostructures; and still it is unsolved mystery in the scientific community.

1.7.1 CdSe Crystal Structures

CdSe crystallizes into three forms: wurtzite (hexagonal), sphalerite (cubic, zinc blende), and rock-salt (cubic) [94]. The sphalerite structure is unstable and moderate heating is required to convert it into wurtzite structure. The transition starts at about 130 °C and is completed at about 700 °C, within one day. The rock-salt structure is only observed under high pressure. The crystal structures are given below and various properties have been tabulated in Table 1.1.

1.7.1.1 Wurtzite Crystal Structure

The name wurtzite crystal structure has been derived from mineral wurtzite. The wurtzite structure is a member of hexagonal crystal system and Figure 1.6 (a) shows the wurtzite (hexagonal close-packed or hcp) structure of CdSe.

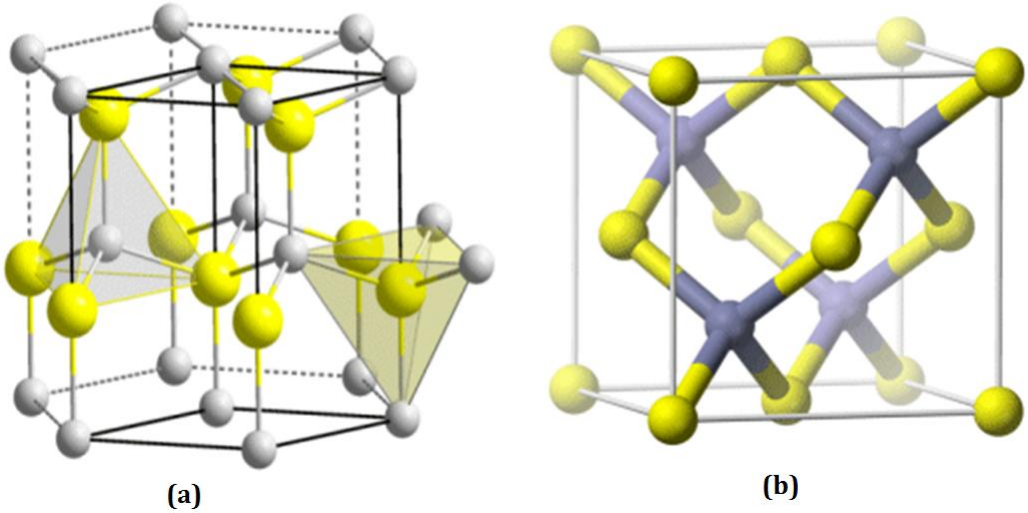

Figure 1.6 (a) Wurtzite crystal structure and (b) Zinc blende crystal structure of CdSe [95, 96]

The atoms of cadmium and selenium are tetrahedrally coordinated with each other that are stacked in an ABABAB pattern.

1.7.1.2 Zinc Blende Crystal Structure

Figure 1.6 (b) shows the zinc blende structure of CdSe, which is a member of cubic closed packing (ccp) crystal system. Two types of atoms form two interpenetrating face-centered cubic lattices, commonly known as face-centered cubic structure. In this structure also, both atoms are tetrahedrally coordinated with each other and stacked in an ABABAB pattern.

Table 1.1 Properties of CdSe

Properties	**Types or values**
Phase stable at 300 K	Wurtzite (Hexagonal)
Space group	Zinc blende F43m and wurtzite P6_3mc
Lattice parameters at 300 K	Zinc blende (a_0=0.608 nm), Wurtzite (a_0=0.430 nm, c_0=0.702 nm)
Optical band gap (E_g)	≈ 1.797 eV (wurtzite) ≈ 1.712 eV (zinc blende)
Carrier mobility	660 cm^2/Vs
Electron drift mobility	720 cm^2/Vs
Melting point	>1300℃
Density of wurtzite phase	5.81 $g.cm^{-3}$
Toxicity	Highly toxic and carcinogenic to humans

1.8 Objectives of the thesis

In present thesis work, synthesis of pure and transition metal (Fe, Ni, Co)-doped CdSe nanostructures viz., nanoparticles and nanorods have been carried out by chemical route. Various characterization techniques have been employed for the study of synthesized nanostructures, as DMS material. The characterization techniques include XRD, TEM, EDS, UV-visible, PL spectroscopy, Raman spectroscopy, ESR and VSM/SQUID. The effect of doping on structural, optical and magnetic properties has been investigated. Further, the possible origin of magnetism has been discussed in detail.

Chapter 2

Syntheses and Characterizations

Chapter 2

Syntheses and Characterizations

There is a significant development in the field of nanostructured materials, their syntheses and characterizations, due to shape and size dependent properties. In the present chapter, a unified approach has been presented for the synthesis of CdSe nanostructures using solvothermal/hydrothermal route. Also, the characterization techniques employed have been discussed briefly, which include x-ray diffraction (XRD), photoluminescence (PL), UV-visible absorption spectroscopy, energy dispersive spectroscopy (EDS), transmission electron microscopy (TEM), vibrating sample magnetometer (VSM)/superconducting quantum interference device (SQUID).

2.1 Synthesis of CdSe nanostructures

Ideally, a given synthesis procedure should produce high-quality nanostructures by using low cost, less toxic, and environment friendly precursors and solvents. The various chemical methods such as colloidal [97], hydrothermal/solvothermal [98-100], chemical precipitation [101, 102], etc have been widely used to synthesize CdSe nanostructured materials. The colloidal and hydrothermal/solvothermal synthesis procedures are promising in this regard. However, there are some disadvantages in using colloidal synthesis procedure for CdSe nanostructures. First, this synthesis procedure is complicated. Second, synthesis temperature is difficult to control being high, and precursors (trioctylphosphine oxide, dimethyl cadmium) used are extremely toxic. On the other hand, hydrothermal and solvothermal synthesis techniques emerge as powerful tools for

synthesis of nanostructures due to low temperature, low cost, less toxic precursors and controllable morphology. In present work, hydrothermal and solvothermal syntheses techniques have been used for the synthesis of CdSe nanostructures as described in following sections.

2.1.1 Synthesis of CdSe nanoparticles

The synthesis of CdSe nanoparticles in present work has been done using hydrothermal technique. A hydrothermal technique can be defined as ‘‘a chemical reaction inside closed system in the presence of a solvent (aqueous solvent) at a temperature higher than the solvent’s boiling point’’ [103]. In order to carry out such reactions the solvent is heated well above its boiling point in a sealed vessel known as autoclave (Figure 2.1).

Figure 2.1 Pictorial view of Autoclave used in present work

There are two main parameters (chemical and thermodynamical) which control the given hydrothermal reaction. The chemical parameters include concentration of starting precursors, pH of reaction, and nature of solvent whereas, thermodynamical parameters include temperature and pressure of reaction. Final product obtained is generally in the form of powder. Thin films can also be deposited by this technique if a substrate is used.

Figure 2.2 show various steps followed for the synthesis of CdSe nanoparticles. Cadmium chloride ($CdCl_2$), sodium dodecyl sulfate (SDS), Selenium powder (Se) and de-ionized (DI) water were used as the starting precursors.

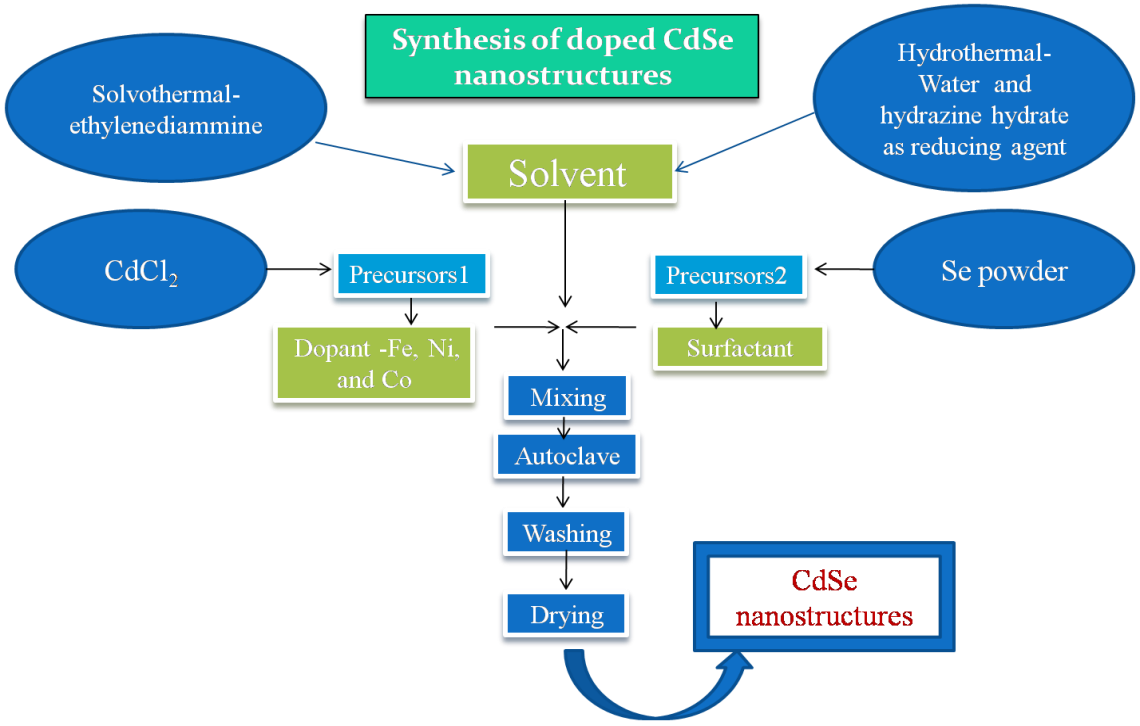

Figure 2.2 Schematic of hydrothermal/solvothermal synthesis of CdSe nanostructures

Appropriate amount of $CdCl_2$ was dissolved in DI water. SDS was used as a capping agent. Se was reduced with the hydrazine hydrate and this solution was added into the $CdCl_2$ solution.

Finally, the mixture was transferred to 50 ml Teflon-lined autoclave. Autoclave was placed at appropriate temperature for required time. The precipitates were washed with distilled water and ethanol for several times and, then dried in hot air oven to obtain the powder samples.

2.1.2 Reaction mechanism

The formation of nanoparticles during the synthesis can be understood by nucleation and growth process. SDS has been used as surfactant in the present work which aggregates in aqueous

solution to form micelles. It has two head groups, hydrophilic head and a long hydrophobic tail as shown in Figure 2.3 (a).

The possible reaction mechanism for the synthesis of CdSe nanoparticles [104]:

$$CdCl_2 + (NHNH_2)^{2+} + Se^{2-} + H_2O \rightarrow CdSe\,(\downarrow) + N_2\,(\uparrow) + H_2\,(\uparrow) + 2HCl + H_2O$$

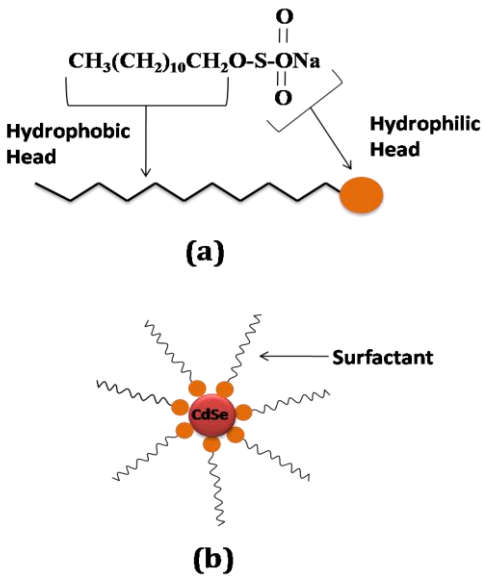

Figure 2.3 (a) Chemical formula with illustrative representation of SDS surfactant and (b) SDS capped CdSe nanoparticles

A surfactant is essential to prevent aggregation and forming stable nanoparticles. The hydrothermal treatment has been given after the loading of respective metal salts in teflon lined autoclave (Figure 2.1). The embryos are formed inside the micelle having unequal sizes and subsequently, their growth takes place by Ostwald ripening mechanism [105]. According to this mechanism, the larger particles grow at the cost of smaller ones leading to formation of spherical CdSe nanoparticles with narrow size distribution. The larger particles have lower surface to volume ratio as compared to smaller ones. Due to this fact, the smaller nanoparticles possess extremely large surface energy as compared to larger ones. The system tries to acquire an

equilibrium state by lowering down its energy via dissolution of smaller nanoparticles while larger ones continue to grow. This leads to the formation of SDS capped CdSe nanoparticles as shown in Figure 2.3 (b).

2.1.3 Synthesis of CdSe nanorods

The synthesis of CdSe nanoparticles has been done using solvothermal technique. The solvothermal technique is similar to hydrothermal technique as discussed in section 2.1.1. The hydrothermal technique is called solvothermal if we use a non-aqueous solvent.

Figure 2.2 shows the flow chart of various steps used for synthesis of nanorods. $CdCl_2$, Se and ethylenediammine (en) were used as reaction precursors.

The appropriate amount of $CdCl_2$ and Se powder were dissolved in en. The mixture was transferred to 50 ml Teflon-lined autoclave. The autoclave was then placed for required time at an optimum temperature in a heating oven and was allowed to naturally cool down at room temperature. The precipitates were collected, washed several times with distilled water and ethanol, and then dried in hot air oven under the ambient conditions to obtain the powder.

2.1.4 Reaction mechanism

The formation of CdSe nanorods can be explained by solvent coordination molecular template (SCMT) mechanism [106]. According to this mechanism, en is responsible for the synthesis of nanorods. The en works as a chelating agent and solvent in the present reaction. It helps in an anisotropic crystal growth and acts as a structure directing molecule. The possible reaction mechanism for synthesis of CdSe nanorods [106]:

$$Cd^{2+} + 2en \leftrightarrow [Cd(en_2)]^{2+}$$

$$[Cd(en_2)]^{2+} + Se^{2-} \rightarrow CdSe \cdot 0.5en \rightarrow CdSe\ (\downarrow) + en$$

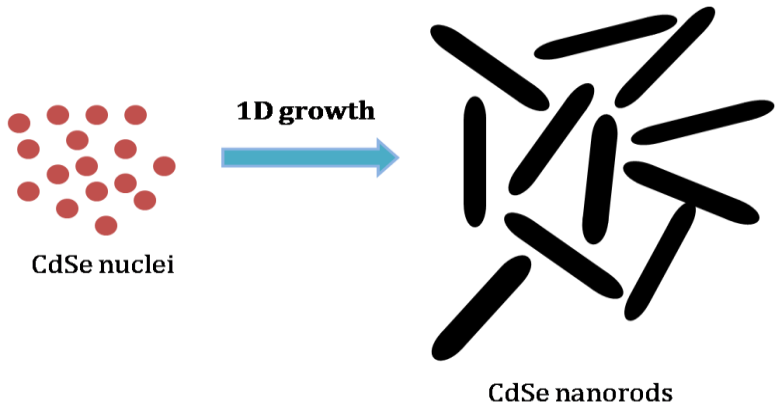

Figure 2.4 Schematic representation of formation of CdSe nanorods

First the formation of layered structure of CdSe·0.5en takes place. These layers are connected by en molecules via coordination bonds between two neighboring Cd^{2+} ions. Finally the en molecules come out of it leading to the formation of nanorods, as shown in Figure 2.4.

2.1.5 Doping in CdSe nanostructures

In the present research work, Fe, Ni and Co-doped CdSe nanostructures have been synthesized as DMS materials. The presence of dopant leads to significant change in structural, optical and magnetic properties. The detailed investigations of induce magnetism have been carried out (chapter 3, results & discussions) in order to know the exact origin of magnetism in doped nanostructures.

The common approach followed for doping is to introduce metal salt of given dopant during synthesis process of nanostructures, as shown in Figure 2.2. For the doping of Fe in CdSe nanostructures, their metal salt ferrous chloride tetrahydrate ($FeCl_2 \cdot 4H_2O$) is dissolved in $CdCl_2$ solution with the help of magnetic stirrer. The remaining synthesis procedure is same as described in sections 2.1.1 and 2.1.3. Similar procedure is adopted for the synthesis of Ni and Co

doped CdSe nanostructures by using their respective metal salts, nickel chloride hexahydrate ($NiCl_2 \cdot 6H_2O$) and cobaltous chloride hexahydrate ($CoCl_2 \cdot 6H_2O$). Following compositions were synthesized using above procedure:

- *Fe, Co, Ni-doped CdSe nanoparticles*
  - $Cd_{1-x}Fe_xSe$ (x = 0.00, 0.02, 0.04, 0.06, 0.08, 0.10)
  - $Cd_{1-x}Co_xSe$ (x = 0.00, 0.05, 0.10 and 0.15)
  - $Cd_{1-x}Ni_xSe$ (x = 0.00, 0.02, 0.05, 0.10)
- *Fe, Co, Ni-doped CdSe nanorods*
  - $Cd_{1-x}Fe_xSe$ (x = 0.00, 0.02, 0.05 and 0.10)
  - $Cd_{1-x}Co_xSe$ (x = 0.00, 0.05 and 0.10)
  - $Cd_{1-x}Ni_xSe$ (x = 0.00, 0.05, 0.10 and 0.15)

2.2 Characterization techniques

2.2.1 X-ray diffraction (XRD)

2.2.1.1 Introduction

X-rays are the electromagnetic waves having wavelength ranging from 0.01 to 0.10 nm. The wavelength of x-rays is of the same order as that of the inter-planar distance in the crystalline materials. Due to this, x-rays suffer diffraction when they are allowed to fall on the crystalline material and thereby, producing diffraction pattern by the constructive interference of

monochromatic beam. This is a powerful nondestructive analytical technique which provides wealth of information such as structures, phases, average grain size, crystallinity, crystal defects and strain. So, it can be considered as a fingerprint technique for the crystalline materials.

2.2.1.2 Bragg's Law

W.H. Bragg and his son W.L. Bragg in 1913 introduced the equation for constructive interference of x-rays, known as Bragg's law. It states that when x-rays are incident on a crystalline material's surface they reflect back at an angle of θ (as shown in Figure 2.5) giving rise to constructive interference, according to the condition [107].

$$2d \sin\theta = n\lambda$$

where d is inter-planar spacing, λ is wavelength of incident x-rays, θ is glancing angle, n is integer which gives the order of diffraction pattern. Braggs determined the crystal structures of NaCl, ZnS, diamond and were awarded Nobel Prize in 1915 for their work.

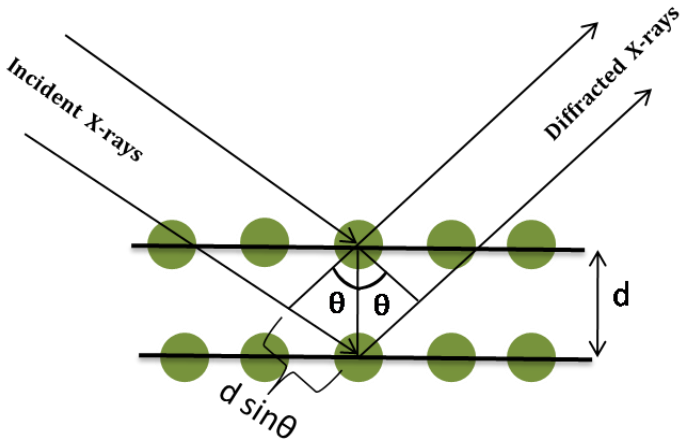

Figure 2.5 Bragg's law of diffraction

2.2.1.3 Instrumentation and working

Figure 2.6 shows the pictorial view of x-ray diffractometer instrument installed at Thapar University, Patiala. The diffractometer consist of x-ray tube, sample holder and detector. X-rays are produced in a cathode ray tube which consists of two electrodes: an anode made of tungsten or other high melting point material and a cathode. The electrons are accelerated towards the target by applying high voltage (of order 1 kV to 1 MV). On striking the target, the accelerated electrons produce x-rays.

Figure 2.6 Pictorial view of x-ray diffractometer

The characteristics x-ray spectra produced, consists of several components such as K_α and K_β. The monochromatic x-rays (K_α) are required for diffraction to occur, which is achieved by using foils or crystal monochromators. X-ray diffraction does not require tedious sample preparation procedure but only a suitable sample holder is required to fix material under investigation. The commonly used targets for x-ray generation are Cu, Co or Mo and energy of corresponding

emitted x-ray photons lies between 5 to 20 keV. The various types of detectors used to detect x-ray are scintillation detector, gas proportional counter, Ge solid state detector, linear CCD, image plate detector, CCD-camera, photographic film [108]. The detectors play a vital role in the determination of quality, consistency and throughput of x-ray diffraction analysis.

2.2.1.4 Sample preparation

Sample preparation is a very important step in order to obtain a good XRD pattern of given material, especially for soils and clays, which are poor reflectors of x-rays, as well as other types of materials such as iron oxide coatings and organic materials are difficult to characterize through XRD. Fine grained powder samples (around 1-5μm) are required for good quality of XRD analysis. In the present study, an agate mortar and pestle has been used to crush the samples in order to obtain required fine powder. The obtained fine powder is placed in the sample holder and then, compressed with glass plate in order to achieve a flat surface, before performing the measurement.

2.2.1.5 Applications of XRD

The most common use of XRD is phase analysis of crystalline materials. The diffraction pattern obtained from XRD is compared with the International Center Diffraction Data (ICDD) or formerly known as (JCPDS) Joint Committee on Powder Diffraction Standards data base and the best match is selected. The various types of information can be obtained from XRD pattern of crystalline materials, which has been listed in Table 2.1, given below.

Table 2.1 Information from XRD analysis

Peak positions	**Peak intensities**	**Peak shapes & widths**
Crystal system Space group symmetry Unit cell dimensions Qualitative phase identification	Unit cell contents Point symmetry Quantitative phase fractions	Crystallite size (2-200 nm) Non uniform micro strain Defects (stacking faults, etc.)

In present thesis work, XRD pattern of the synthesized samples were recorded using PANalytical X'Pert PRO X-ray diffractometer with CuK$_\alpha$ (λ = 1 .5418 Å) radiation operated at 45 kV and 40 mA and Shi-madzu, LabX XRD-6000, diffractometer with CuK$_\alpha$ (=1.5418 Å) operated at 40 kV and 30 mA.

2.2.2 UV-visible spectroscopy (UV-vis)

2.2.2.1 Introduction

UV-vis spectroscopy refers to the absorbance or reflectance spectra of a sample in solution or in solid form. UV-vis region falls in wavelength range of 200-800 nm of electromagnetic spectrum corresponding to energy of 6.2-1.5 eV. This energy is capable of promoting or (exciting) the electrons from ground state to first singlet excited state of the given samples. This spectroscopy

is generally applied to molecules or inorganic ions or complexes which are in solution form. However, absorption of solids and even of gases can also be recorded.

2.2.2.2 Beer-Lambert law

The principle of UV-vis spectroscopy is based on Beer-Lambert law [109], which states that, when a beam of monochromatic light is passed through a homogeneous solution of an absorbing material (Figure 2.7.), the rate of decrease of intensity of radiation with thickness of the absorbing solution is proportional to the intensity of incident radiation as well as the concentration of the solution.

Beer-Lambert law can be expressed by the following equation [109]

$$A = log\ (I_0/I) = \varepsilon \times c \times 1$$

where, A = absorbance, I_0 = intensity of light incident on the sample (or cuvette), I = intensity of light after passing through the sample (or cuvette), c = molar concentration of solute, l = length of sample holder (or cuvette) usually of 1 cm, ε = molar absorptivity

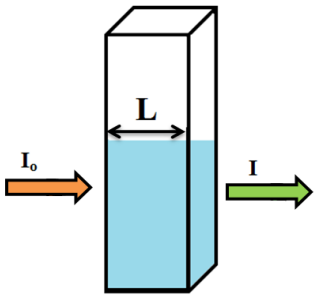

Figure 2.7 Illustration of Beer-Lambert law

2.2.2.3 Instrumentation and working

UV-vis spectrophotometer consist of five essential components given as (1) a stable radiation source (2) monochromator (3) sample holder (4) radiation detector or transducer (5) signal processing and output device, as shown in Figure 2.8.

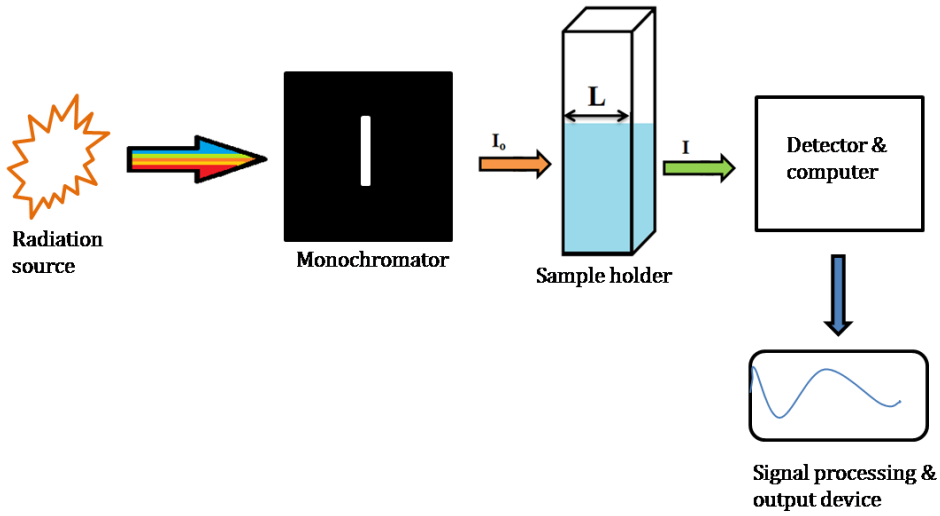

Figure 2.8 Illustration of essential components in a UV-vis spectrophotometer

A radiation source must provide good continuous intensity in UV and visible region. The commonly used radiation sources are deuterium lamp for UV measurements (190-400 nm) and tungsten-halogen lamp for visible measurements (400-800 nm). With time, the intensity of radiation sources decreases as the life span of a deuterium lamp is approximately 1,000 hr and that of tungsten-halogen lamp, approximately 10,000 hr. Generally, spectrophotometers consist of both types of radiation sources in order to measure the UV-visible spectrum of a given material. A Monochromator is an optical device which provides radiation of desired wavelength out of the wider range of wavelengths emitted by radiation source. Two types of monochromators used are prism and grating. In most of UV-vis spectrophotometers, quartz cuvettes are used as a sample holder in order to record UV-vis spectrum of the given sample.

Usually, square cuvettes having path length of 1.0 cm are used as a sample holder. A detector is required to convert a light signal into an electrical signal which can be measured and transformed into an output signal (Figure 2.8). Presently, three types of detectors are used in spectrophotometers namely phototube, photomultiplier tube and diode array detector. Figure 2.9 shows the pictorial view of UV-visible spectrophotometer.

Figure 2.9 Pictorial view of UV-visible spectrophotometer

2.2.2.4 Sample preparation

The samples must be clearly dispersed in a suitable solvent before taking measurement. Sonication or grinding can sometimes help to properly disperse the samples in the given solvent. If the samples are not properly dispersed then particles in the solution will scatter the incident light and therefore, detector will provide the incorrect data. In the present study, nanoparticles are dispersed in ethanol and sonicated for half an hour before taking the measurement.

2.2.2.5 Applications of UV-vis spectroscopy

- In present study, UV-vis spectra have been used to calculate the band gap of pure and doped CdSe nanostructures.
- UV-vis absorption spectroscopy can be used for the quantitative determination

of unknown sample by using Beer-Lambert's equation, $A = \varepsilon c l$.

- It can be used to detect impurities in the organic molecules. The additional peaks can be observed in UV-vis spectra due to the presence of impurities in sample which can be compared with standard raw material.
- The kinetic (or rate) of reactions can also be studied by using UV-vis spectroscopy. UV-vis radiations are passed through the reaction cell and corresponding absorbance changes can be observed.
- It can also be used to determine the molecular weight, dissociation constant of acids or bases and structure of organic compounds.

In the present thesis work, the optical absorption spectra were recorded with UV-visible spectrophotometer of Analytic Jena, SPECORD 205.

2.2.3 Photoluminescence (PL) spectroscopy

2.2.3.1 Introduction

Photoluminescence spectroscopy is a powerful non-destructive technique to study the electronic structure in a given material. A laser light is directed onto the sample which photo excites electrons of the given material. The luminescence (or emission of light) takes place when photo-excited electrons de-excite spontaneously [110]. This luminescence (or emission of light) is known as photoluminescence (PL). PL is of two types: energy resolve and time resolve. PL can be observed at room temperature as well as at low temperatures. However, at low temperature the spectral emission lines become sharper and stronger, which reveals more structural information.

2.2.3.2 Instrumentation and working

A laser light is directed onto the sample with energy much larger than optical band gap of the sample as shown in Figure 2.10. PL experiments can also be carried out in a variable temperature range i.e. cryostat unit (1.5 - 300 K) in order to get more insight of the sample.

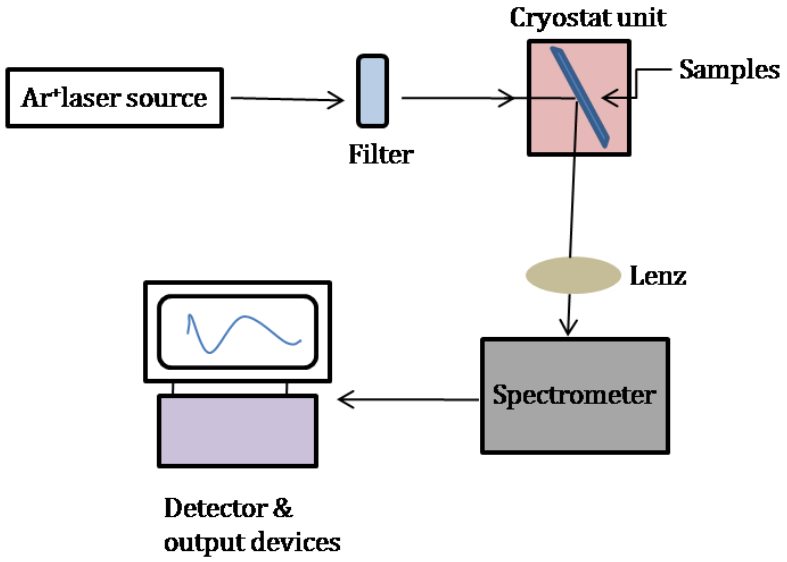

Figure 2.10 Experimental set-up of PL spectrophotometer

The emission peaks are enhanced and also, we can reveal the minor emission peaks which are not observed at room temperature. The emitted light is selected by filters in order to take the measurements at any pair of fixed wavelengths. When laser light incident on the sample, the orientation of sample is selected in such a way that the reflected laser light and PL emission propagate in different directions. The emission light propagates through fiber optic cable and spectrophotometer. The diffraction grating inside spectrophotometer diffracts different wavelengths in different directions. The detector measures signal intensity corresponding to each wavelength and the output device displays PL spectra of the sample under investigation. Pictorial view of photoluminescence spectrometer is shown in Figure 2.11.

Figure 2.11 Pictorial view of photoluminescence spectrometer

2.2.3.3 Sample preparation

The sample for PL analysis was prepared by dispersing the nanoparticles ultrasonically in ethanol in present study.

2.2.3.4 Applications of PL spectroscopy

- The band gap can be determined from radiative transitions between conduction and valence bands of a semiconductor in PL spectra.
- PL emission spectra can be used to determine impurity levels and defects in semiconductors. PL emission energy can be used to identify specific defects whereas; the PL intensity can be used to determine their concentration.
- The quality of material can also be determined from radiative and non-radiative transitions. The non-radiative transitions are related with localized defects whose presence can affect material's quality and subsequently, the device performance. So, the material quality can be measured by quantifying the amount of radiative transitions involved.

In present thesis work, The PL spectra of the synthesized samples were recorded using Perkin Elmer LS55 spectrofluorimeter.

2.2.4 Transmission electron microscopy (TEM)

2.2.4.1 Introduction

TEM is an important characterization tool for micro and nano world, as it can provide wealth of information about the morphology of materials with sizes varying from micro to atomic scale. First TEM was built in 1932 by Ernst Ruska and Knoll [111]. TEM uses high energy electron beam usually 100-300 keV, which impinges upon the thin sample (< 200 nm). A series of electromagnetic lenses focus the electron beam into an image or a diffraction pattern. The wavelength of electron is 100,000 times smaller than visible light, which results in greater resolving power of TEM. This leads to increased resolution (≈ 0.1 nm) comparable to atomic dimensions. Today, TEM is an integral part of many research laboratories and can be used to examine the morphology and structure of microorganisms, cells, metals, crystal structures and surfaces.

2.2.4.2 Interactions of electron beam with sample

When a beam of electron strike sample, different kinds of interactions take place, shown in Figure 2.12. These interactions result in backscattered electrons, unscattered electrons, Auger electrons, elastically scattered electrons, inelastically scattered electrons, and x-rays [112].

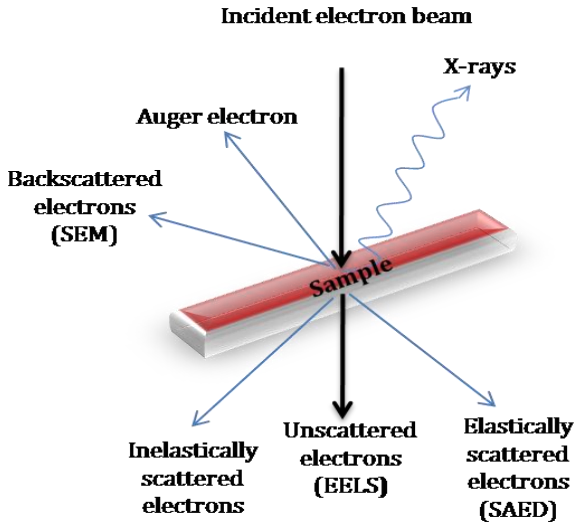

Figure 2.12 The illustration of various types of interactions between sample and electrons

The backscattered electrons are caused by incident electrons colliding normally with atoms in the sample. These are used to determine SEM image of the samples. The secondary electrons are produced when the incident beam of electron have a sufficient energy to eject the inner most electrons of the sample (usually K-shell). This causes a vacancy which is filled by upper orbital electron of the same atom and energy is liberated in the form of x-rays. This energy is sufficient to eject the outer electron known as Auger electron. When the incident electrons pass through the sample without any interaction, the transmitted electrons are known as unscattered electrons. The incident electrons scattered by sample's atoms elastically are known as elastically scattered electrons. When there is energy loss, the scattered electrons are known as inelastically scattered electrons which are used for electron energy loss spectroscopy (EELS). This spectroscopy is used for the determination of oxidation state of elements.

2.2.4.3 Instrumentation and working

TEM works in the same manner as that of a slide projector. Projector shines a beam of light through a slide and an image is formed on the screen according to structures and objects on the slide.

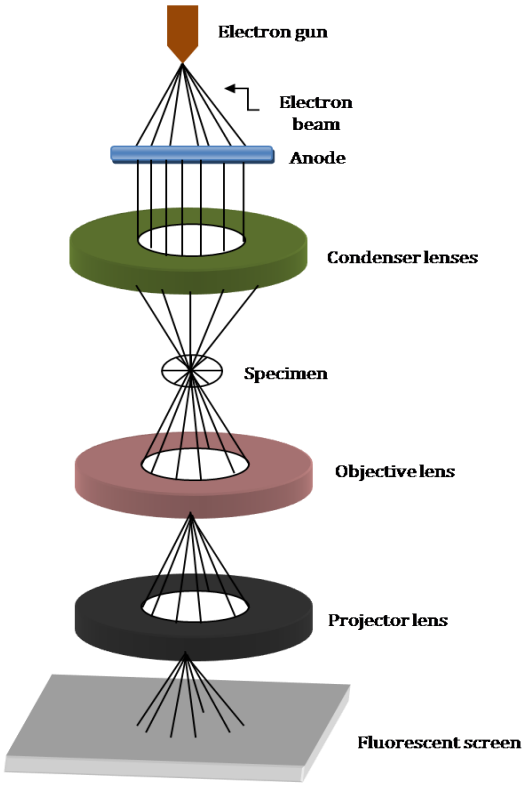

Figure 2.13 The main instrumental components and working of TEM

The working of TEM is similar to projector, except that instead of light electrons are transmitted through the specimen and image is formed on fluorescent (phosphor) screen. TEM consist of four main components: an electron gun, a vacuum system, a series of electromagnetic lenses and electrostatic plates (Figure 2.13) [113]. The tungsten filament acts as an electron gun which produces a monochromatic beam of electrons. The emitted electrons are accelerated and focused

to a small, coherent beam by condenser lenses. The beam is then passed through the thin specimen. After this, transmitted electrons are focused by objective lens, which finally strike on a fluorescent (phosphor) screen, producing an image. Pictorial view of TEM is shown in Figure 2.14.

Figure 2.14 Pictorial view of TEM [114]

2.2.4.4 Sample preparation

The powdered samples were dispersed in ethanol ultrasonically, and a drop of this solution was spread on carbon coated copper grid. Then, the grid was placed in a sample holder to view images.

2.2.4.5 Applications of TEM

TEM can be used in different modes to obtain the information:

- Bright Field (BF)/Dark Field (DF) mode

In BF mode, electrons are scattered and absorbed within the specimen and regions with higher thickness will appear darker in resulting image. However, in DF mode, scattered electrons from the specimen are collected and this mode is useful for transparent samples. The BF/DF modes can provide information about the shape and size of particles, defects, phases and grain boundaries.

- High Resolution Transmission Electron Microscopy (HRTEM) mode

This mode allows obtaining the lattice fringes imaging of specimen under investigation. The crystal structure, visualization of defects and inter-atomic distances can be directly observed from HRTEM images.

- Electron Diffraction (ED) mode

The crystalline specimen diffracts electrons, leading to formation of diffraction pattern, which allows the determination of crystallographic information such as lattice parameters, crystal symmetry and orientation.

Apart from above mentioned structural characterization, elemental and chemical composition can be obtained using additional accessories and techniques such as Energy-dispersive X-ray spectroscopy (EDS). This gives qualitative and quantitative elemental analysis. Electron Energy Loss Spectroscopy (EELS) provides information about the nature of atoms, their bonding, nearest neighbors and oxidation state.

In present thesis work, TEM images of the synthesized samples were recorded using transmission electron microscope (TEM; Hitachi (H-

7500)). SAED and HRTEM images were recorded using TEM (JEOL 2100F) operated at 200 keV.

2.2.5 Energy dispersive spectroscopy (EDS)

2.2.5.1 Introduction

EDS is an analytical technique used for the elemental analysis of a given material. It uses characteristic x-rays, produced when a high energy electron beam strike on specimen surface. It is a qualitative and quantitative analysis which provides the information about elements having atomic number (Z >3) [115]. It is a nondestructive technique, which can be applied for the measurement of sample in wide variety of forms such as solids, powders, liquids, and thin films.

2.2.5.2 Interaction volume

The interaction of an electron beam with specimen surface is the basis for imaging and elemental analysis (in SEM & EDS). The interaction depth can vary from 1 µm to 6 µm, depending on material of specimen, known as interaction volume. The various types of signals generated in interaction volume are shown in Figure 2.15. The most of incident electrons are scattered elastically or inelastically from the sample's surface or near surface, without penetrating through specimen.

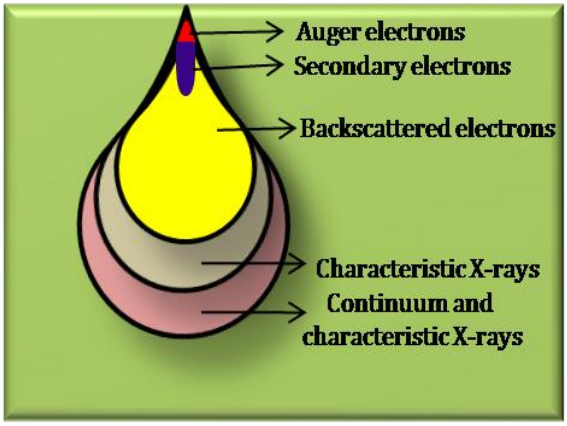

Figure 2.15 The interaction of electrons beam with specimen surface

The electrons which are ejected by an elastic collision are referred to as backscattered electrons. These are high energy electrons having energy comparable to incident electrons. The secondary electrons are ejected due to inelastic scattering of incident beam of electron with loosely bound specimen electrons. The emitted electrons possess lower energy typically 50 eV or less. After the ejection of secondary electrons, vacancies are created and electrons from higher energy shells falls down to the lower energy shell and characteristic x-rays are produced during these transitions. When this energy is transferred to third electron, the emitted electrons are known as Auger electrons.

2.2.5.3 Theory of EDS

When inner shell (usually K) electrons are ejected by bombardment of high energy beam of electrons, the atoms get excited. The ejected electron creates a vacancy and consequently, electron from higher orbital drops down in order to fill it (Figure 2.16).

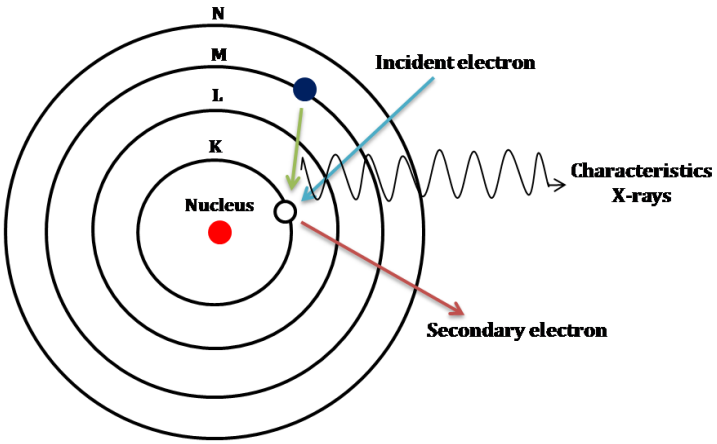

Figure 2.16 Principle of EDS

The atoms return to its normal state by giving up its energy. The emitted energy is known as characteristics x-rays and equals to difference between two electrons states. The emitted x-ray energy is characteristic of the element present. EDS detector separates the characteristic x-rays of different elements into an energy spectrum and EDS system software analyzes the energy spectrum, which provide qualitative and quantitative information about the elements present in the specimen.

2.2.5.4 Instrumentation and working

EDS systems are attached with either SEM or TEM instrument. It includes electron gun, x-ray detector and software to collect and analyze energy spectra, as shown in Figure 2.17. An electron gun produces high energy electron beam which falls on specimen surface and different type of interactions take place (Figure 2.15).

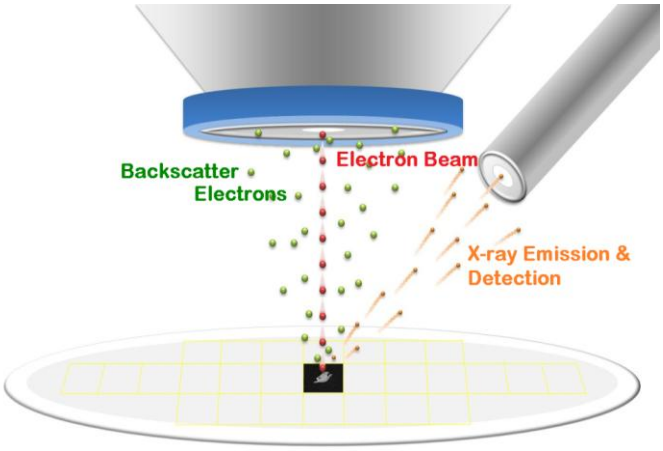

Figure 2.17 Schematic representation of EDS components [116]

EDS detector absorbs the energy of incoming characteristics x-rays and convert them into electrical voltage pulses. The system software collects signal and analyze energy corresponding to the characteristics x-rays of elements comprising the sample. The pictorial view of EDS attached to SEM is shown in Figure 2.18.

Figure 2.18 EDS instrument attached with SEM

2.2.5.5 Sample preparation

The sample preparation is required before recording EDS. It is placed under high vacuum conditions, so water must be removed from the samples. All non-conducting samples are made conducting by coating the sample with conducting material (usually gold). The carbon tape has been used as bonding agent between sample holder and powder material. The thin gold coating on sample's surface has been done with sputter coating unit. Finally, it is placed in sample holder for analysis.

2.2.5.6 Applications of EDS

- Elemental analysis: X-ray energy values from the specimen are compared with known characteristic x-ray values by system software which determines the presence of an element in specimen. The elements from Boron to Uranium can be determined by EDS and minimum detection limit vary from 0.1 to a few weight percent, depending on specimen under investigated.
- Elemental mapping: The variations in characteristics x-ray intensity at any point can yield information regarding the relative concentration of elements present in specimen. One can record the image brightness intensity as a function of local relative concentration of elements. This gives very useful information regarding the distribution of elements in a given specimen.
- Line profile analysis: A line is preselected across the specimen and electrons beam is scanned along this line. X-rays are detected along line and relative elemental concentration can be known along the given path.

In present thesis work, the presence of dopant and impurities was confirmed by energy dispersive x-ray spectroscopy (EDS) of OXFORD analytical, attached with SEM.

2.2.6 Raman spectroscopy

2.2.6.1 Introduction

In the year of 1928, Sir C. V. Raman an Indian physicist discovered the inelastic scattering of light and awarded novel prize for physics in 1930. In Raman spectroscopy, inelastically scattered light allows the interrogation and identification of vibrational (phonon) modes of molecules [117]. It is an invaluable analytical tool for molecular finger printing and monitoring changes in molecular bond structure, as well.

2.2.6.2 Theory

When monochromatic radiations are focused on a given sample then most of the radiations will be scattered elastically. If molecules of the sample are excited to a virtual electronic state, they will immediately come back to their original state by emitting photons of energy (Figure 2.19). When energy of incident photons is equal to energy of scattered photons then this process is known as Rayleigh scattering.

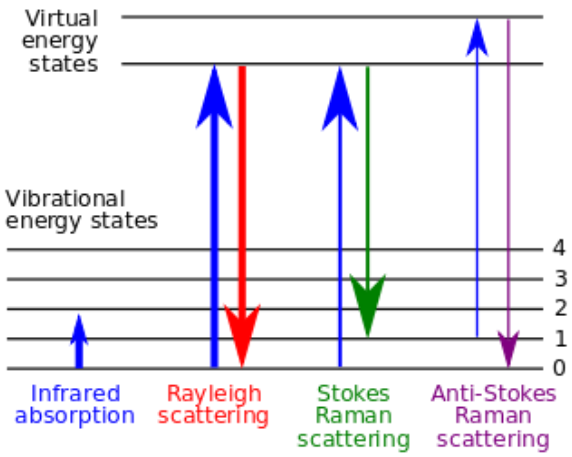

Figure 2.19 Schematic showing energy states involved in Raman signal [118]

Also, a given molecule may emit a photon having energy higher or lower than incident photon called Stokes and anti-Stoke scattering. The difference in energy of incident and scattered photon is known as Raman shift. It is this Raman shift which gives the information about molecular structure of samples.

2.2.6.3 Instrumentation and working

An intense beam of laser light is focused on the sample, as shown in Figure 2.20. Most of the scattered light possess same wavelength as that of incident one, along with Raman shifted light.

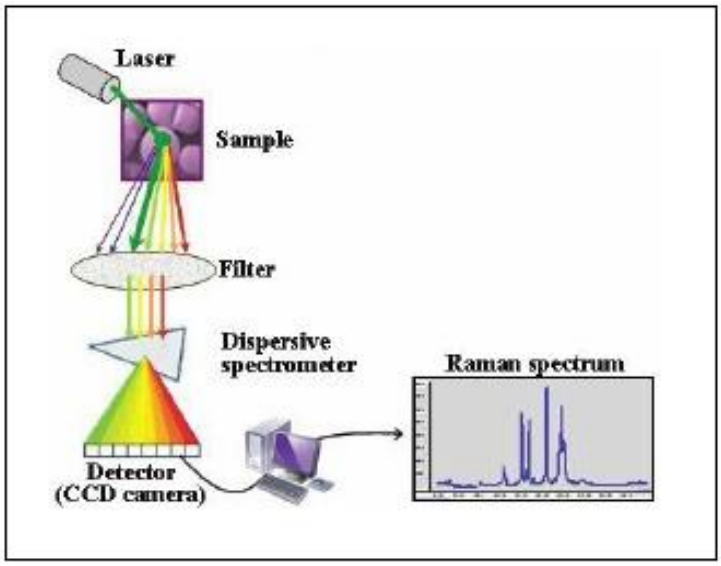

Figure 2.20 The block diagram of Raman spectrometer [119]

The emitted light is collected which is subsequently filtered to remove the laser light. The remaining light is allowed to pass through a dispersive spectrometer. The spectrometer separates different wavelengths of light and finally, it is detected by detector. The results were collected and plotted which appeared in the form of Raman spectrum. The pictorial view of Raman spectrometer is shown in Figure 2.21.

Figure 2.21 Pictorial view of Raman spectrometer [120]

2.2.6.4 Applications of Raman spectroscopy

- The characteristics Raman modes can be used to identify composition of a given material.
- The change in frequency of Raman peaks gives information regarding stress and strain in a given material.
- The width of observed Raman peak determine the quality of synthesized crystalline material.
- Intensity of Raman peaks can be related to the amount of material present in a given system.

In present thesis work, Raman measurements were performed by Renishaw Iniva Raman spectrometer. The samples were excited by laser source having 785 and 514.5 nm wavelength, with exposure time of 30 sec.

2.2.7 Electron spin resonance spectroscopy (ESR)

2.2.7.1 Introduction

ESR is a versatile, non-destructive technique which has been used for over 50 years to study variety of paramagnetic species. The first observation of ESR signal was made by a Soviet physicist Zavoisky, in 1944 [121, 122]. Afterwards, extensive studies have been carried out by subsequent groups and nowadays, it is a standard research tool. Although, ESR signal is limited

to substances having unpaired electrons but it finds a variety of applications in the field of biology, chemistry, medicine and physics.

2.2.7.2 Theory

ESR is based on the interaction of unpaired electrons spin with external applied magnetic field. When these unpaired electrons are subjected to external magnetic field, the electron spin magnetic moment align itself parallel (m_s = 1/2) or antparallel (m_s = -1/2) to the field, as shown below.

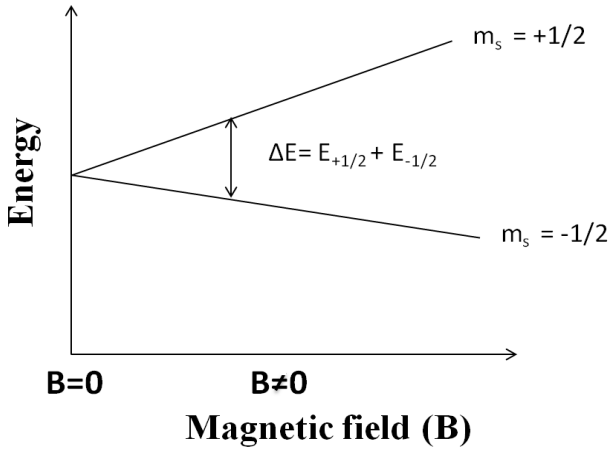

Figure 2.22 Energy level diagram of an electron spin (S = ± 1/2) in presence of applied magnetic field B

An electron can jump between two energy levels (Figure 2.22) by absorbing or emitting photon of energy ΔE given by following relation

$$\Delta E = h\nu = g_e \mu_B B$$

where, g_e is Landé g-factor, μ_B is Bohr magneton, B magnetic field, h is planck's constant and ν frequency of incident radiations. The resonance can be observed either by keeping constant

magnetic field or by varying the applied frequency, or vice versa. Generally during ESR measurement, frequency is kept constant as it is much easier to vary magnetic field.

2.2.7.3 Instrumentation and working

ESR spectrometers consist of a microwave source, an attenuator, electromagnets, sample cavity, and detector as shown in Figure 2.23 [123]. The klystron is source of radiations which generate stable high power microwaves. Most of the ESR spectrometers are operated at 9.5 GHz frequency. The sample is placed in cavity and microwave radiations fall on it. The cavity placed between the poles pieces of an electromagnet is capable of producing magnetic field upto 8000 G, required for ESR measurement.

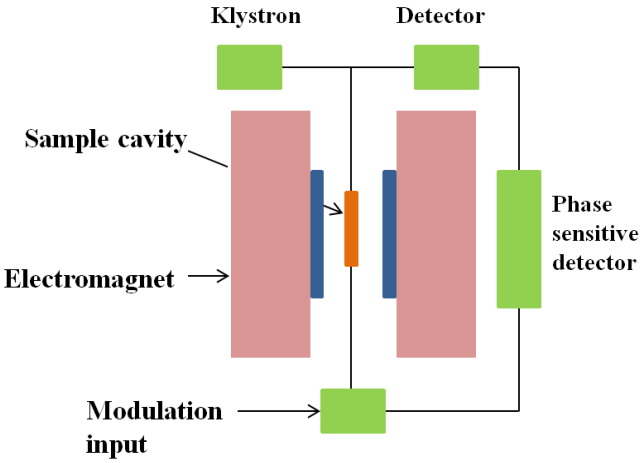

Figure 2.23 Block diagram of ESR spectrometer [124]

When separation between two energy levels equals the microwave energy, then corresponding absorption signal is detected by the detector. The obtained signal is usually converted into derivative form in order to improve signal to noise ratio. Pictorial view of ESR spectrometer is shown in Figure 2.24.

Figure 2.24 Pictorial view of ESR [125]

2.2.7.4 Sample preparation

Few mg of powder sample has been used for ESR measurement, in present work. However, samples in the form of liquid (few ml) or gaseous form can also be analyzed by ESR measurement.

2.2.7.5 Applications of ESR

- Free radicals and paramagnetic species can be detected and measured by this technique.
- This technique has been extensively employed to biological systems such as tissues, seeds and leaves etc. to study the presence of free radicals.
- Various point defects in solids can be analyzed by this technique.
- One can also study the molecular structure, crystal structure, reaction kinetics, electron transport etc.

In present thesis work, the samples were characterized by Bruker EMX EPR Spectrometer and E-112 ESR Spectrometer, VARIAN, USA.

2.2.8 Vibrating sample magnetometer (VSM)

2.2.8.1 Introduction

VSM measures the magnetic properties of materials. It was invented in 1956 by Simon Foner at MIT [126]. It is based on Faraday's law of electromagnetic induction. When a sample is placed in uniform magnetic field, dipole moment is induced in the sample. The sample is physically vibrated sinusoidally which induces an electrical signal in the pick-up coils. The electrical signal is proportional to magnetization of the sample. Greater the magnetization greater will be induced current. VSM can measure samples with extremely low magnetic signals ($5x10^{-7}$emu) and low coercivity (10 mOe) in fields up to 2T. It can be used to measure the magnetism in materials of different forms such as the powder, thin films and liquid.

2.2.8.2 Instrumentation and working

Figure 2.25 shows the schematic representation of various components present in VSM. The sample is inserted in the sample holder and it rests at centre in a pair of pickup coils between the poles of an electromagnet. The sample is magnetized due to uniform magnetic field of electromagnet. The sample is vibrated along the vertical axis and voltage is induced in the pickup coil which is proportional to the sample's magnetic moment. Pair of stationary coils picks up the induced ac signal, which is proportional to the amplitude and frequency of the vibration of sample. The output measurement displays magnetic moment (m) as a function of applied field

(H). The magnetic field is usually generated by an electromagnet driven by a DC bipolar power supply.

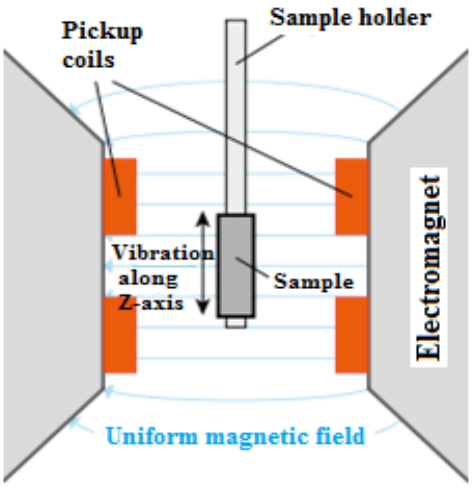

Figure 2.25 Schematic representation of VSM [127]

The voltage V measured across the sensing coils in a VSM can be expressed as [128]:

$$V = m \times A \times F \times S$$

where, m is the magnetic moment of the sample, A is amplitude of vibration, F is frequency of vibration, S is sensitivity function of the sensing coils. Using VSM, one can measure DC magnetic moments as a function of temperature, magnetic field and time. So, it allows performing susceptibility and magnetization studies. Pictorial view of VSM is shown in Figure 2.26.

Figure 2.26 Pictorial view of VSM [129]

2.2.8.3 Sample preparation

In the present study, in order to perform measurement, few mg of powder sample was placed in sample holder.

2.2.8.4 Applications of VSM

VSM is mainly used to measure the magnetic properties of materials in different forms such as powder, liquid and thin films. Diamagnetic, paramagnetic, ferromagnetic, ferrimagnetic, and antiferromagnetic properties of materials can be observed from this instrument. The magnetic recording materials, GMR, CMR, spin valve, magneto-optical materials can also be studied using VSM.

In present thesis work, the magnetic measurements (M-H) were performed by vibrating sample magnetometer (VSM) (Lake Shore).

2.2.9 Superconducting quantum interference device (SQUID)

2.2.9.1 Introduction

SQUID device was first proposed by Brian Josephson in 1962 [130]. It is the most sensitive device used to measure very weak magnetic signals i.e. magnetic flux. It can even measure the electromagnetic field of a human body. This device basically relies on Josephson effect. A thin insulating layer is sandwiched between two superconductors, making a Josephson junction. It is useful for many purposes in engineering, physics, biology and medicine.

2.2.9.2 Josephson effect

When two superconductors are joined by a very thin insulating layer (≈ 10 nm), there is a probability that electron pairs (cooper pairs) can pass through the junction by tunneling which leads to electric current. If a small voltage is applied across the junction, oscillating current starts flowing through the junction, known as A. C. Josephson effect [131]. Instead, if a constant current is passed through the junction, no voltage drop is detected across it, known as D. C. Josephson effect [131]. There are two types of SQUID on the basis of a superconducting loop interrupted by either one or two Josephson junctions, RF or DC SQUID, respectively. RF-SQUID is based on A. C. Josephson effect and DC SQUID is based on the DC Josephson effect. The major difference between RF and DC SQUID is that, DC SQUID may offer lower noise as compared to a RF SQUID but it is very difficult to operate a DC SQUID and also, fabricate two nearly identical Josephson junctions in a single device.

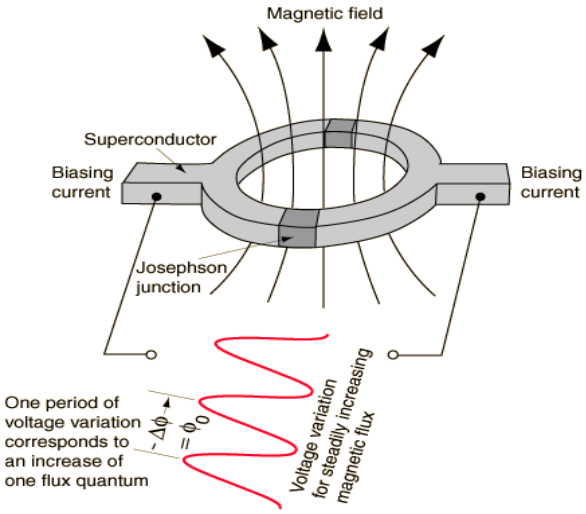

Figure 2.27 Josephson junctions within a superconducting ring. A change in flux produces a voltage variation across the Josephson junction [132]

The sensitivity of SQUID can be associated with changes in magnetic field with quantized magnetic flux (Φ) given by [131]

$$\Phi = h/2e \approx 2.067 \times 10^{-15} \text{ tesla } m^2$$

If a constant biasing current is applied across the SQUID device, the measured voltage oscillates with the changes in phase at the two junctions, which depends upon the change in the magnetic flux, as shown in Figure 2.27.

2.2.9.3 Instrumentation and working

The main components of a SQUID are: (a) superconducting magnet, (b) superconducting detection coil coupled to the sample and (c) SQUID connected to the detection coil (shown in Figure 2.28).

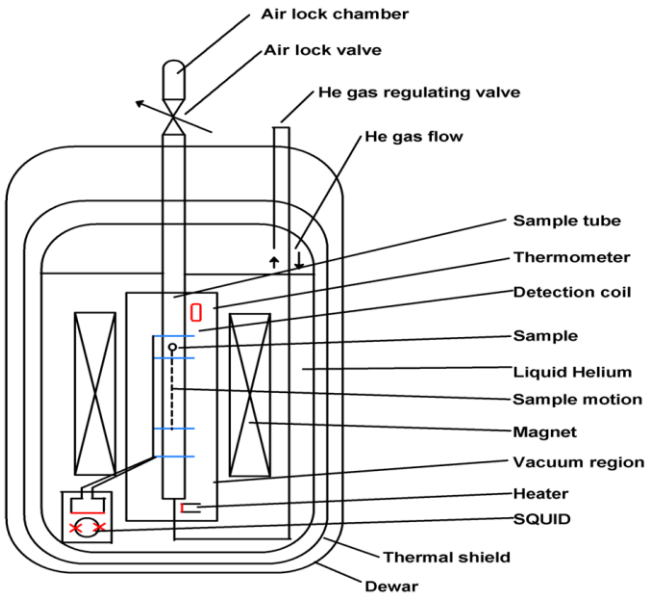

Figure 2.28 Schematic representation of various parts of a SQUID device [133]

A superconducting magnet is a solenoid made from superconducting wire. This solenoid is kept in liquid helium which can generate magnetic fields in the range of 5-18 Tesla. Superconducting detection coil is a single piece of superconducting wire which is placed in the uniform magnetic field of solenoidal superconducting magnet. When sample is moved through detection coil, the magnetic moment of sample induces an electric current in the pick-up coil system. This changes the persistent current in detection coil which further produces the variation in SQUID output voltage proportional to the magnetic moment of sample. A SQUID can allow the measurements to be made over a wide range of temperature (4-400 K). The liquid helium and heater is used to control the sample's temperature. Pictorial view of a SQUID instrument is shown in Figure 2.29.

Figure 2.29 Pictorial view of SQUID [134]

2.2.9.4 Sample preparation

In most of SQUID measurements, a plastic straw is used as sample holder because the straw has minimal magnetic susceptibility. In the present study, few mg of powder sample was placed on teflon tape and it was rolled to form a bead. This bead was put inside the straw for the measurement.

2.2.9.5 Applications

Presently, the most common use of SQUID is magnetic property measurement of variety of systems. The testing of eddy currents using SQUID have been used for many years to detect flaws in structures and it finds potential applications in detection of stress or corrosion in reinforcing rods used in bridges, aircraft runways or buildings. In biology, it is used worldwide to measure magnetic signals from the heart, brain, lungs, liver, nerves, skeletal muscle, stomach, intestines, eyes, and other organs.

In present thesis work, the magnetic measurements were performed by using SQUID (Quantum design).

Chapter 3

Results & Discussions

Chapter 3

Results & Discussions

The present chapter deals with results obtained for Fe, Ni and Co-doped CdSe nanostructures and their discussions. The various characterization techniques such as XRD, UV-visible, PL, TEM, Raman spectroscopy, ESR, and VSM/SQUID have been employed in order to study their properties and to know the origin of magnetism in these doped nanostructures. The detail has been given as below:

3.1 Structural, optical and magnetic properties of Fe-doped CdSe nanoparticles

This section deals with the series of $Cd_{1-x}Fe_xSe$ (x = 0.00, 0.02, 0.04, 0.06, 0.08, 0.10) nanoparticles. The nanoparticles were synthesized by hydrothermal technique, as discussed in detail in chapter 2. The structural, optical and magnetic properties of pure and Fe-doped nanoparticles were investigated. The obtained results are discussed below:

3.1.1 Structural and phase analyses

Structural properties of $Cd_{1-x}Fe_xSe$ nanoparticles were investigated from XRD pattern (Figure 3.1). The well resolved peaks observed in XRD pattern indicate that the CdSe nanoparticles are single phase and polycrystalline in nature. All the peaks are in well agreement with wurtzite phase of CdSe (JCPDS card no. 77-2307) up to 6 % doping concentration whereas secondary phase starts appearing at and above this concentration. All the peaks of secondary phase of $FeSe_2$ can be matched with JCPDS No. 21-0432. The decrease in crystallinity and peak broadening was observed with increase in Fe doping concentration. The ionic radius of Fe^{2+} (0.76 Å) which is

smaller as compared to that of Cd^{2+} (0.97 Å), leads to lattice distortion. The average crystallite size (D) of CdSe nanoparticles was calculated using Scherrer's formula [107],

$$D = \frac{k\lambda}{\beta \cos\theta}$$

where K is a constant having value 0.94, λ is the wavelength of x-ray radiation, β is the full-width half maxima (FWHM) and θ is the diffraction angle.

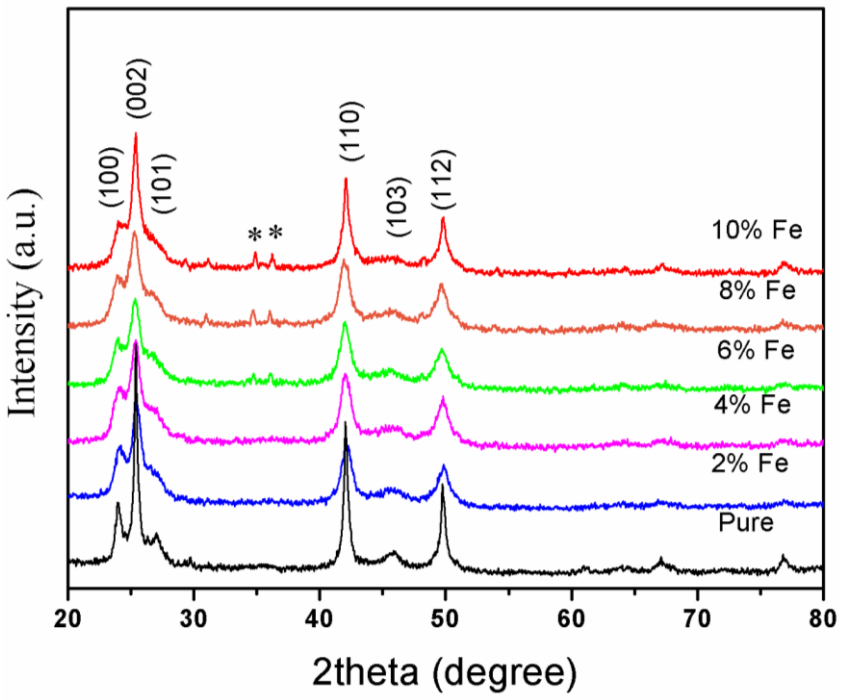

Figure 3.1 XRD pattern of $Cd_{1-x}Fe_xSe$ ($0 \leq x \leq 0.1$) nanoparticles (* represents the secondary phase of $FeSe_2$)

The average crystallite size comes out to be, respectively, 12.97, 9.42, 8.03, 7.88, 7.87 and 13.18 nm for the pure, 2 %, 4 %, 6 %, 8 %, and 10 % Fe-doped CdSe nanoparticles. It has been found that the average crystallite size decreases up to 6 % of Fe-doping concentration and then, it starts

increasing. The origin of secondary phase at and above 6 % Fe concentration indicates that Fe ions are segregating and they are occupying some other position instead of replacing Cd ions in the lattice. A similar trend has also been noticed in other reports [135, 136].

3.1.2 Compositional analysis

EDS technique is used to determine the chemical constituents present in samples. Figure 3.2 shows the EDS spectra of pure and Fe-doped CdSe nanoparticles.

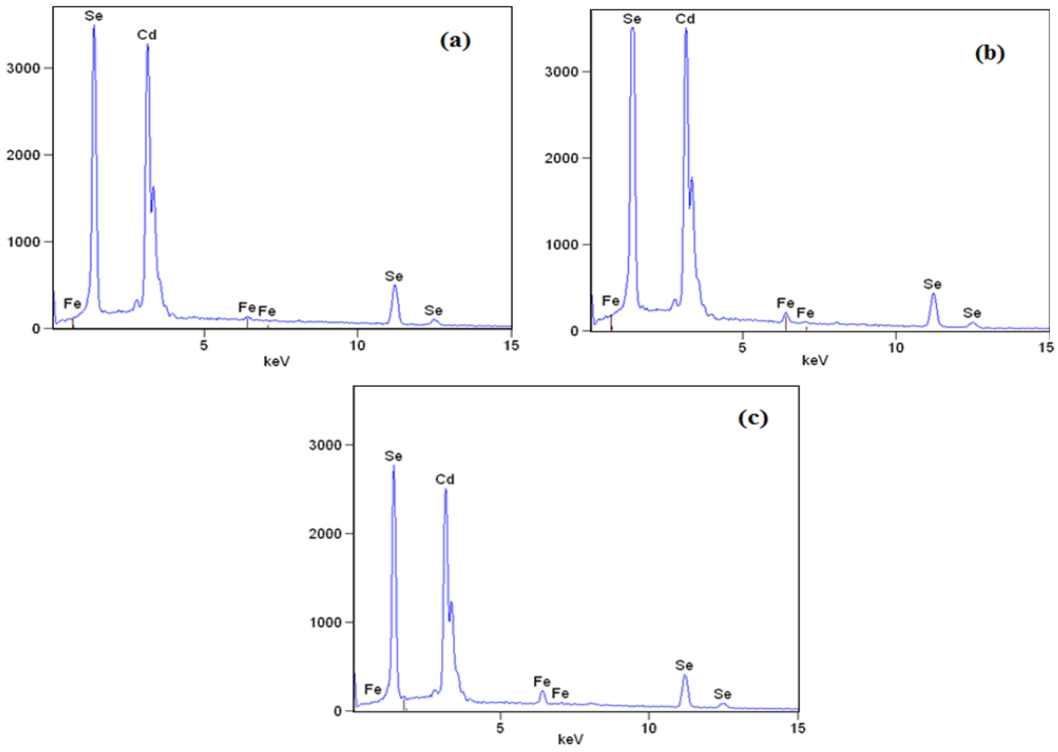

Figure 3.2 EDS spectra of (a) pure, (b) 6%, (c) 10 % Fe-doped CdSe nanoparticles

It is clear from Figure 3.2 that Cd and Se are present in their stoichiometric ratio. It shows the presence of Fe consistent with our experimental plan. No other additional impurities were observed in EDS spectra.

3.1.3 Morphological analysis

TEM was used to determine particle size and shape of as synthesized nanoparticles. To record the micrographs, powdered samples were dispersed in ethanol and then, ultrasonicated for fifteen minutes. Figure 3.3 shows TEM micrographs of pure and 6 % Fe-doped CdSe nanoparticles. These clearly show that both pure and doped nanoparticles are spherical in shape

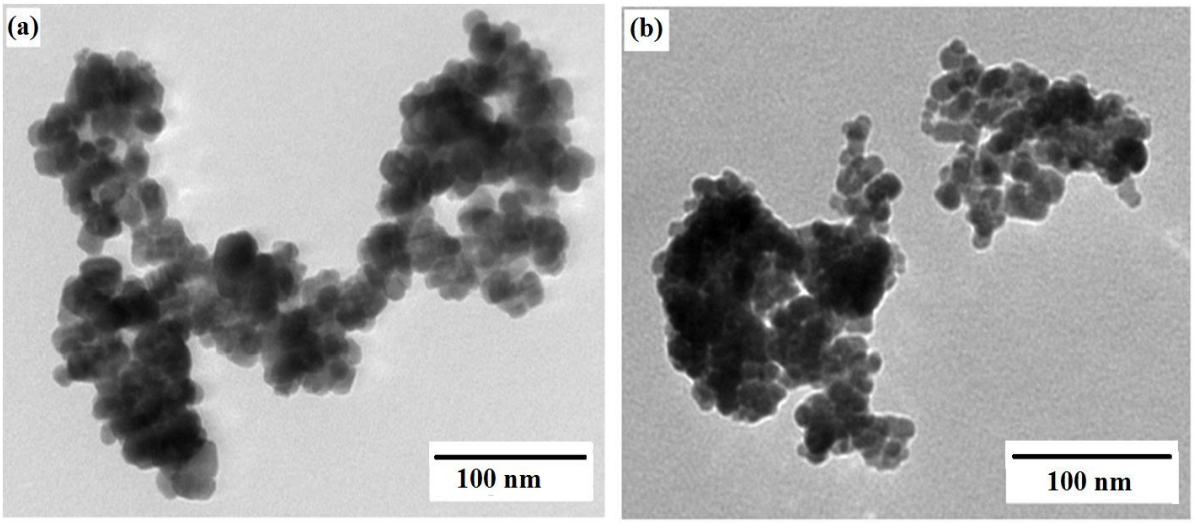

Figure 3.3 TEM micrograph of (a) pure and (b) 6 % Fe-doped CdSe nanoparticles

with uniform particle size distribution. The average particle size comes out to be around 14 nm for pure CdSe nanoparticles and 10 nm for 6 % Fe-doped CdSe nanoparticles. It has been found that Fe doping resulted in decrease of average particle size. The average particle size obtained from TEM has been found to be in agreement with that of calculated using Scherer's formula.

3.1.4 Optical analyses

3.1.4.1 UV-vis. analysis

To understand the optical absorption and energy band gap (E_g) of $Cd_{1-x}Fe_xSe$ ($0 \leq x \leq 0.1$) nanoparticles, UV-visible absorption spectra were recorded and are shown in Figure 3.4 (a). The absorption spectra were used to calculate E_g of the synthesized nanoparticles, using Tauc's relation,

$$(\alpha h\nu)^2 = A(h\nu - E_g)^n$$

where A is a constant which depends upon the probability of given electronic transitions, hν is the photon energy, *h* is Planck's constant and n is 1 /2 , 2 , 3 /2 , 3 for allowed direct, allowed

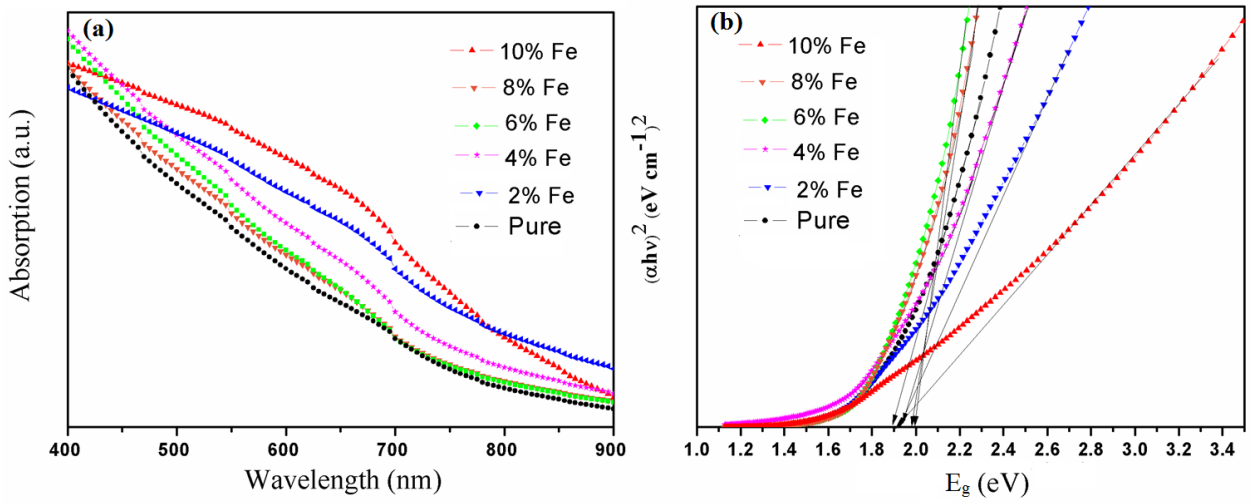

Figure 3.4 (a) UV-Visible absorption spectra and (b) plot between $(\alpha h\nu)^2$ and E_g for $Cd_{1-x}Fe_xSe$ ($0 \leq x \leq 0.1$) nanoparticles

indirect, forbidden direct and indirect transitions, respectively. Figure 3.4 (b) shows the variation of $(\alpha h\nu)^2$ as a function of energy of pure and doped CdSe nanoparticles. E_g was calculated by extrapolating line in the spectra and it has been found to vary between 1.90–1.97 eV. Bulk CdSe has band gap of 1.72 eV corresponding to absorption edge at 714 nm [137]. The observed spectra show a clear blue-shift in pure as well as Fe-doped CdSe nanoparticles as compared to their bulk

counterpart. Reason may be attributed to quantum confinement of an electron-hole pair (exciton) for the observed blue-shift in absorption spectra.

3.1.4.2 PL analysis

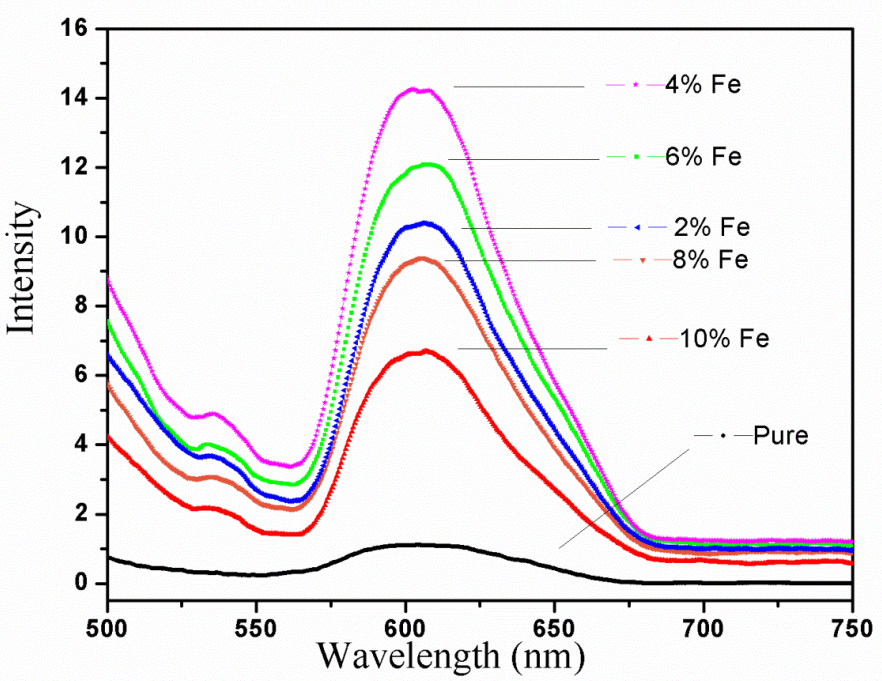

Figure 3.5 PL spectra of $Cd_{1-x}Fe_xSe$ ($0 \leq x \leq 0.1$) nanoparticles, at excitation wavelength of 480 nm

Figure 3.5 shows room temperature PL spectra of pure and Fe-doped CdSe nanoparticles. The sharp peak observed at ~ 614 nm may correspond to band gap or defects in CdSe nanoparticles. However, no variation in peak position has been observed with the increase in Fe-doping concentration. The obvious reason for unchanged peak position is due to the fact that PL bands are not associated with Fe ions but with the shallow impurities and native defects in CdSe nanoparticles. The intensity of this peak has been found to first increase up to 4 % doping concentration and then show decrease with further increase in Fe-doping concentration. The

increase in emission intensity with doping concentration may be attributed to shallow region trapped electron-hole pairs or excitons [138]. However, decrease in intensity after 4 % doping is due to quenching by Fe, whose state acts as an electron trapping center that leads to non-radiative band edge recombination. The non-radiative band edge recombination increases in comparison to radiative band edge recombination at higher Fe-doping concentration, which results in decrease of emission intensity. There is an additional emission peak observed at ~ 537 nm in PL spectra and it is attributed to radiative transition of Fe dopant to ground state [139]. This peak is absent in pure CdSe sample and its intensity increases with Fe-doping concentration.

3.1.5 Raman spectroscopy analysis

Raman spectroscopy is a powerful tool to investigate the structural properties of nanomaterials. The shifting of Raman peaks can be associated with changes in structure, particle size, nature of defects etc. [140, 141]. Figure 3.6 shows Raman spectra of pure and Fe-doped CdSe nanoparticles. In pure CdSe nanoparticles, 1LO (longitudinal optical) and 2LO (its overtone) phonon modes have been observed at 209 and 414 cm^{-1}, which is in corroboration with literature [142]. Traces of additional peaks denoted by (♦) could be attributed to the presence of vibrational mode of –Se–Se–Se– chains [143]. The increase of Fe-doping concentration leads to decrease in values of 1LO and 2LO phonon modes (red-shift), along with appearance of additional broad peak marked by (*) as shown in Figure 3.6. The appearance of broad additional peak (beyond 4% Fe) can be ascribed to the secondary phase of iron selenides, which is in agreement with XRD analysis [144]. The red-shift of 1LO and 2LO modes with increase in Fe-doping concentration can be explained by phonon confinement in nanoparticles [141]. In present study, doping led to decrease of particle size as revealed by TEM analysis. The decrease of particle size

resulted in increase of phonon confinement. This led to peak broadening as well as shifting of phonon modes with increasing Fe-doping concentration in CdSe nanoparticles.

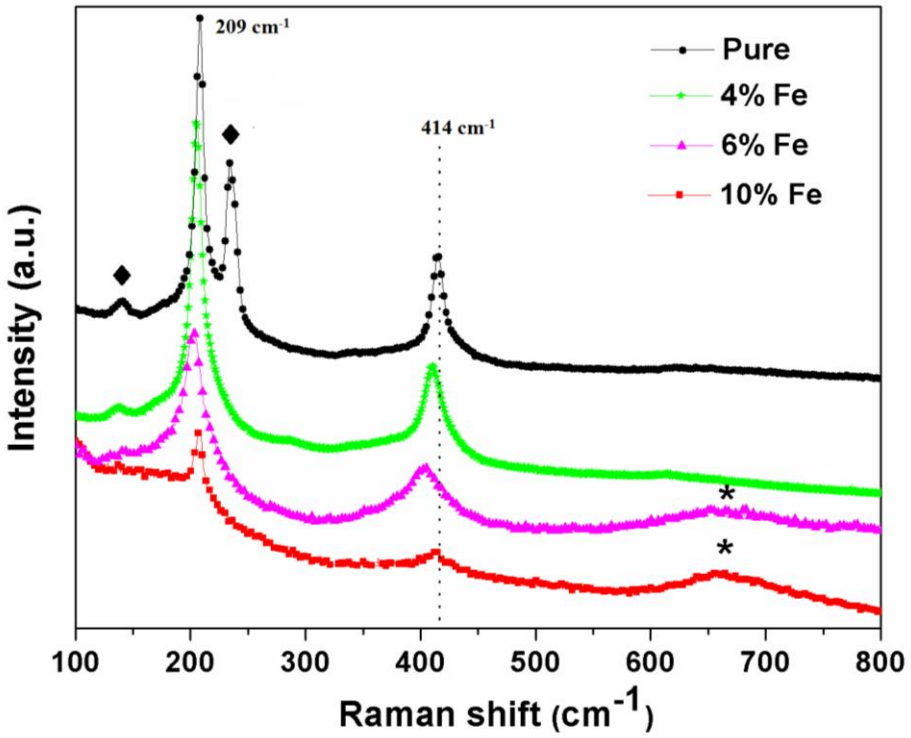

Figure 3.6 Raman spectra of $Cd_{1-x}Fe_xSe$ (x = 0.0, 0.04, 0.06, 0.1) nanoparticles

3.1.6 ESR analysis

ESR is an effective tool to explore ferromagnetism in transition metal doped semiconductors [145-147]. Figure 3.7 shows ESR spectra of pure and Fe-doped CdSe nanoparticles, recorded at room temperature. A broad resonance signal has been observed in pure CdSe which could be attributed to presence of defects in nanoparticles [67]. The careful analysis of spectra reveals the overlapping of two signals in doped nanoparticles, as shown in Figure 3.7 (b). The spectra can be fitted well to Gaussian signal-A and Lorentzian signal-B (Figure 3.7 (b)). Similar results have also been reported in literature previously [146, 147], wherein the signal-A can be attributed to

the ferromagnetic resonance arising due to Fe^{2+}-Fe^{2+} exchange interactions in doped nanoparticles. The signal-B can be attributed to substitutional presence of uncoupled Fe^{3+} ions in host nanoparticles. ESR analysis indicates the presence of Fe ions in mixed oxidation states i.e. Fe^{2+} / Fe^{3+}.

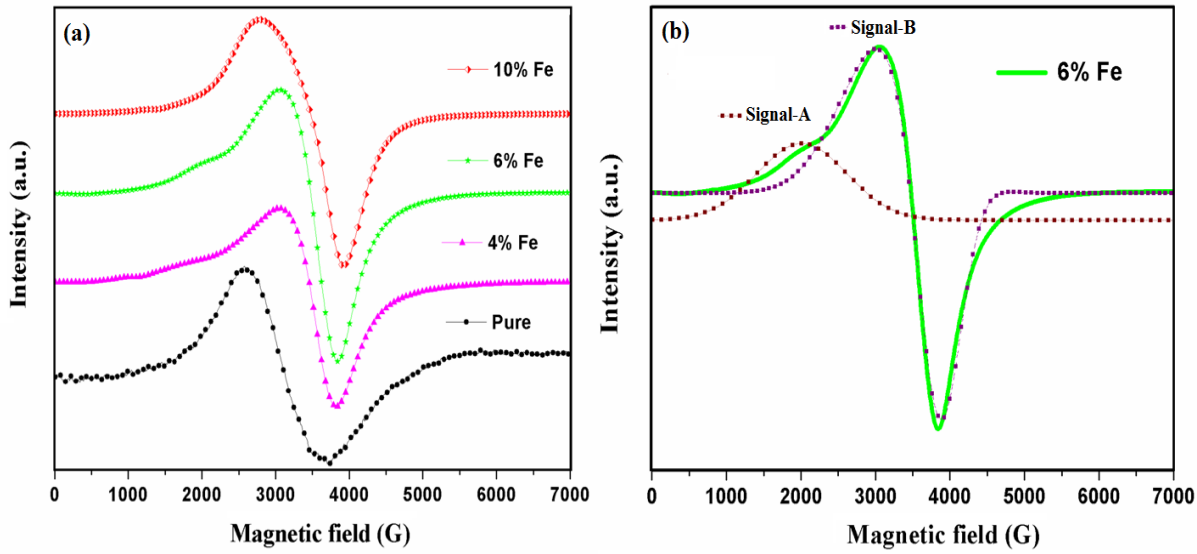

Figure 3.7 ESR spectra of $Cd_{1-x}Fe_xSe$ (x = 0.0, 0.04, 0.06, 0.1) nanoparticles

The *g*-values have been calculated using equation [138],

$$g = \frac{h\gamma}{\mu_B H}$$

where, *h* is Planck's constant, γ is the microwave frequency and μ_B is the Bohr magneton. The *g*-values corresponding to signal-B have been found to be 2.28, 2.04, 2.04 and 2.04 for pure, 4%, 6% and 10% Fe-doped CdSe nanoparticles, respectively. The *g*-value of signal-A has been found to be 2.21. The *g*-values >2 is a clear signature of ferromagnetism in pure and doped nanoparticles.

3.1.7 Magnetic analysis

The magnetic properties of $Cd_{1-x}Fe_xSe$ nanoparticles were determined by SQUID at room temperature. It is well known that bulk CdSe is diamagnetic in nature with susceptibility (χ) value (-0.334×10^{-6} emu $g^{-1}Oe^{-1}$) [148]. But as we move from bulk to nano, CdSe no longer remains diamagnetic. There occur ferromagnetic/paramagnetic transitions depending upon various parameters such as defects, reduced size or due to presence of capping agent [68, 149].

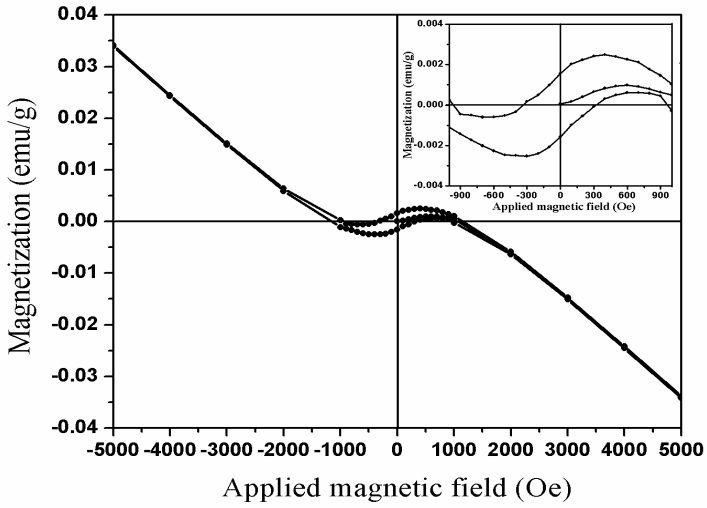

Figure 3.8 Room-temperature M-H hysteresis curve for CdSe nanoparticles. The inset shows expanded view of lower field region

Sundaresan et al. [69] reported that all inorganic nanoparticles exhibit ferromagnetism naturally. Figure 3.8 illustrates room-temperature ferromagnetic behavior of pure CdSe nanoparticles capped with SDS. The magnetization versus applied field behavior of pure and Fe-doped CdSe nanoparticles is shown in Figure 3.9. The observed magnetic behavior in synthesized samples are in well correlation with previous report on Fe-doped CdSe nanoparticles [70], but considerable enhancement in saturation magnetization value has been observed in present data.

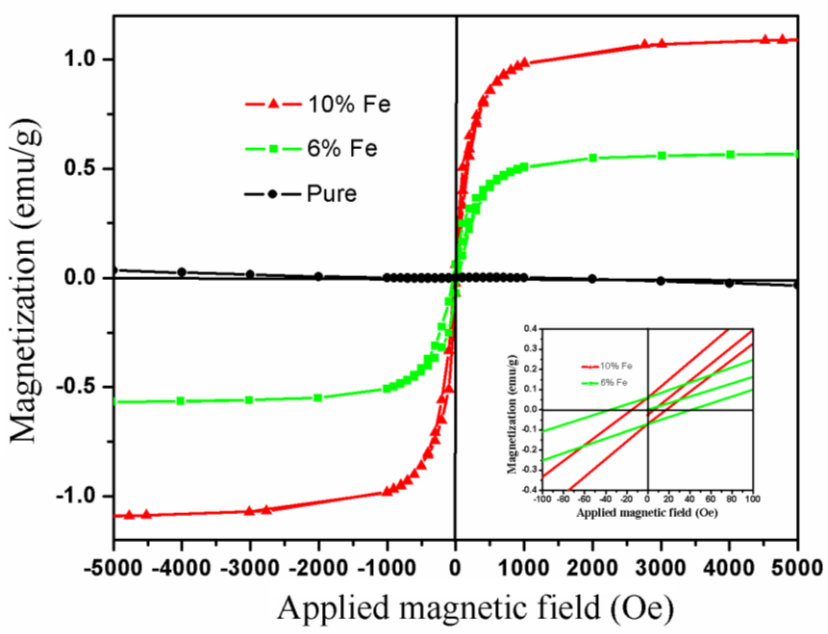

Figure 3.9 Magnetization versus applied field (M – H) hysteresis curves for $Cd_{1-x}Fe_xSe$ (x = 0.00, 0.06 , 0.10) nanoparticles at room temperature

The earlier report on Fe-doped CdSe nanoparticles exhibit cubic phase but in the present case, hexagonal phase has been observed which could be a possible reason for enhancement of ferromagnetism [150]. The presence of extra phase of $FeSe_2$ does not contribute towards ferromagnetism in Fe-doped CdSe nanoparticles as it is generally non-magnetic in nature [151]. Coercivity (H_c), retentivity (M_r), saturation magnetization (M_s) and susceptibility (χ) values are listed in Table 3.1. It is clear from the values summarized in table that saturation magnetization value increases with increase in Fe-doping concentration.

Table 3.1 The observed magnetic parameters for $Cd_{1-x}Fe_xSe$ (x =0.00, 0.06, 0.10) CdSe nanoparticles

Sample	**H_c (G)**	**M_r (emu/g)**	**M_s (emu/g)**	**χ = M/H (emu/g.G)**
Pure	325.37	1.5×10^{-3}	0.002	0.006×10^{-4}
6% Fe	39.45	72.9×10^{-3}	0.520	4.929×10^{-4}
10% Fe	15.37	61.4×10^{-3}	1.007	9.820×10^{-4}

Firstly, exchange interactions between Fe^{2+}-Fe^{2+} ions may be responsible for observed ferromagnetism in these nanoparticles, which is well in agreement with ESR analysis. Secondly, ESR spectra indicates presence of Fe^{3+} ions in host CdSe nanoparticles. The charge imbalance between Fe^{3+} and Cd^{2+} ions can give rise to more number of defects which leads to formation of bound magnetic polarons (F-centers). The increase of Fe-doping concentration increases bound magnetic polarons (F-centers), which in turn increases saturation magnetization. Third possibility is the large surface area of nanoparticles leads to the alignment of more number of magnetic dipoles in the same direction. Therefore, the increase in saturation magnetization is probably due to the presence of Fe and large surface area of nanoparticles.

3.2 Structural, optical and magnetic properties of Co-doped CdSe nanoparticles

In this section, the series of $Cd_{1-x}Co_xSe$ (x = 0.00, 0.05, 0.10 and 0.15) nanoparticles have been discussed. The details of synthesis procedure are described in chapter 2. The structural, optical and magnetic properties of pure and Co-doped nanoparticles have been measured. The obtained results and their discussion have been given below:

3.2.1 Structural and phase analyses

The structure, phase purity and crystallite size of nanoparticles were determined from XRD patterns, as shown in Figure 3.10. All diffraction peaks corresponding to pure CdSe nanoparticles have been found to be in good agreement with standard JCPDS card no. 19-0191, depicting the formation of zinc blende phase with cubic structure.

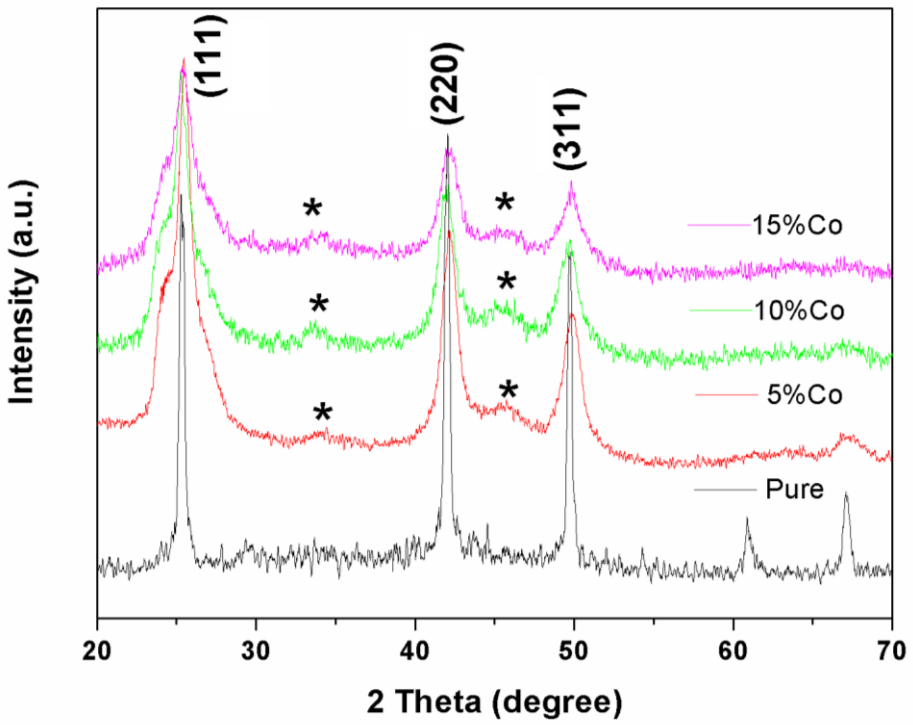

Figure 3.10 XRD patterns of pure, 5%, 10% and 15% Co-doped CdSe nanoparticles

The diffraction peaks at 2θ (degree) values of 25.40, 42.02, 49.84 correspond to (111), (220), (311) planes of cubic CdSe. The extra peaks observed at 2θ (degree), 34.43, 45.92 in all the doped samples are related to cobalt diselenide ($CoSe_2$) (JCPDS card no. 09-0234). The considerable peak broadening has been observed with Co doping concentration. The lower ionic radius of Co^{2+} (0.72 Å) ions as compared to Cd^{2+} (0.97Å) ions, generates compressive strain in host nanoparticles leading to peak broadening in XRD pattern. The peak broadening in XRD patterns may arise due to several other reasons such as smaller crystallite size, instrumental error, fast scanning [107]. As in present case, proper precautions have been taken into account during scanning such as instrument calibration with standard samples and slow scan rate. Therefore, observed broadening is due to strain and smaller crystallite size, where their contribution to peak broadening is independent of each other. Therefore, total broadening can be written as sum of these two as $\beta_{total} = \beta_{strain} + \beta_{crystallite}$ size and can be calculated using Williamson-Hall (W-H) equation [152],

$$\beta_{total} \cos\theta = \frac{1}{D} + \frac{\eta \sin\theta}{\lambda}$$

where η is the effective strain present in material, D is the average crystallite size, λ is the wavelength of x-ray radiation, β is the full width at half maxima, and θ is the diffraction angle.

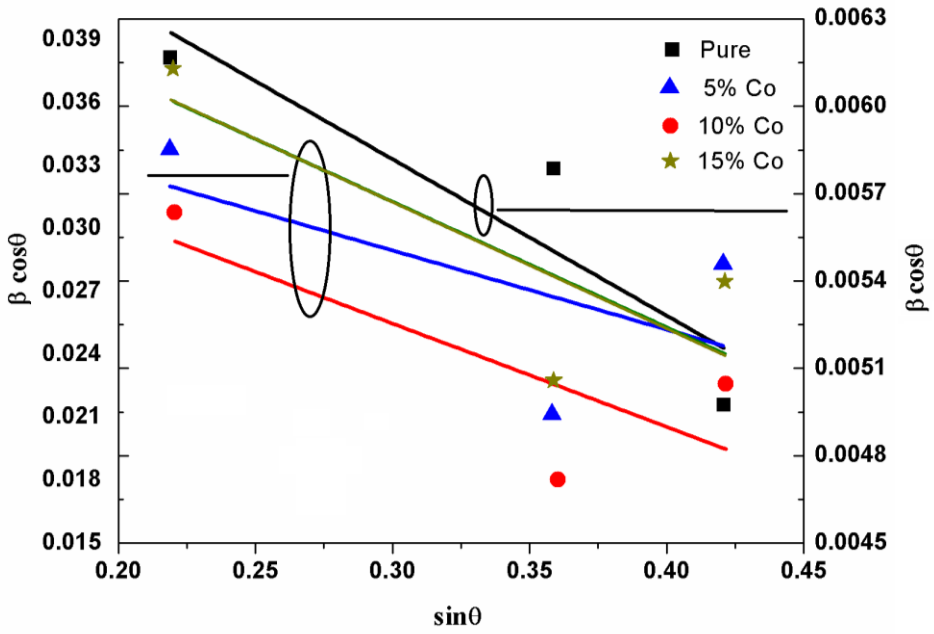

Figure 3.11 W-H plot for pure and Co-doped CdSe nanoparticles

Table 3.2 The calculated values of average crystallite size, average particle size and strain of pure and Co-doped CdSe nanoparticles

Co content (Wt %)	**Average crystallite size from XRD *D* (nm)**	**Average particle size from TEM (nm)**	**Strain *η***
0	20.7	41.2	0.00537
5	3.8	9.5	0.03769
10	3.6	8.9	0.04933
15	3.1	7.5	0.05988

Negative slopes of pure and Co-doped CdSe nanoparticles as shown in Figure 3.11 indicate the presence of effective compressive strain in crystal lattice. Table 3.2 shows

calculated values of strain, crystallite sizes from XRD and TEM. The higher magnitude of slope with incorporation of Co in CdSe suggests enhancement in strain and reduction in crystallite size.

3.2.2 Compositional analysis

The compositional analysis has been done using EDS in order to confirm the elements and quantify their percentage composition, as shown in Figure 3.12. The peaks of cadmium

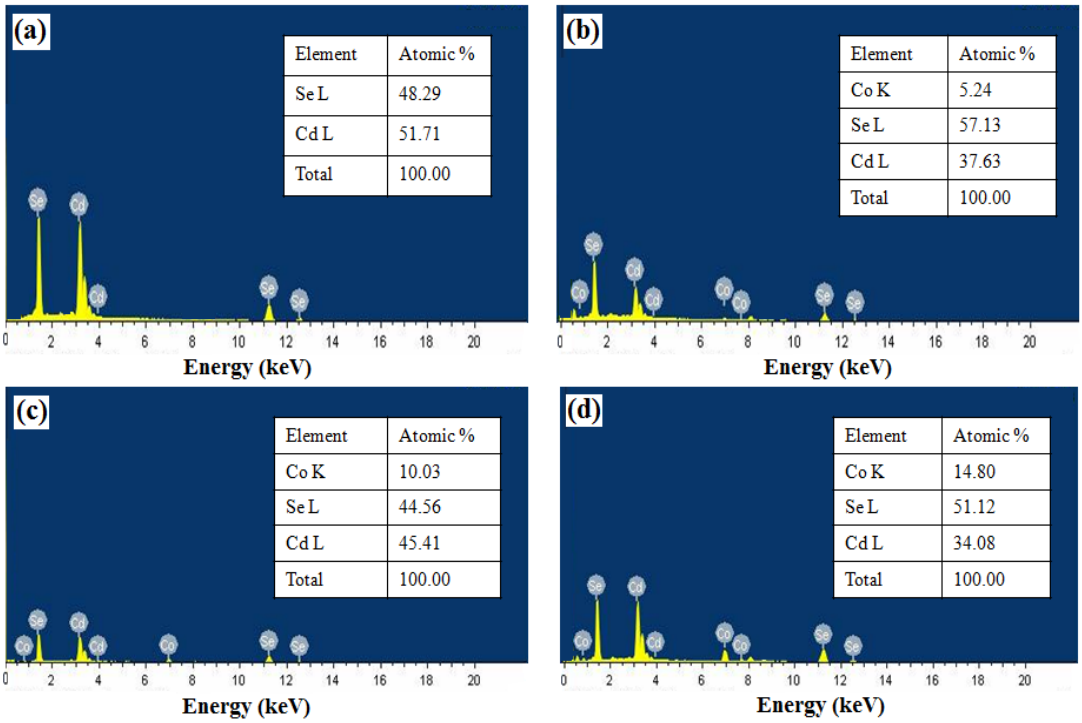

Figure 3.12 EDS spectrum of (a) pure (b) 5%, (c) 10% and 15% Co-doped CdSe nanoparticles

(Cd), cobalt (Co) and selenium (Se) have been observed, which confirm the presence of Co in host CdSe nanoparticles. EDS measurement reveals 5.24%, 10.03% and 14.80% Co for 5%, 10%

and 15% doping concentration, consistent with the weight percent of Co added. Also, no traces of any other impurity element have been observed in the samples.

3.2.3 Morphological analysis

From Figure 3.13, it is clear that pure CdSe nanoparticles exhibit a mixed morphology of spherical, faceted and rod-shaped. Further, doping of Co leads to formation of spherical CdSe nanoparticles with decreased particle size. The shape of nanocrystals depends on concentration of initial precursors and growth kinetics [153].

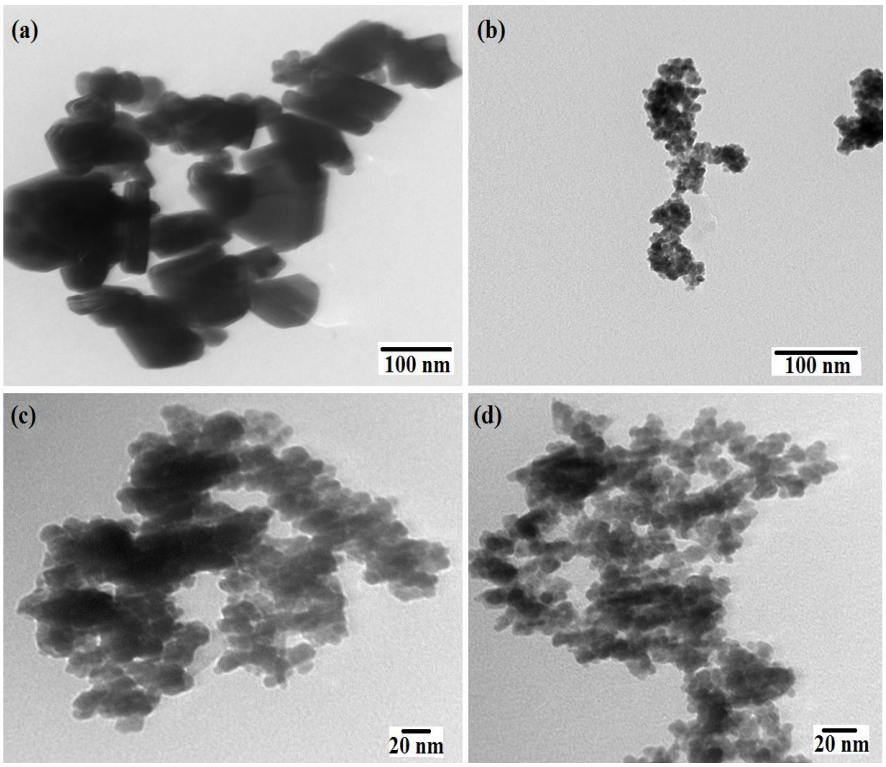

Figure 3.13 TEM micrographs of (a) pure, (b) 5%, (c) 10% and (d) 15% Co-doped CdSe nanoparticles

At high monomer concentration, growth rate of nanocrystals is fast leading to the formation of different shapes. The doping of Co into CdSe nanoparticles limits the growth rate in solution growth process and this favors formation of spherical nanoparticles having smaller particle size [154]. The average particle size of pure, 5%, 10% and 15% Co-doped CdSe nanoparticles has been found to be 41.2, 9.5, 8.9, and 7.5 nm, respectively. Particle size from TEM is consistent with the results obtained from XRD. The irregular shaped nanoparticles for pure CdSe further support the long tail in UV-Visible spectra.

3.2.4 Optical analyses

3.2.4.1 UV-vis. analysis

Figure 3.14 (a) shows UV-visible absorption spectra of pure and Co-doped CdSe nanoparticles. Bulk CdSe has a band gap of 1.72 eV corresponding to absorption wavelength of 714 nm. In the present system, pure CdSe nanoparticles show red-shift, which is due to the band narrowing effect arising from strained anisotropic structure, as well as the scattering of light in different directions or intra-bandgap defect states [155, 99]. A long tail in UV-Visible spectrum has also been observed in pure CdSe nanoparticles, which indicates the formation of faceted or rod like structures [156].

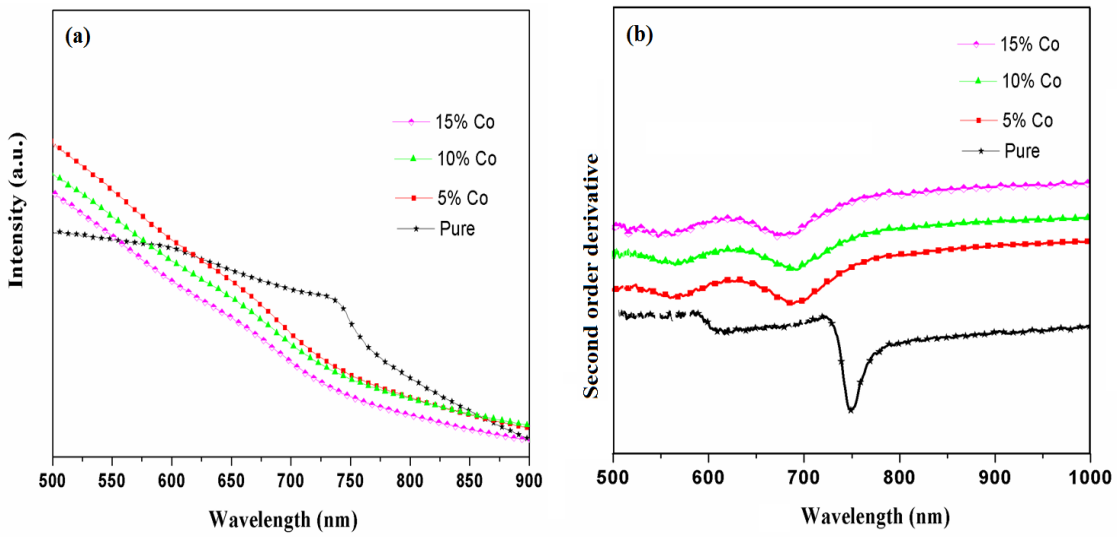

Figure 3.14 (a) UV-visible absorption spectra of pure and Co-doped CdSe nanoparticles and (b) Second-order derivative of the absorption spectra of pure and Co-doped CdSe nanoparticles

However, with Co doping blue-shift has been observed. This can be explained by quantum confinement of electron-hole pairs (excitons), which is dominant when the particle size is less than or comparable to Bohr exciton radius of bulk material. The Bohr exciton radius of CdSe is around 5.5 nm [157]. Hence, CdSe nanoparticles of radii ≤5.5 nm show quantum confinement effect with absorbance maxima shifted towards shorter wavelengths. E_g of synthesized nanoparticles have been calculated using second order derivative of absorption spectra (Figure 3.14 (b)) and it comes out to be 1.65, 1.78, 1.80 and 1.83 eV for pure, 5%, 10% and 15%, respectively. E_g value has been found to be increase with increasing Co-doping concentration, which can be attributed to decrease in particle size.

3.2.4.2 PL analysis

PL emission spectra of pure and Co-doped CdSe nanoparticles have been recorded at room temperature with excitation wavelength of 480 nm, as shown in Figure 3.15. Two broad emission peaks, at 576 and 632 nm, have been observed in emission spectrum. The weak emission peak at 576 nm related to deep trap levels and strong emission peak at 632 nm is due to shallow region trapped electron-hole pairs [158]. The emission from deep trap levels does not change with doping because it is independent of particle size and doping concentration whereas, emission from shallow traps decreases with Co- doping concentration [159]. Co acts as electron trapping center, which leads to non-radiative recombinations. So, it is concluded that Co acts as a quencher impurity in the host CdSe nanoparticles.

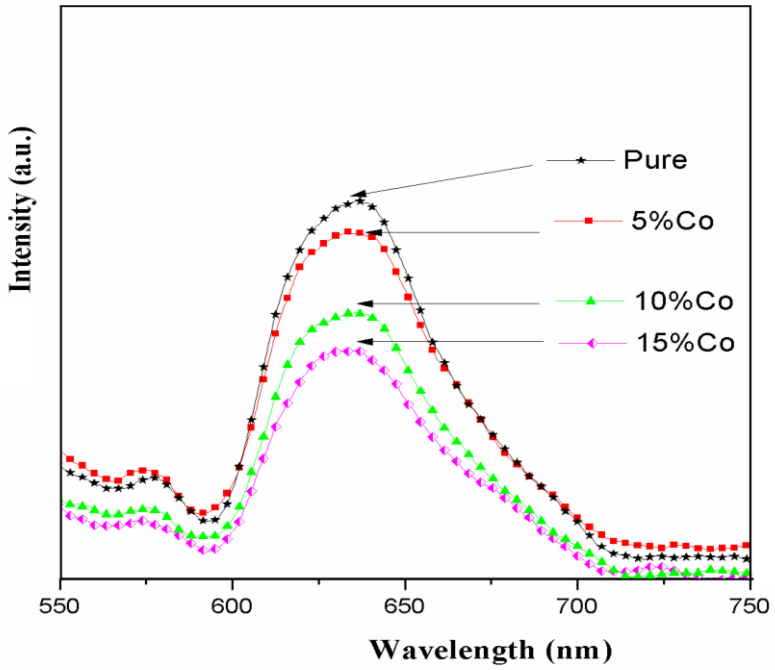

Figure 3.15 PL spectra of pure and Co-doped CdSe nanoparticles recorded at an excitation wavelength of 480 nm

3.2.5 Raman spectroscopy analysis

Figure 3.16 (a) shows room temperature Raman spectra of pure and Co-doped CdSe nanoparticles in the range 100-800 cm^{-1}. The strongest and sharpest peak at 208 cm^{-1} along with weak peak at 418 cm^{-1} can be assigned to 1LO and 2LO phonon modes of CdSe, respectively [142]. However, with increase in Co-doping concentration, peak broadening and decrease in intensity with respect to pure CdSe nanoparticles have been observed (Figure 3.16 (a)). This indicates that Co substitution might be responsible for local disorder in host nanoparticles. Also, doping leads to appearance of new broad peak, as clearly revealed by expanded view of Raman spectra (Figure 3.16 (b)). This additional peak at 680 cm^{-1} can be attributed to cobalt diselenide, which is well in agreement with XRD analysis [160]. The considerable decrease of Raman shift has been observed for 5% Co-doping as compared to 10 and 15% Co-doping concentration. The phonon confinement and lattice strain can play a significant role in the observed increase or decrease of Raman shift [141]. The phonon confinement or tensile strain leads to decrease of Raman shift whereas; compressive stress can possibly result in increase of Raman shift. In present study, 5% Co-doping results in considerable decrease of particle size (as revealed by TEM analysis). The phonon confinement driven decrease of Raman shift has been observed initially. Afterwards, dopant related compressive strain tends to increase Raman shift, contrary to phonon confinement which decreases it.

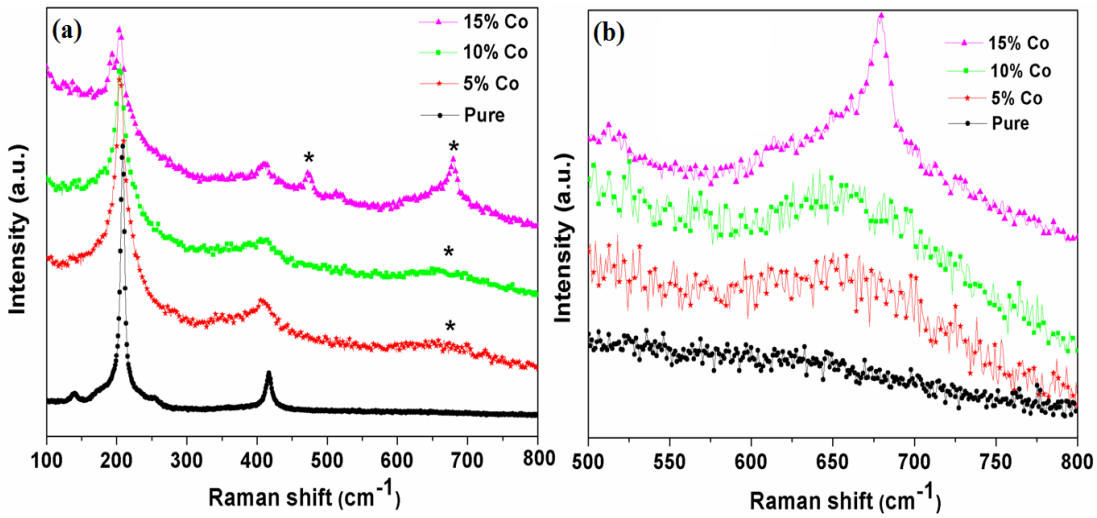

Figure 3.16 (a) Raman spectra of $Cd_{1-x}Co_xSe$ (x = 0.0, 0.05, 0.10, 0.15) nanoparticles (b) expanded view of Raman spectra from 500-800 cm^{-1}

3.2.6 ESR analysis

Figure 3.17 shows ESR spectra of pure and Co-doped CdSe nanoparticles at room temperature. The spectra exhibit broad line width which could be attributed to ferromagnetic resonance due to long range exchange interactions. The *g*-values and N_s participating in resonance (Table 3.3) of pure and doped CdSe nanoparticles have been calculated using equation [138], *g*-value (> 2) reveals ferromagnetic resonance in pure and Co-doped CdSe nanoparticles.

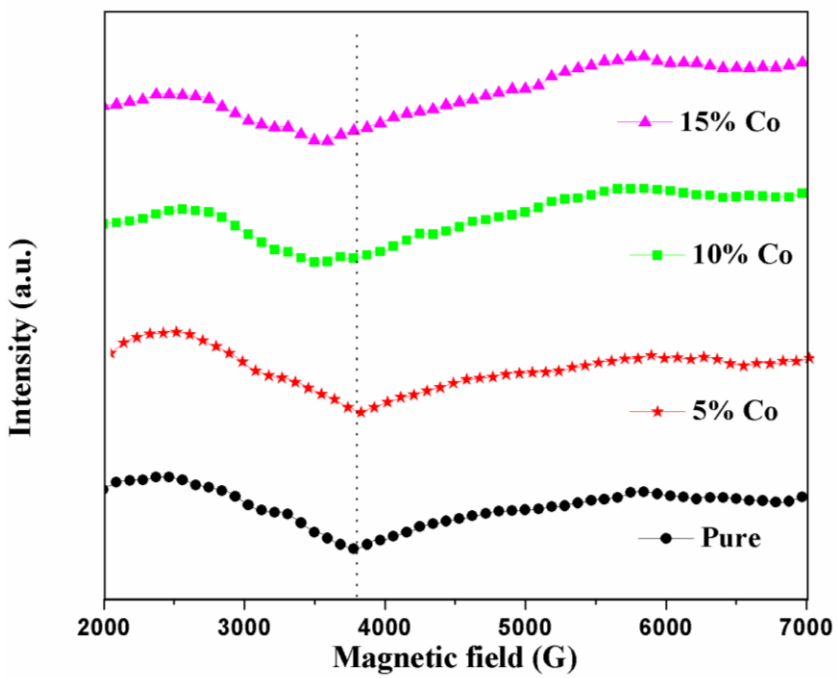

Figure 3.17 ESR spectra of $Cd_{1-x}Co_xSe$ (x = 0.0, 0.05, 0.10, 0.15) nanoparticles

Table 3.3 Lande '*g*' factor, line width (ΔH), and number of spins (N_s) of pure and Ni-doped CdSe nanoparticles

Samples	**g-value**	**Line width, ΔH (G)**	**No. of spins, N_s**
Pure	2.35	1002	3.29×10^{8}
5% Co	2.39	1224	4.34×10^{8}
10% Co	2.43	1326	4.36×10^{8}
15% Co	2.54	1383	3.53×10^{8}

Also, ESR signal indicate the +2 oxidation state of Co^{2+} ions in CdSe nanoparticles [161]. The increase of ΔH and N_s with doping (Table 3.3) is most likely to arise due to ferromagnetic

exchange interactions between closely lying Co^{2+}- Co^{2+} ions. This show the strong exchange interactions between Co^{2+}- Co^{2+} ions which are increasing with Co-doping concentration. However, at 15% Co-doping concentration decrease of N_s has been observed. The reason could be attributed to the strong exchange interactions being antiferromagnetic in nature, at higher doping concentration [162].

3.2.7 Magnetic analysis

Figure 3.18 shows the M-H hysteresis loops of pure and Co-doped CdSe nanoparticles at room temperature. Hysteresis curves with H_c and M_r values, 221, 301, 99, 65Oe and 2.83×10^{-4}, 6.15×10^{-5}, 2.93×10^{-4}, 5.23×10^{-4} emu/g, respectively, have been observed for pure, 5%, 10% and 15% of doping concentration. For pure CdSe nanoparticles, diamagnetic curve (Figure 3.18 (a)) has been obtained, as expected from its intrinsic diamagnetic nature. At a lower magnetic field value, as shown in inset of Figure 3.18 (a), weak ferromagnetism has been observed, which may be attributed to the charge transfer between capping agent and host CdSe nanoparticles or defects [68, 149]. However, universatility of ferromagnetism has been observed in CdSe nanoparticles [69]. The magnetism in doped CdSe nanoparticles may be originated possibly from carrier mediated exchange interactions between delocalized carriers of host and localized d-spins of the Co ions [163]. The secondary phase of $CoSe_2$ does not contribute to observed magnetism in present system but it shows paramagnetism below 4K [164]. Also, origin of observed magnetism in doped CdSe nanoparticles may be attributed to the presence of secondary impurities or phases such as Co_3Se_4, Co_7Se_8, and Co_9Se_8 [165]. However, no such phases have been detected in Raman and XRD analysis within their detection limits.

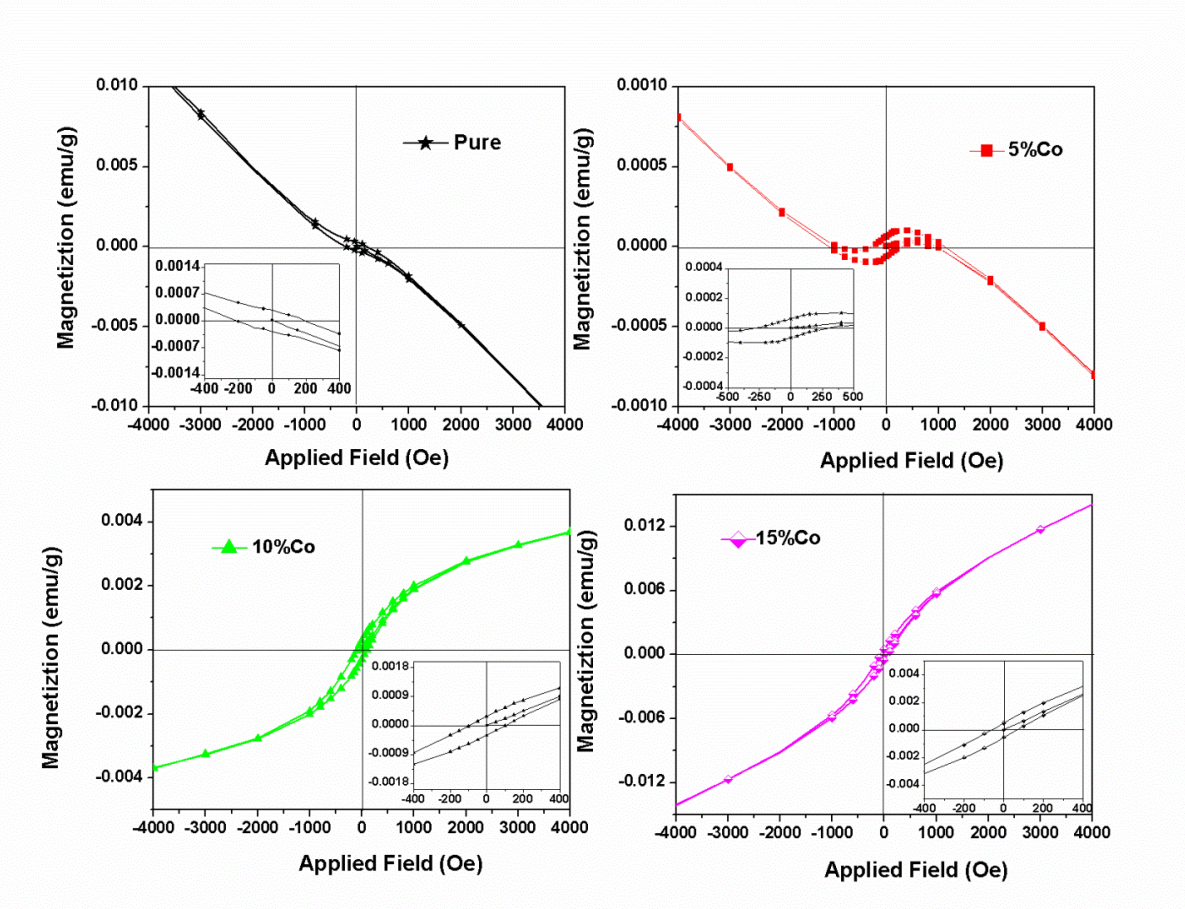

Figure 3.18 M-H curves showing hysteresis of (a) pure, (b) 5%, (c) 10% and (d) 15% Co doping concentration. The inset shows the enlarged view of M-H curve

S-type hysteresis loop has been observed in 5% Co doping concentration which shows the emergence of ferromagnetism in host nanoparticles. Further, diamagnetic contribution arises from the host, which reduces the magnetic moment at higher magnetic field. With increase of doping concentration up to 10%, the ferromagnetic behavior has been observed with weak magnetic moment (Figure 3.18 (c)), which may be due to long range ferromagnetic ordering in Co-doped CdSe nanoparticles. The ferromagnetic loop is not saturated, but noticeable H_c and M_r values have been observed for 10% of Co doping. Further, increase of Co content

beyond 10% led to linearization of M-H hysteresis curve (Figure 3.18 (d)). It indicates that Co-Co superexchange interaction dominates at higher Co-doping concentration, thereby possesses antiferromagnetic character. Hanif et al [62] in 2002 and Archer et al [66] in 2007 reported similar results; the Co-doped CdSe nanoparticles show antiferromagnetic behavior, due to strong sp-d exchange interaction between Co d-orbitals and conduction band of the host CdSe.

3.3 Structural, optical and magnetic properties of Ni-doped CdSe nanoparticles

This section deals with series of $Cd_{1-x}Ni_xSe$ (x = 0.00, 0.02, 0.05, 0.10) nanoparticles. The nanoparticles were synthesized by hydrothermal technique, as discussed in detail in chapter 2. The structural, optical and magnetic properties of pure and Ni-doped nanoparticles were investigated. The obtained results are discussed below:

3.3.1 Structural and phase analyses

Figure 3.19 shows XRD patterns of pure and Ni-doped CdSe nanoparticles. All diffraction peaks are well indexed with hexagonal structure of CdSe (JCPDS card no. 77-2307) having lattice constants a = 4.299 Å and c = 7.010 Å. No indication of secondary phase has been detected in XRD pattern. The average crystallite size of CdSe nanoparticles has been calculated using Scherer's formula [107].

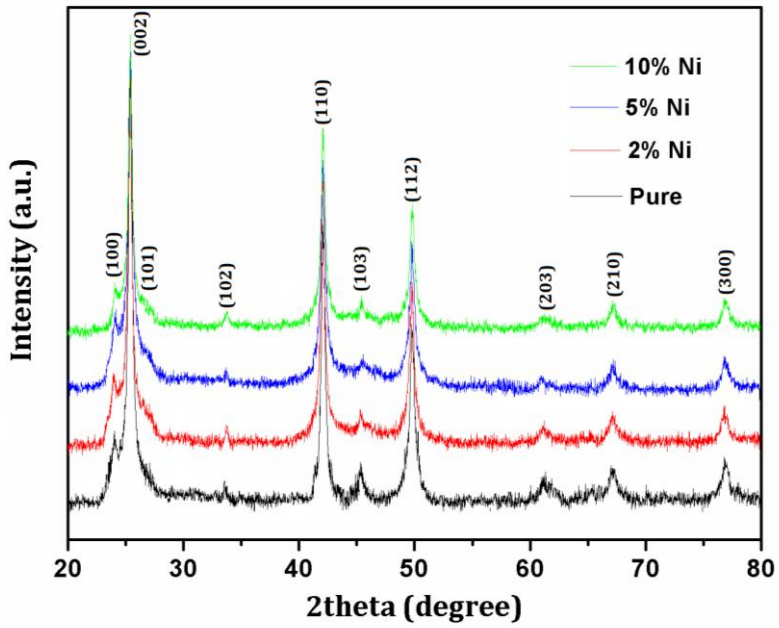

Figure 3.19 XRD patterns of pure and Ni-doped CdSe nanoparticles

The average crystallite size comes out to be 22.67, 21.60, 20.32 and 18.81 nm for pure, 2%, 5% and 10% Ni- doped CdSe nanoparticles, respectively. Further, peak shift towards higher angle ($2\theta_{002}$) and decrease of lattice parameters (a, c) from 4.29 to 4.27 Å and 7.01 to 6.98 Å have been observed with Ni-doping concentration. This could be attributed to smaller ionic radii of Ni^{2+} (0.69 Å) as compared to Cd^{2+} (0.97 Å). The decrease of lattice parameters and peak shift in XRD indicates substitution of Cd^{2+} by Ni^{2+} ions in host CdSe nanoparticles [166, 167].

3.3.2 Morphological analysis

The morphology of synthesized nanoparticles has been studied by TEM, as shown in Figure 3.20. It has been observed that pure and Ni-doped CdSe nanoparticles possess spherical morphology with uniform particles size distribution. However, agglomeration has been observed with increase of Ni-doping concentration, owing to smaller particle size of doped nanoparticles. The average particle size comes out to be 25 nm for pure and 20 nm for 10% Ni-doped nanoparticles. Figure 3.20 (c, d) shows EDS pattern of pure and 10% Ni-doped CdSe nanoparticles. It has been clearly observed in EDS pattern that no impurity element is present in synthesized nanoparticles and also, amount of Cd, Se and Ni is consistent with our experimental plan.

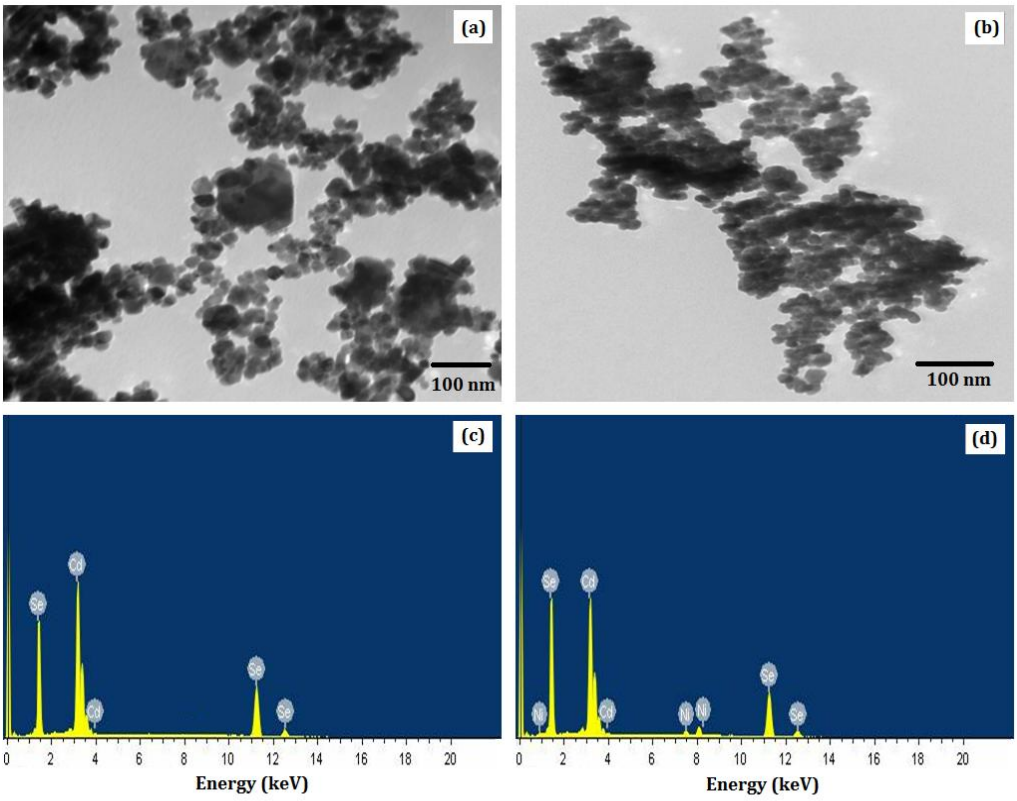

Figure 3.20 TEM images of (a) pure and (b) 10% Ni-doped CdSe nanoparticles, corresponding their EDS patterns (c) and (d), respectively.

3.3.3 Optical analyses

3.3.3.1 UV-vis. analysis

The diffuse reflectance spectroscopy has been used to calculate band gap of synthesized nanoparticles. Figure 3.21 shows the diffuse reflectance spectra of pure and Ni-doped CdSe nanoparticles. The value of band gap energy has been calculated using Kubelka-Munk function [168],

$$F(R) = \frac{(1-R)^2}{2R}$$

where, F(R) is Kubelka-Munk function (equivalent to the absorption coefficient) and *R* is % reflectance. $F(R)^2$ vs hν (eV) has been plotted and linear part of curve has been extrapolated to estimate the band gap values. The band gap values have been calculated to be 1.77, 1.80, 1.82, 1.85 eV for pure, 2%, 5% and 10% Ni-doped CdSe nanoparticles, respectively.

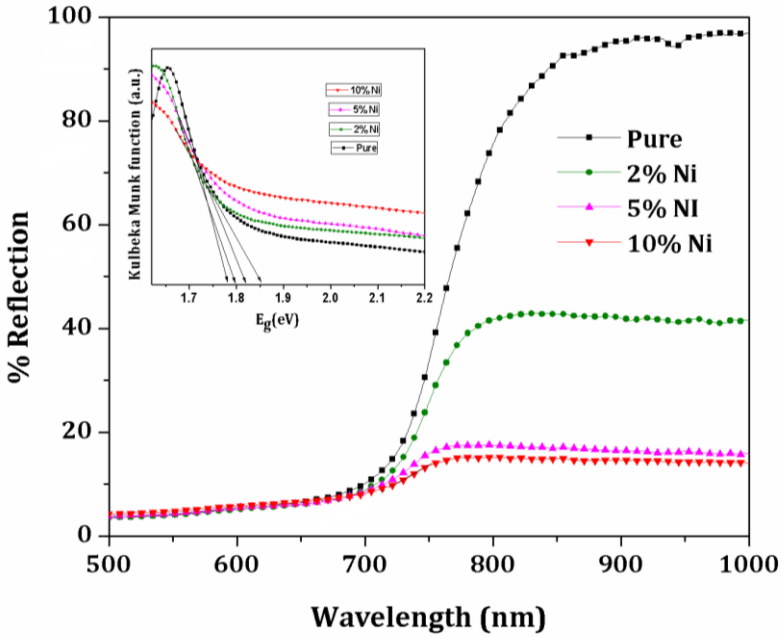

Figure 3.21 The diffuse reflectance spectra of pure and Ni-doped CdSe nanoparticles

The blue-shift has been observed with increase of Ni-doping concentration in CdSe nanoparticles as shown in inset of Figure 3.21. This blue-shift in pure and doped nanoparticles could be attributed to quantum confinement effect as particle size lies in nanometer regime. The quantum confinement effect comes into picture when particles size becomes less than or comparable to Bohr exciton radius (bound electron hole pair). Bohr exciton radius of CdSe is 5.5 nm [169], but in present study the average particle radius from TEM analysis comes out to be greater than 5.5 nm. This can be explained via weak confinement and strong confinement regimes [166, 167]. In weak confinement the particle radius is greater than Bohr exciton radius. The motion of exciton

is restricted owing to nanometric size and this leads to blue shift in absorption spectra. However, strong confinement effects start dominating when radius of nanomaterials becomes less than Bohr exciton radius for a given material. The weak confinement effect can possibly be the reason behind observed blue-shift in pure and Ni-doped CdSe nanoparticles.

3.3.3.2 PL analysis

Figure 3.22 shows PL emission spectra of pure and Ni-doped CdSe nanoparticles at room temperature. The broad emission spectra have been observed in pure and doped nanoparticles. The broad spectra could be attributed to the convolution of two peaks (687 and 717 nm) marked as E1 and E2, in Figure 3.22.

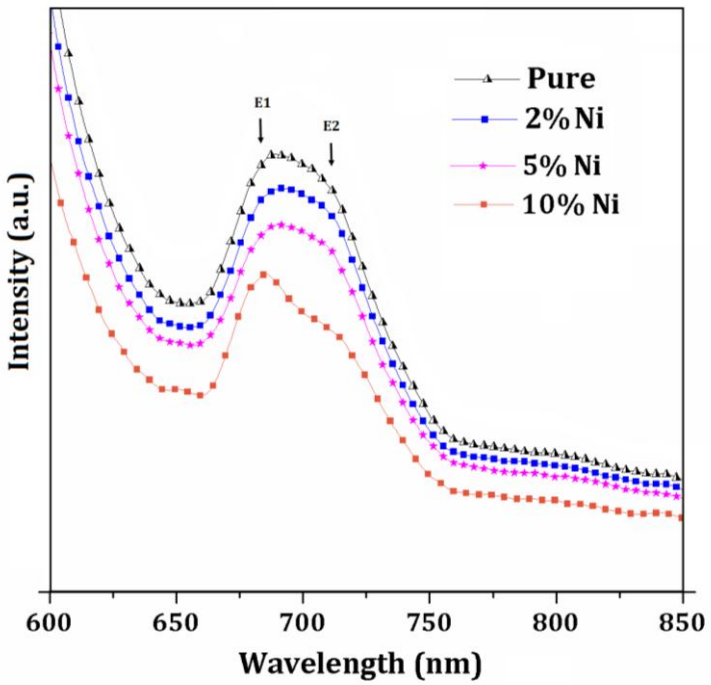

Figure 3.22 PL emission spectra of pure and Ni-doped CdSe nanoparticles

These are related to intrinsic defects or deep level vacancies (V_{Cd} –V_{Se}), which are characteristics of wurtzite structure. The origin of peaks E1 and E2 can be explained via two different types of V_{Cd} – V_{Se} associates in wurtzite structure. One is oriented along hexagonal *c*-axis and other is oriented along basal Cd–Se bond direction [170]. It is clear from Figure 3.22 that increase of Ni-doping concentration leads to more number of intrinsic defects in host CdSe nanoparticles. No variation in peak position has been observed with increase in Ni-doping concentration. The obvious reason for unchanged peak position is that PL bands are associated with intrinsic defects in CdSe nanoparticles. However, decrease in emission intensity with doping is due to quenching by Ni, whose state acts as an electron trapping center that leads to non-radiative recombinations [171].

3.3.4 Raman spectroscopy analysis

To explore the effect of Ni-doping concentration on structural and vibrational properties, Raman scattering of pure and doped nanoparticles have been measured at room temperature, as shown in Figure 3.23 (a). The spectrum reveals peak position at about 208 and 416 cm^{-1} which can be attributed to 1LO and 2LO phonon modes of CdSe, respectively [142]. Also, Raman spectra shows two peaks marked by (*), these correspond to presence of Se phase [143]. No indication of any secondary phases related to Ni or Cd have been observed in Raman spectra. However, doping induced red-shift of Raman peaks have been observed as shown in Figure 3.23 (b). According to Heisenberg's uncertainty principle, position and momentum of a particle is related by following relation

$$\Delta x \times \Delta p \geq \frac{\hbar}{2}$$

where Δx is the particle size, Δp is the phonon momentum and $\hbar$ is the reduced Planck's constant. As the particle size decreases, phonon confinement and momentum distribution increases. This results in red-shifting and broadening of Raman peaks [172]. The other reason of peak shifting can be ascribed to the strain in nanomaterials. As, in present study ionic radii of Ni^{2+} (0.69 Å) is smaller as compared to Cd^{2+} (0.97 Å). This led to considerable lattice strain driven Raman peak shifting in Ni-doped CdSe nanoparticles. Further, electron-phonon coupling strength have been calculated using Haung-Rhys parameter [173]

$$\frac{1LO}{2LO} = \frac{2}{S}$$

S-values have been calculated to be 0.298, 0.359, 0.593, and 0.642 for pure, 2%, 5% and 10% Ni-doping, respectively.

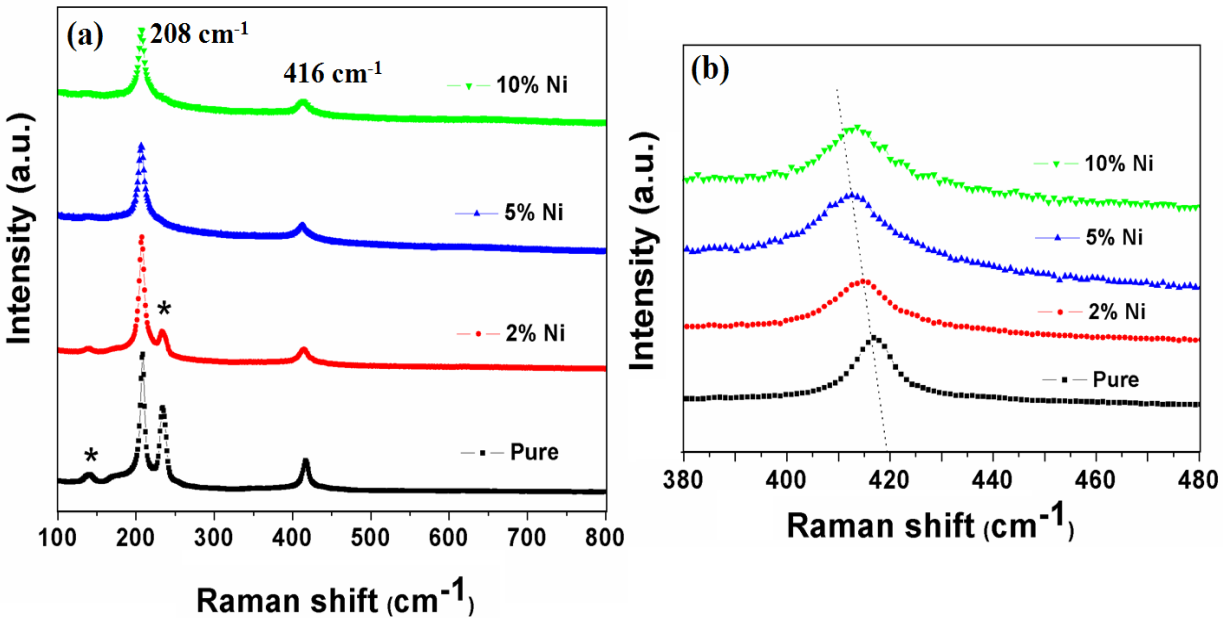

Figure 3.23 (a) Raman spectra of pure and Ni-doped CdSe nanoparticles (b) enlarged view of Raman spectra

The increase of *S*-factor shows enhanced electron-phonon coupling due to changes in sp-d exchange interactions with Ni-doping in CdSe nanoparticles.

3.3.5 ESR analysis

Figure 3.24 shows ESR spectra of pure and Ni-doped CdSe nanoparticles at room temperature. The spectra exhibit broad line width which could be attributed to ferromagnetic resonance due to long range exchange interactions. The *g*-values (Table 3.4) of pure and doped CdSe nanoparticles have been calculated using equation [138], There is considerable deviation of *g*-values from free electron *g*-value (~ 2.001) in pure and Ni-doped CdSe nanorods. In previous reports a broad paramagnetic resonance signal has been observed (*g*-value~ 2) for pure CdSe nanoparticles, owing to the presence of defects or capping agent [70, 138,].

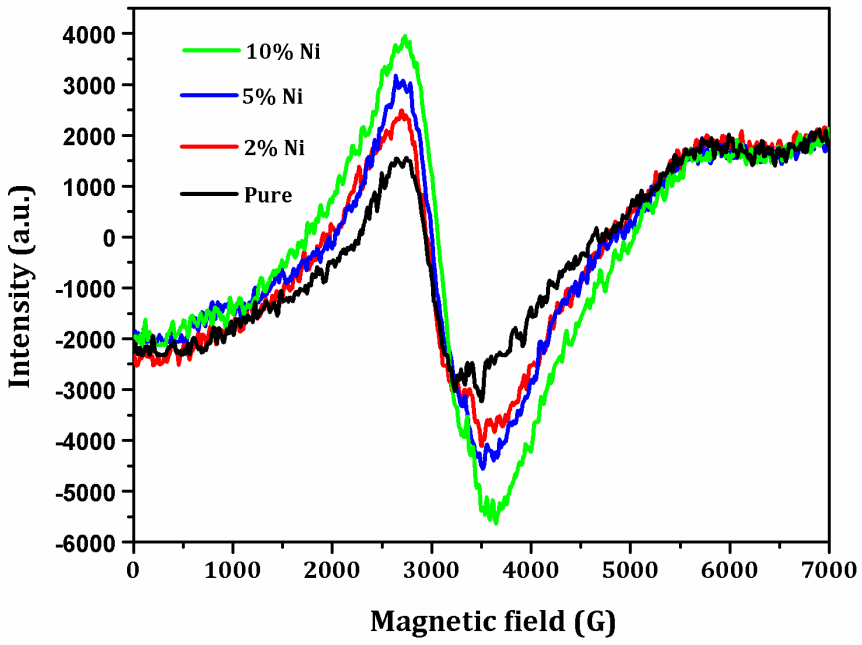

Figure 3.24 shows the ESR spectra of pure and Ni-doped CdSe nanoparticles at room temperature.

But in present study comparatively good resonance signal has been observed with *g*-value of 2.31, indicating ferromagnetism in pure CdSe nanoparticles. In doped nanoparticles, Ni^{2+} has $^3A_2$ (F) ground state in octahedral coordination and degenerate ^3F ground state splits as a consequence of crystal field resulting in *g*-value of 2.23 [174]. So, with increase of doping concentration decrease of *g*-values has been observed and this further intimates that Ni exist in +2 oxidation state in doped nanoparticles. N_s participating in the resonance can be calculated (Table 3.4), by using the formula [138]

$$N_s = 0.285\ \mathrm{I}\ (\Delta H)^2$$

where 'I' is the peak-to-peak height (arbitrary units) and ΔH is the line width (in G). It has been observed that number of spins participating in the ferromagnetic resonance increases with increase of Ni-doping concentration.

Table 3.4 g-value, ΔH, peak to peak intensity and N_s of pure and Ni-doped CdSe nanoparticles

Samples	**g-value**	**Line width, ΔH (G)**	**Peak to peak intensity**	**No. of spins, N_s**
Pure	2.31	645	4272	5.065×10^8
2% Ni	2.29	782	6140	1.070×10^9
5% Ni	2.25	847	7358	1.504×10^9
10% Ni	2.23	879	9184	7.095×10^9

3.3.6 Magnetic analysis

Figure 3.25 shows M-H loops at room temperature for pure and Ni-doped CdSe nanoparticles. The ferromagnetic M-H curves have been obtained for pure and doped nanoparticles. Further, at

higher applied fields linearization of M-H curves takes place indicating diamagnetic contribution of host CdSe. The values of saturation magnetization have been found to be 0.54, 1.36, 1.76 and 2.48 memu/g for pure, 5 and 10% Ni-doped CdSe nanoparticles. It is well known that the CdSe in bulk form is a diamagnetic material having 'χ' = - 2.25 × 10^{-7} emu $g^{-1}Oe^{-1}$ [148]. The ferromagnetism in pure CdSe nanoparticles has been reported, owing to the presence of capping agent or surface defects or vacancies in host CdSe nanoparticles [67-69]. The intrinsic defects have been observed in PL analysis, which play a vital role in the observed RTFM in present study.

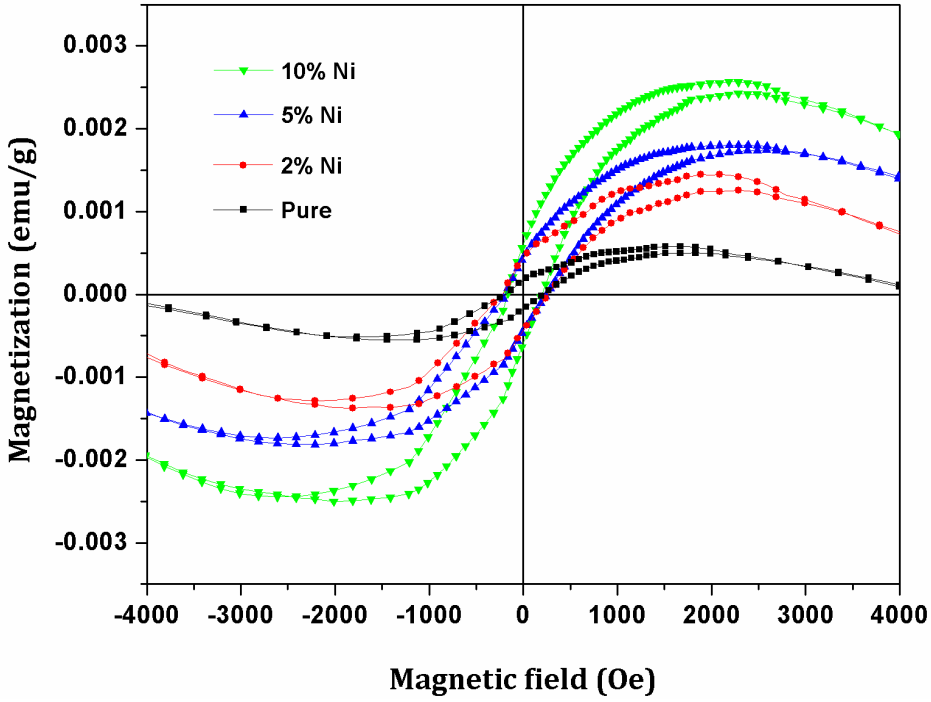

Figure 3.25 Room temperature M-H curves of pure and Ni-doped CdSe nanoparticles

The increase of ferromagnetic character has been observed with Ni-doping concentration. However, origin of observed ferromagnetism at room temperature in transition metal-doped II-VI materials is not clear and a matter of debate till date. There are number of possibilities for the observed RTFM in Ni-doped CdSe nanoparticles such as Ni metal, its extra phases or intrinsic

ferromagnetism. Metallic Ni is a ferromagnetic element in Free State, but it is unable to retain its metallic nature during the synthesis, leading to formation of secondary phases of Ni such as NiSe, NiO, Ni_2O and Ni_2O_3. NiSe is diamagnetic in bulk, whereas bulk NiO exhibits antiferromagnetism (Neel temperature ~ 520 K) or super-paramagnetism at nanocrystalline range [175]. Also, the value of saturation magnetization for Ni nanoparticles has been reported to be 40 emu/g [176]. But in present study saturation magnetization values were found to be much lower, excluding their role in observed RTFM. As evident from PL study, increase of doping concentration leads to increase of defects. The charge carriers trapped in defects lead to ferromagnetic ordering in pure CdSe nanoparticles. Secondly, trapped carriers acts as a medium for indirect ferromagnetic resonance between Ni^{2+} ions. This leads to ferromagnetism in Ni-doped CdSe nanoparticles, which arises from long range ferromagnetic resonance between Ni^{2+}-Ni^{2+} ions. The ferromagnetic ordering has been further supported by ESR analysis. We conclude that the intrinsic defects and indirect ferromagnetic coupling between Ni^{2+}-Ni^{2+} ions both are responsible for observed ferromagnetism in the present study. Therefore, observed RTFM in Ni-doped CdSe nanoparticles is intrinsic in nature; this can be useful for future spintronics device applications.

3.4 Structural, optical and magnetic properties of Fe-doped CdSe nanorods

In this section, the series of $Cd_{1-x}Fe_xSe$ (x = 0.00, 0.02, 0.05 and 0.10) nanorods have been discussed. The details of synthesis procedure are described in chapter 2. The structural, optical and magnetic properties of pure and Fe-doped nanorods have been measured. The obtained results and their discussion have been given below:

3.4.1 Structural and phase analyses

XRD patterns of pure and Fe-doped CdSe nanorods are shown in Figure 3.26. The observed diffraction peaks have been well indexed to standard hexagonal structure having wurtzite phase of CdSe (JCPDS card no. 77-2307). No secondary or impurity phase related peaks have been observed in XRD patterns, demonstrating the substitutional presence of dopant in host CdSe nanorods. The various parameters, as calculated from XRD pattern have been displayed in Table 3.5. The intensity of diffraction peaks decreases with increase of Fe-doping concentration, indicating the loss of crystallinity due to lattice distortion. On the incorporation of Fe ions into the crystal lattice of host CdSe nanorods, alteration of lattice parameters occurs pertaining to smaller ionic radius of Fe^{3+} (0.64 Å) ion as compared to Cd^{2+} (0.97 Å) ion.

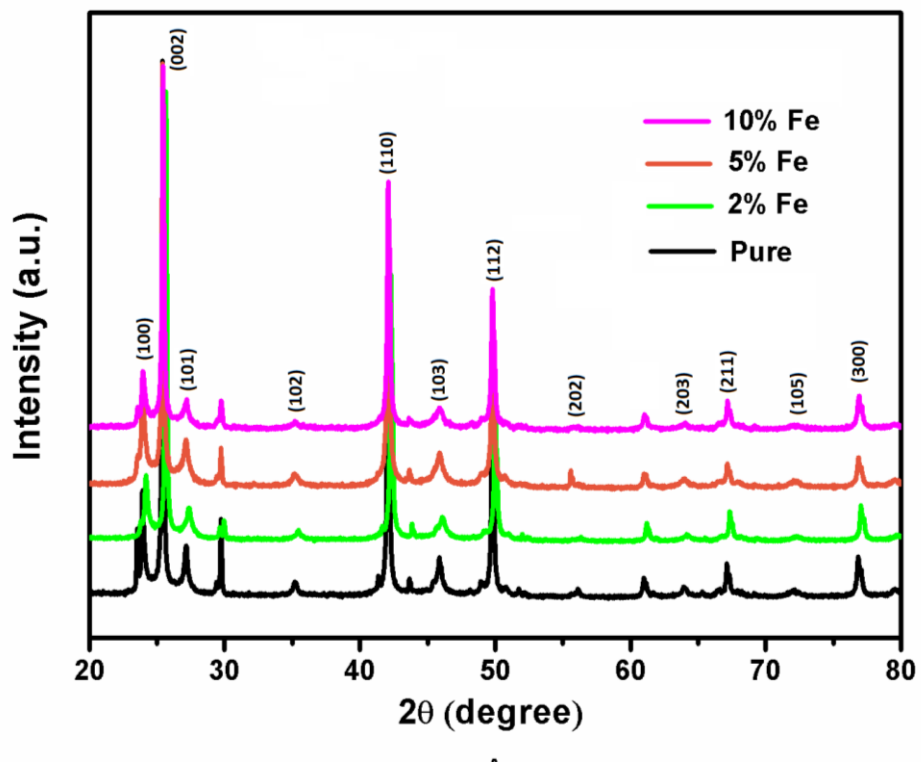

Figure 3.26 XRD patterns of pure and Fe-doped CdSe nanorods

The lattice parameters (a, c) have been calculated using [107]:

$$\frac{1}{d^2} = \frac{4}{3}\left(\frac{h^2 + hk + k^2}{a^2}\right) + \frac{l^2}{c^2}$$

where, *d* is inter-planar spacing, *h*, *k* and *l* are the Miller indices. The doping of Fe ions, further, leads to increase of lattice strain as shown in Table 3.5, which has been calculated using Williamson Hall equation [152]

$$\frac{\beta cos\theta}{\lambda} = \frac{1}{\varepsilon} + \frac{\eta sin\theta}{\lambda}$$

where, ε is effective crystallite size, η is strain, λ wavelength of x-ray used, β is full width at half maximum and θ is angle of diffraction. XRD results clearly reveal that Fe^{3+} ions have replaced Cd^{2+} ions, without the formation of any secondary phase in host CdSe nanorods.

Table 3.5 The unit cell parameters (a, c, d and V), $2\theta_{002}{}^{o}$, FWHM, peak intensity and η of synthesized nanorods

Sample	**2θ**	**FWHM**	**d-spacing (Å)**	**a=b (Å)**	**c (Å)**	**Cell volume (Å)**	**Lattice strain (η)**	**Peak intensity**
Pure	25.418	0.1564	3.5014	4.288	7.002	111.493	0.00632	8793
2% Fe	25.656	0.1596	3.4694	4.249	6.938	108.473	0.00641	8568
5% Fe	25.460	0.1599	3.4956	4.275	6.981	110.486	0.00802	6720
10% Fe	25.440	0.1709	3.4983	4.284	6.996	111.190	0.00707	4912

3.4.2 Morphological and elemental analysis

Figure 3.27 (a), (b) and (c) show the TEM images of pure, 5% and 10% Fe-doped CdSe nanorods, respectively. TEM images clearly reveal that pure and doped nanorods are of approximately same dimensions. The diameter and length of pure and doped nanorods have been found to be in the range of 8-15 and 100-140 nm, respectively. Figure 3.27 (d) shows the HRTEM image of 5% Fe-doped CdSe nanorods. The clear lattice fringes with no evidence of secondary phase and Fe metal clustering is well evident in HRTEM analysis, which confirms the single crystalline nature of synthesized nanorods. This has been further confirmed from the SAED pattern as shown in Figure 3.27 (e). The *d*-spacing (marked by arrows) corresponding to (101) plane of hexagonal CdSe has been estimated to be 3.3 Å, as shown in Figure 3.27 (d). EDS

analysis further shows that no impurity element is present in synthesized nanorods and amount of Cd, Se and Fe is in good agreement with our experimental plan. These observations together with XRD analysis confirm the doping of Fe in the CdSe nanorods.

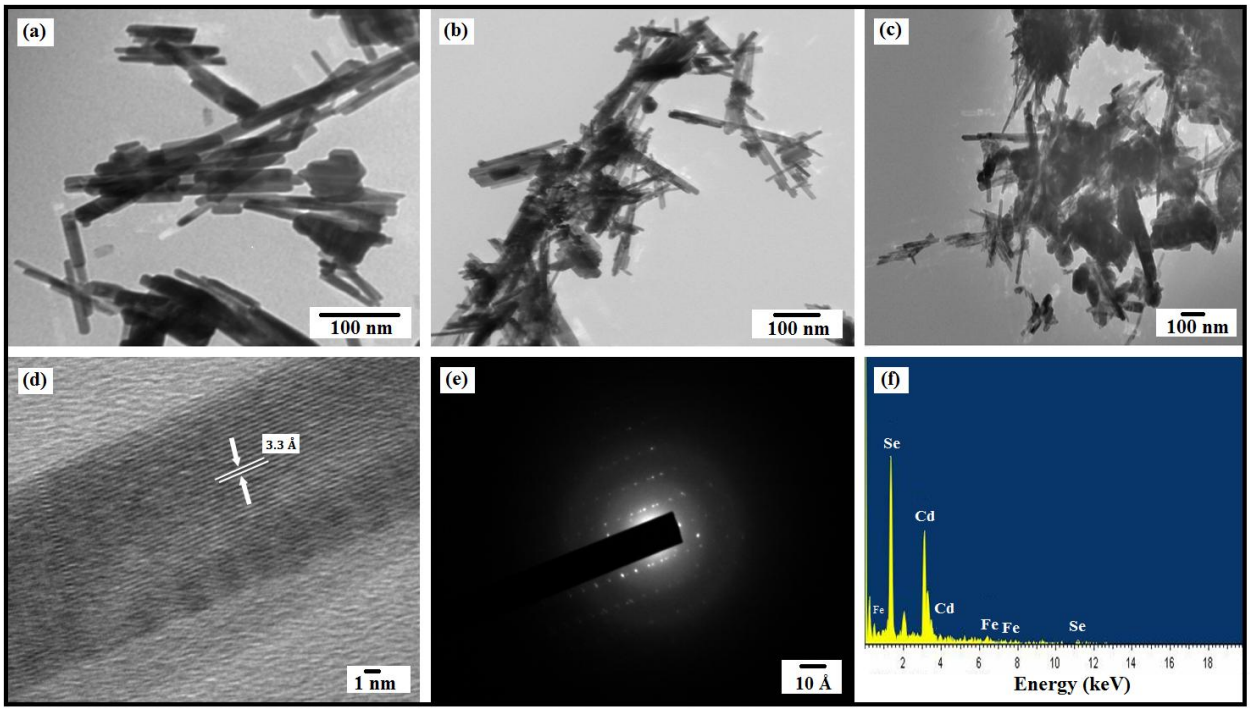

Figure 3.27 TEM images of (a) pure (b) 5% and (c) 10% Fe-doped CdSe nanorods, (d) HR-TEM (e) SAED and (f) EDS images of 5% Fe-doped CdSe nanorods

3.4.3 Optical analysis

3.4.3.1 UV-vis. analysis

In order to study the optical properties of pure and Fe-doped CdSe nanorods, diffuse absorption was performed at room temperature, as shown in Figure 3.28. E_g of pure and doped nanorods has been calculated, using second order derivative of the absorption spectra. E_g values have been found to be 1.57, 1.59, 1.60 and 1.61 eV for pure, 2%, 5% and 10% Fe-doping concentration, respectively. The bulk CdSe has a band gap of 1.74 eV, corresponding to absorption band edge

at 714 nm [98]. In present study, red-shift has been observed in the band gap of pure CdSe nanorods as compared to their bulk counterpart. This shift in E_g can be well explained by the presence of intra-bandgap defect states or strained anisotropic structure of host nanorods [99, 155]. The blue-shift in band gap has been observed with Fe-doping concentration. The observed blue-shift cannot be ascertained to quantum confinement, owing to bigger size of synthesized nanorods. The deformation of band structure due to Fe-doping may be considered as the probable reason for blue-shift of E_g [177].

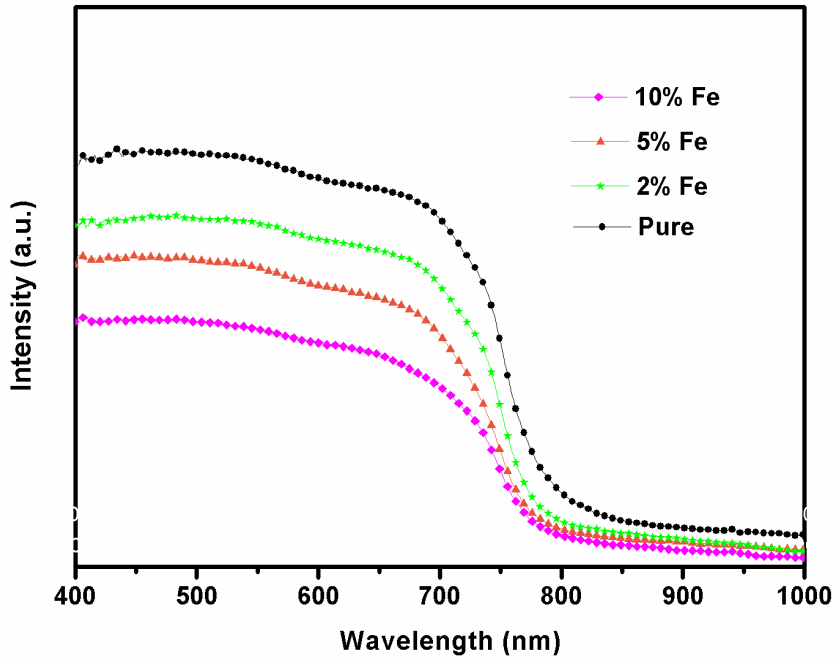

Figure 3.28 UV-visible absorption spectra of pure and Fe-doped CdSe nanorods

3.4.3.2 PL analysis

Figure 3.29 show PL emission spectra of pure and Fe-doped CdSe nanorods. A broad emission peak has been observed at 682 nm which can be related to near band edge emission in CdSe nanorods [178]. However, no change in peak position and decrease of emission intensity has

been observed with Fe-doping. The obvious reason for unchanged peak position is that the emission bands originate from near band edge defects in nanorods [179]. Whereas, decrease in intensity is due to quenching by Fe, whose state acts as an electron trapping center that leads to non-radiative band edge recombination.

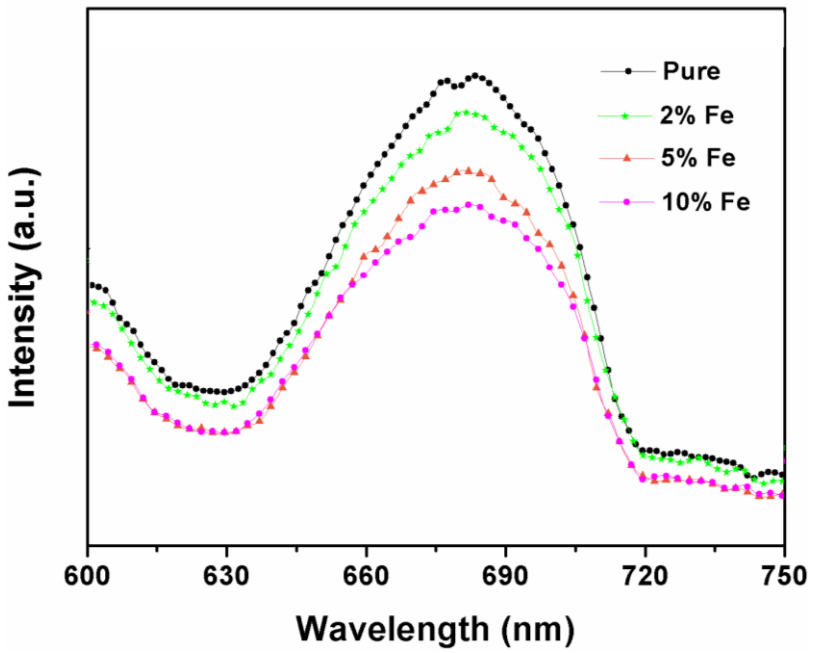

Figure 3.29 PL emission spectra of pure and Fe-doped CdSe nanoparticles

3.4.4 Raman spectroscopy analysis

Figure 3.30 shows the room temperature Raman spectra of pure and Fe-doped CdSe nanorods. The phonon frequencies of longitudinal optical (1LO) and its overtone (2LO) mode for pure CdSe nanorods have been found to be at 216 and 418 cm^{-1}, respectively. The obtained values are in well agreement with reported values in the literature for bulk CdSe, i.e., 209 and 418 cm^{-1} for 1LO and 2LO phonon modes, respectively [142]. The blue-shift of 1LO phonon mode has been observed in pure CdSe nanorods with respect to its bulk counterpart. Also, a considerable blue-shift in 5 and 10% Fe-doped nanorods is present as compared to the undoped one. This may

possibly be due to the phonon confinement or lattice strain [141]. In the present study, phonon confinement cannot give rise to blue-shift of 1LO phonon mode due to large size of CdSe nanorods. Also, no blue-shift of E_g due to quantum confinement effect in UV-visible spectra has been observed. Considering above mentioned observations, it can be concluded that phonon confinement does not give rise to blue-shift, rather the strain arising due to lattice contraction is real cause for observed blue-shift in pure and Fe-doped CdSe nanorods; this is also consistent with XRD analysis. The 1LO phonon mode peak position follows the same trend as that of lattice strain in XRD analysis.

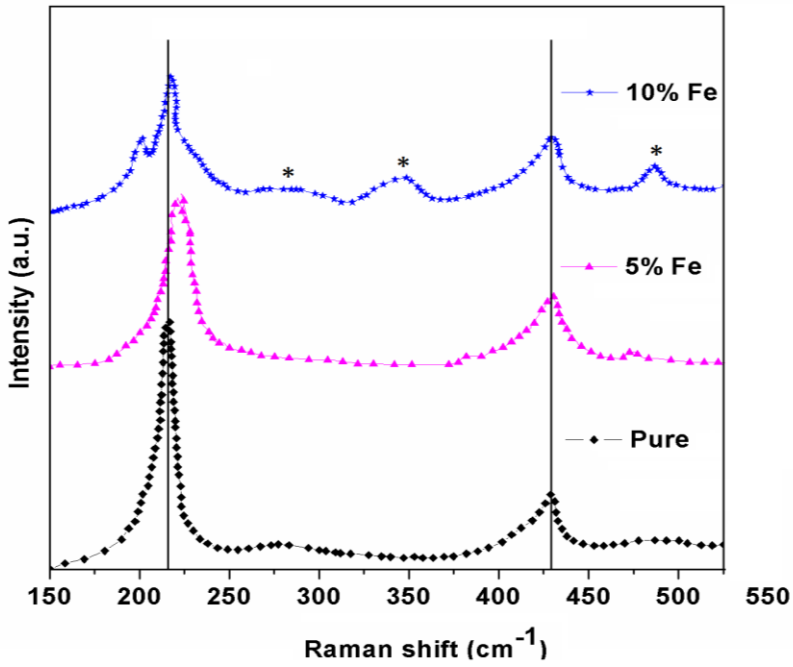

Figure 3.30 Raman spectra of pure and Fe-doped CdSe nanorods with Ar^+ source excitation.

The relative shift of 1LO phonon mode can be related to strain by relation given below [180].

$$\frac{\Delta\omega}{\omega} = \left(1 + 3\frac{\Delta a}{a}\right)^{-\gamma} - 1$$

where, ω is the frequency of the crystal vibrations, a is lattice parameter, γ = 1.1 (Grüneisen parameter) for 1LO phonon mode in CdSe. It has been found that the strain ($\Delta a/a$) values in pure, 5% and 10% Fe-doped CdSe nanorods comes out to be 0.27%, 0.58% and 0.37%, respectively. The surface reconstruction related strain in pure, and doping related strain in Fe-doped CdSe nanorods can be attributed to observed blue-shift of 1LO phonon mode. Along with 1LO and 2LO phonon modes, the broad Raman bands have been observed at 275 and 490 cm^{-1} in pure CdSe nanorods. Their origin can be related to the lattice defects, which usually appears in defective crystals. Also, additional Raman peaks have been observed in 5% and 10% Fe-doped CdSe nanorods. This can be attributed to enhanced electron-phonon coupling due to defects or to localized vibrational modes (LVM) induced by the Fe-doping. These activate additional phonon modes arising due to relaxation of Raman selection rules [181].The peaks consecutive to 1LO and 2LO modes have possibly arisen from the coupled optical-acoustical phonon modes. However, peaks marked by asterisk (*) may have originated from LVM due to Fe doping in CdSe nanorods. Similar LVMs have also been observed for transition metal doped II-VI semiconductor materials [182].The crystalline quality, defects and Fe-doping strongly influences electron-phonon coupling strength, which have been calculated using Haung-Rhys parameter, *S*, [173]. *S*-values have been calculated to be 0.612, 1.101, 1.105 for pure, 5%, and 10% Fe-doping, respectively. The increase of *S* factor shows enhanced electron-phonon coupling due to changes in sp-d exchange interactions with Fe-doping in CdSe nanorods.

3.4.5 ESR analysis

ESR measurements have been performed in order to determine the oxidation state of dopant and origin of magnetism in Fe-doped CdSe nanorods. Figure 3.31 shows room temperature ESR spectra of pure and doped CdSe nanorods. A broad signal has been observed for pure CdSe

nanorods having *g*-value ~ 2, which is attributed to the presence of defects in host CdSe nanorods [70, 138]. In ESR spectra, two signals have been observed, a broad (signal A) and narrow (signal B), as shown in Figure 3.31.

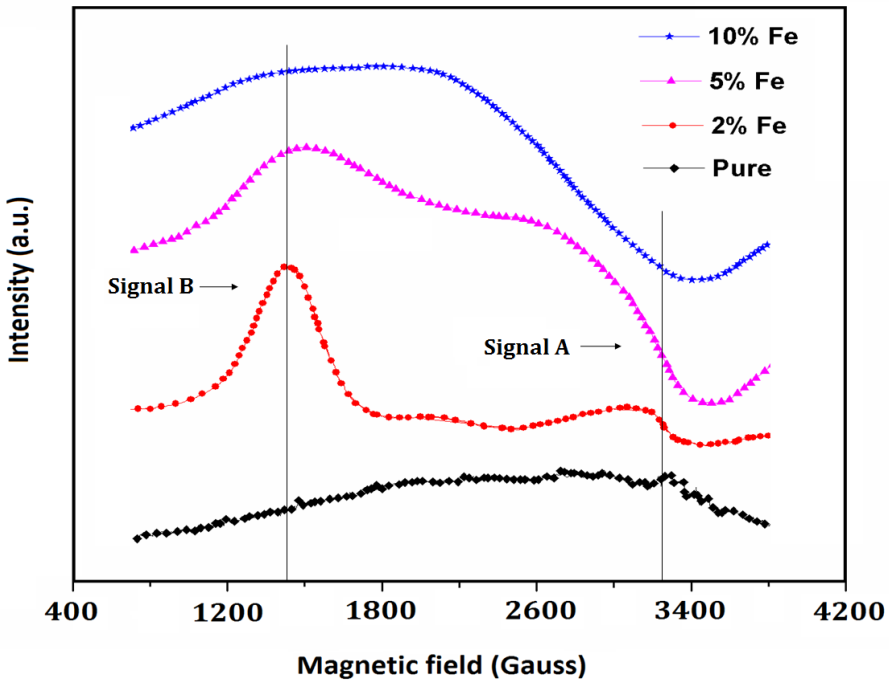

Figure 3.31 ESR spectra of pure and Fe-doped CdSe nanorods

Table 3.6 The g-values, number of spins (N_s) and saturations magnetization (M_s) of synthesized nanorods

Sample	**g-value (Signal A)**	**g-value (Signal B)**	**ΔH (G)**	**$N_s \times 10^3$**	**M_s**
Pure	2.00	….	….	…..	0.026
2% Fe	2.02	4.8	162	7.4795	0.143
5% Fe	2.14	4.4	792	178.77	0.263
10% Fe	2.31	4.3	1098	343.59	0.415

Table 3.6 shows *g*-values of pure and doped CdSe nanorods, as calculated using equation [138], The *g*-values have been found to be 2.02, 2.14 and 2.31, respectively, for 2, 5 and 10% Fe-doped CdSe nanorods. The *g*-value greater than 2 is a clear signature of ferromagnetism in all doped CdSe nanorods. Also, signal broadening with doping can be associated with long range ferromagnetic ordering between Fe^{3+} ions, thereby giving rise to ferromagnetism in doped CdSe nanorods. The shifting of signal A with Fe-doping is due to the presence of non-homogeneous local magnetic field in host nanorods [183]. The additional peaks corresponding to *g*-values of 4.8, 4.4 and 4.3 have been observed for 2%, 5% and 10% Fe-doping concentration, respectively. This can be credited to the presence of isolated Fe^{3+} ions in distorted tetrahedral sites of host CdSe nanorods. The N_s contributing to resonance signal A, have been calculated by using the formula [138], and is tabulated in Table 3.6. It has been observed that the number of spins contributing to the ferromagnetic resonance corresponding to signal A increases with increasing Fe-doping concentration. Also, the signal intensity increases with Fe-doping concentration. Increase of signal intensity shows enhanced ferromagnetic resonance, in accordance with '*S*' parameter in Raman spectroscopy and magnetic data. ESR signal intensity decreases if signal comes from the clustering of Fe ions or interaction between Fe^{3+} ions through the selenium bridges [183]. ESR analysis indicate the strong interaction of the Fe^{3+} ions with the host CdSe nanorods.

3.4.6 Magnetic analysis

Room temperature M-H has been carried out for pure and Fe-doped CdSe nanorods, as shown in Figure 3.32. The ferromagnetic hysteresis loops have been observed for pure and doped CdSe nanorods.

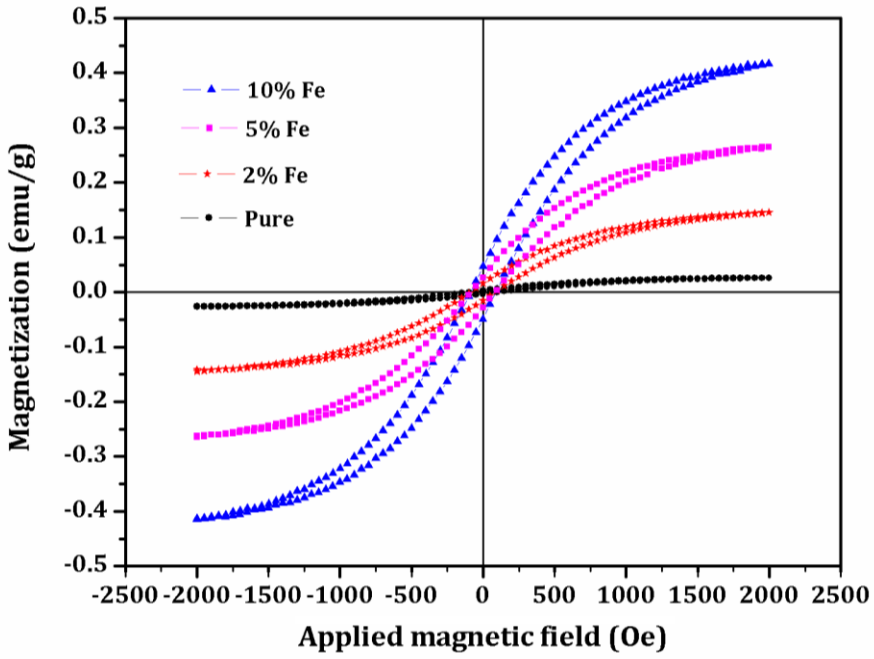

Figure 3.32 M-H of pure and Fe-doped CdSe nanorods measure at room temperature.

The pure CdSe nanorods exhibit M_s and H_c values of 0.026 emu/g and 89 Oe, respectively. The ferromagnetism in CdSe nanomaterials can be related to various parameters such as nature of capping agent, defects and size of the synthesized material [67-69]. In present work, no capping agent has been used and size of the synthesized nanorods is too large to contribute ferromagnetism. Thus, both of these factors can be ruled out to be the cause of origin of ferromagnetism in CdSe nanorods. The probable reason of ferromagnetism in CdSe nanorods is the presence of defects, where bulk CdSe is a diamagnetic material in nature [148]. The increase of M_s values have been observed with Fe-doping concentration. To explain the origin of ferromagnetism in Fe-doped CdSe nanorods, one must consider all possible reasons such as Fe based oxides, Fe clustering or formation of secondary phases. XRD and Raman analysis, indicate that there is no Fe related oxides or formation of secondary phases. Also, Fe based oxides such as FeO, Fe_2O_3 and Fe_3O_4 are antiferromagnetic and superparamagnetic or ferrimagnetic in

nature, respectively [135, 184, 185]. Therefore, these oxides do not contribute to observed ferromagnetism in the present study. In general, Fe ions are in +2 oxidation state if the host CdSe nanorods are in defect-free state. ESR measurement indicates that Fe ions are present in +3 oxidation state. The ferric ions strongly interact with each other and exchange interactions increase with Fe-doping concentration, as corroborated with ESR and Raman analysis. The bound magnetic polaron (F-center exchange mechanism) has been used to explain the ferromagnetism in Fe-doped CdSe nanorods and this mechanism demands exchange interactions between dopant ions via electrons trapped in vacancies, which are responsible for observed ferromagnetism in doped nanorods [20]. The charge imbalance between Cd^{2+} and Fe^{3+} ions leads to more number of defects in CdSe nanorods. The spins of Fe^{3+} ions interact with each other through donor impurity band formed by lattice defects in host CdSe nanorods. The increase of Fe-doping concentration increases bound magnetic polarons (F-centers), which in turn increases the saturation magnetization as shown in Figure 3.32. Finally, it is anticipated that the ferromagnetism is an intrinsic property of Fe-doped CdSe nanorods and is independent of the formation of secondary phases.

3.5 Structural, optical and magnetic properties of Co-doped CdSe nanorods

In this section, the series of $Cd_{1-x}Co_xSe$ (x = 0.00, 0.05 and 0.10) nanorods have been discussed. The details of synthesis procedure are described in chapter 2. The structural, optical and magnetic properties of pure and Co-doped nanorods have been measured. The obtained results and their discussion have been given below:

3.5.1 Structural and phase analyses

Figure 3.33 shows XRD patterns of pure and Co-doped CdSe nanorods. All the diffraction peaks correspond to wurtzite phase having hexagonal structure of CdSe (JCPDS card no. 77-2307).

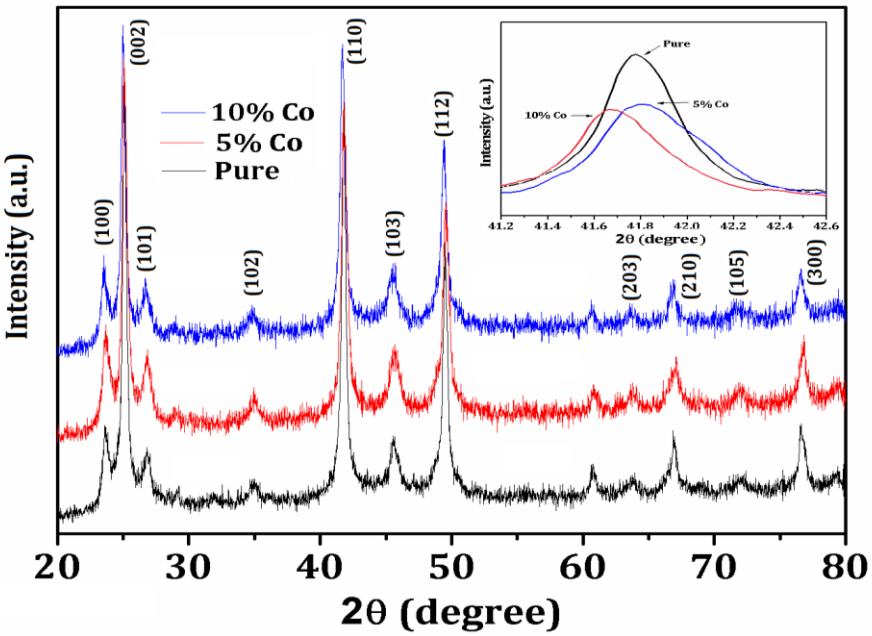

Figure 3.33 XRD pattern of pure and Co-doped CdSe nanorods. Inset shows the zoomed in view of 2θ around 41.7 degrees

No additional peaks related to cobalt metal clustering, oxides or secondary phases have been observed in XRD patterns, which illustrate the purity of synthesized nanorods. The decrease of

peak intensity has been observed with Co-doping which indicates degradation of crystalline quality of synthesized nanorods. The peaks have been found to shift towards higher angle in 5% Co-doped nanorods, but dramatic shift towards lower angle has been observed for 10% Co-doping (inset Figure 3.33).This non-uniform peak shifting leads to interesting variations in lattice parameters, unit cell volume and strain, as summarized in Table 3.5.1. The lattice parameters (a, c) have been calculated using [107]. The lattice strain has been calculated using W-H equation [152] and is summarized in Table 3.7. The decrease of lattice parameters (a, c) and unit cell volume (V*)* illustrates the lattice contraction for 5% Co-doping which can be attributed to the smaller ionic radii of Co^{2+} (0.72 Å) ions as compared to Cd^{2+} (0.97 Å) ions. However, reverse trend (for a, c and V) has been observed for 10% Co-doped CdSe nanorods. At higher doping concentration, interstitial incorporation of dopant takes place along with substitutional one, leading to increase of a, c, V and lattice expansion; this is well in agreement with the recent reports in literature [186, 187].

Table 3.7 The various parameters such as 2θ (degree), full width at half maxima (FWHM), lattice parameters, cell volume, strain of pure and Co-doped CdSe nanorods

Co-doping concentration	**$2\theta_{002}$ (degree)**	**FWHM**	**a=b (Å)**	**c = (Å)**	**d-spacing (Å)**	**Cell volume (Å)**	**Lattice strain**
Pure	25.08	0.34840	4.34386	7.09352	3.54676	115.91	0.000549
5%	25.11	0.45800	4.33996	7.08716	3.54358	115.60	0.005103
10%	24.99	0.38990	4.37124	7.13824	3.56912	118.11	0.003567

3.5.2 Morphological and elemental analysis

In order to investigate the morphology of synthesized samples, TEM analysis has been performed. Figure 3.34 (a) and (b) show the TEM images of 5% Co-doped CdSe samples, which shows the formation of nanorods with length in the range of 80-150 nm and diameter of 10-20 nm. Figure 3.34 (c) shows the HRTEM image with corresponding SAED pattern (inset) of a single 5% Co-doped CdSe nanorod. The clear lattice fringes have been observed in HRTEM image as shown by arrows, indicating the crystalline nature of synthesized nanorods without any segregated impurity phase.

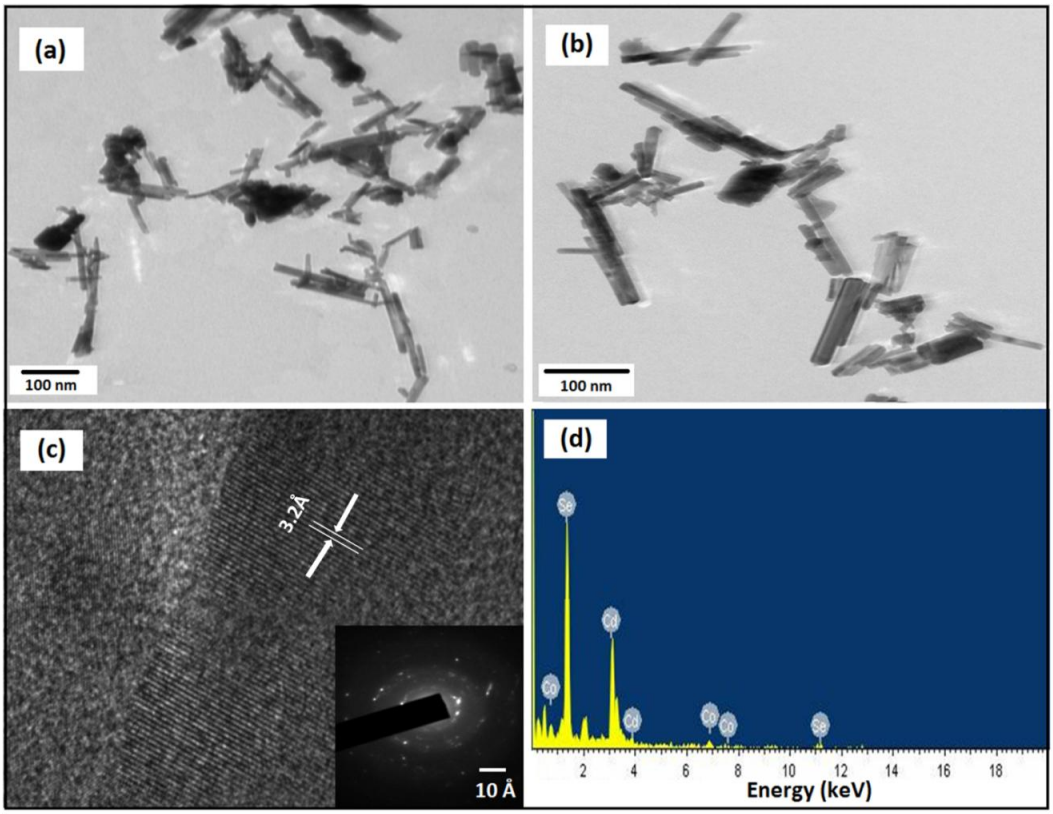

Figure 3.34 (a), (b) TEM images and (c) HRTEM image with SAED pattern (inset) and (d) EDS of 5% Co-doped CdSe nanorods

The *d*-spacing has been calculated to be 3.2 Å, well matched with d-spacing of (002) plane of wurtzite phase hexagonal structure of CdSe. The presence of Co ions in CdSe nanorods have been confirmed through EDS measurement. Figure 3.34 (d) shows the EDS pattern of 5% Co-doped CdSe nanorods. The quantitative analysis reveals that Cd and Se ions are in stoichiometric ratio (i.e. 1:1) and estimated quantity of Co is around 4.86%. No other impurity element has been detected in EDS pattern, confirming the purity of synthesized nanorods.

3.5.3 Optical analysis

The optical measurements of pure and Co-doped CdSe nanorods have been carried out by measuring the diffuse reflectance at room temperature. The change in band gap and gradual reduction of reflection has been observed with increasing the Co-doping, as shown in Figure 3.35.

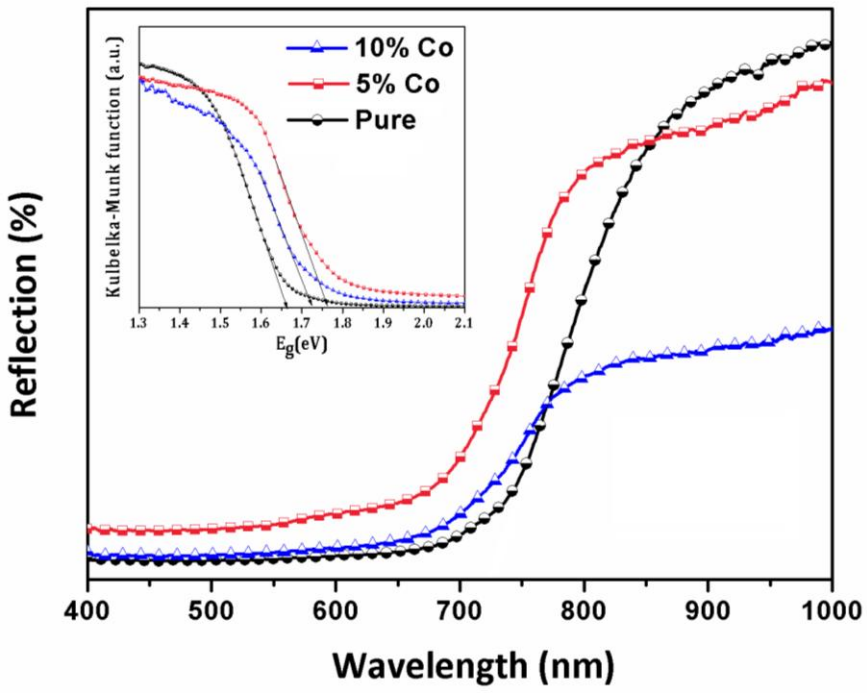

Figure 3.35 The diffuse reflectance spectra of pure and Co-doped CdSe nanorods

The band gap has been calculated using Kubelka-Munk function [168]. E_g of pure and doped nanorods has been calculated by plotting square of F(R) vs. energy (eV) as shown in inset of Figure 3.35. The values of E_g have been found to be 1.66, 1.76 and 1.71eV for pure, 5% and 10% Co-doped CdSe nanorods, respectively. In pure CdSe nanorods red-shift in E_g has been observed as compared to its bulk counterpart (1.72 eV). The observed red-shift can be explained by the presence of intraband-gap defects or strained anisotropic structure of pure CdSe nanorods [42, 155]. However, increase of E_g (1.76 eV) for 5% and sudden decrease of E_g (1.71 eV) for 10% Co-doping in CdSe nanorods has been observed. Similar trend in peak position, strain and lattice parameters have been observed in XRD analysis which indicates that observed variations in E_g can be related to structural changes arising due to Co-doping in CdSe nanorods. Recently, such changes in E_g have also been reported in literature [188, 189]. The structural changes can be considered as the sole reason for observed variation of E_g in the present study.

3.5.4 Raman spectroscopy analysis

Figure 3.36 shows the Raman spectra of pure and Co-doped CdSe nanorods recorded at room temperature. The phonon frequencies of 1LO and 2LO mode for pure CdSe nanorods have been found to be at 223 and 423 cm^{-1}, respectively, which are considerably blue-shifted as compared to its bulk counterpart frequencies found at 209 and 418 cm^{-1}. The surface reconstruction during growth of nanorods leads to lattice contraction which in turn generates lattice strain; this is responsible for observed blue-shift of phonon modes in pure nanorods [181].

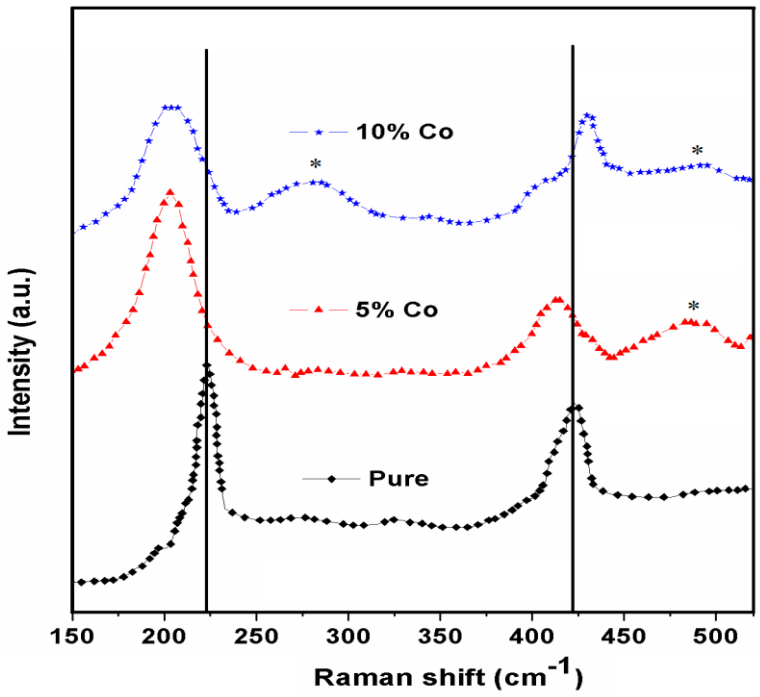

Figure 3.36 Raman spectra of pure and Co-doped CdSe nanorods

Decrease in Raman peak intensity for doped nanorods and red-shift of 1LO, 2LO phonon modes in Raman spectra for 5% and 1LO phonon mode for 10% Co-doped CdSe nanorods, indicate the considerable structural changes arising due to Co-doping in host nanorods. The Co-doping leads to lattice strain induced Raman peak-shift, caused by the different ionic radii of Co^{2+} ions and Cd^{2+} ions, which is in agreement with XRD analysis. The additional localized vibrational modes (marked by *) may possibly arise due to the structural changes resulting from Co-doping in host CdSe nanorods [62]. In order to estimate electron-phonon (el-ph) coupling strength, *S*-parameter has been calculated [173]. *S*-values have been found to be 1.87, 0.90 and 1.88 for pure, 5% and 10% Co-doped CdSe nanorods, respectively. No significant change in el-ph coupling strength has been observed for 10% Co-doping but considerable decrease of S-value has been observed for 5% Co-doping in CdSe nanorods.

3.5.5 ESR analysis

Figure 3.37 shows the ESR spectra of pure and Co-doped CdSe nanorods at room temperature. A broad signal with *g*-value ~ 2 has been observed for pure CdSe nanorods, which can be associated with the presence of defects in host nanorods [70, 138]. No ferromagnetic resonance signal has been observed in ESR spectra of doped nanorods, indicating the absence of exchange interactions between Co ions. More interestingly, the intensity of ESR signal becomes stronger with Co-doping concentration.

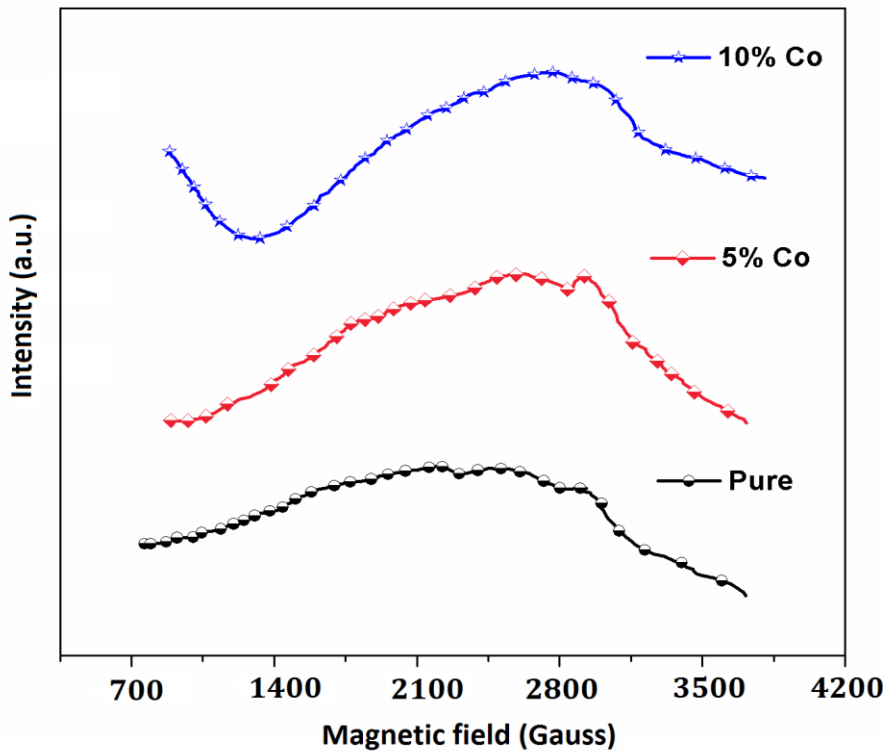

Figure 3.37 ESR spectra of pure and Co-doped CdSe nanorods

The increase of signal intensity with Co-doping corresponds to increase of defects states in host CdSe nanorods. In 10% Co-doped CdSe nanorods a resonance signal at 1300 G has been observed, which could be attributed to isolated Co^{2+} ions in host nanorods [190]. This is well in

agreement with the results obtained from XRD, diffuse reflectance and Raman spectroscopy analyses, which suggests the interstitial presence of Co ions at 10% doping concentration. ESR analysis reveals that structural changes due to Co-doping in CdSe nanorods give rise to ferromagnetic behavior, in the present study.

3.5.6 Magnetic analysis

The magnetic properties of pure and Co-doped CdSe nanorods have been investigated by VSM at room temperature. The distinct ferromagnetic hysteresis loops have been observed in pure and doped nanorods, as shown in Figure 3.38. A clear ferromagnetic hysteresis loop has been observed for pure CdSe nanorods having M_s ~ 0.045 emu/g, M_r ~ 0.0075 emu/g and H_c ~ 86 G. Bulk CdSe is a diamagnetic material with $\chi = -2.25 \times 10^{-7}$ emu $g^{-1}Oe^{-1}$) [148]. Different causes have been reported for observed ferromagnetism in CdSe nanomaterials such as nature of capping agent, defects and size [67-68, 149]. The observed ferromagnetic ordering in CdSe nanorods can be attributed to the presence of defects, well supported by the UV-visible analysis in present study. The bulk Co-doped CdSe based DMSs shows spin-glass behavior at low temperature (< 1K) and paramagnetism or antiferromagnetism at high temperature [11]. The origin of magnetism has been credited to distance between dopant ions, so paramagnetic behavior exists at lower doping concentration (< 0.01) while at higher doping concentration antiferromagnetic behavior exists. The reason for antiferromagnetism has been attributed to super-exchange type interactions between the nearest neighbors (Co ions) at higher doping concentration, in the bulk Co-doped CdSe. In the present study, increase in saturation magnetization for 5% Co-doped CdSe nanorods and an opposite behavior at higher doping concentration (i.e. 10% Co) has been observed, as shown in Figure 3.38. No peak related to Co

metal clustering or secondary phases such as CdO, Co_3Se_4, Co_7Se_8 and Co_9Se_8 have been observed in XRD patterns. In case secondary phases would have been present, a continuous increase in M_s would have occurred with increase of Co-doping, as the trend observed was not same so this possibility can be ruled out.

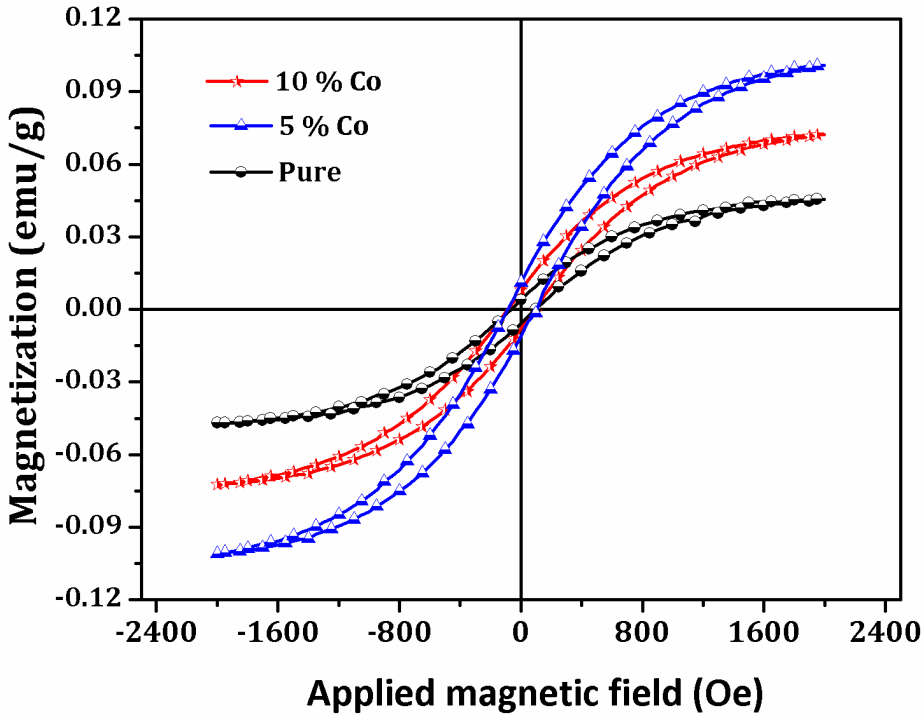

Figure 3.38 Room temperature hysteresis loops for the pure and Co-doped CdSe nanorods

Also, ESR analysis shows the absence of Co^{2+}-Co^{2+}exchange interactions, as no resonance signal has been observed in Co-doped CdSe nanorods. Further, in Raman analysis no significant increase of *S*-values with Co-doping has been observed, which indicates the lack of el-ph coupling strength in doped CdSe nanorods. So, the observed ferromagnetic ordering cannot be ascertained to the presence of Co metal clustering or secondary phases and exchange interactions between Co ions. The origin of ferromagnetic properties can be well-understood by considering

the structural changes arising due to Co-doping in the CdSe nanorods, as revealed by XRD and Raman analysis. As shown in XRD analysis, lattice contraction takes place for 5% Co-doping which indicates the substitutional doping of Co ions in host CdSe nanorods. The difference between the ionic radii of Co^{2+} and Cd^{2+} ions can result in more number of defects as compared to pure CdSe nanorods. This leads to enhanced ferromagnetism in 5% Co-doped CdSe nanorods. This speculation has further been supported by ESR analysis as defects related broad resonance peak has been observed in 5% Co-doped nanorods. However, decrease of ferromagnetism at 10% Co-doping can be explained by lattice expansion of CdSe nanorods (inset Figure 3.33) and structural disorder, as indicated by the peak broadening and appearance of new Raman peaks (Figure 3.36). The interstitial incorporation of Co ions along with substitutional one leads to lattice expansion of the CdSe nanorods as reported in literature for other systems [58, 64]. The interstitial presence of Co ions leads to lattice expansion, which destroys the ferromagnetism in host CdSe nanorods as ferromagnetic interactions are strongly dependent on the distance between Co ions [191, 192, 189]. The present study shows the intrinsic ferromagnetism in Co-doped CdSe nanorods. However, further study is required in order to confirm about the oxidation state of Co ions, their locations and role of defects.

3.6 Structural, optical and magnetic properties of Ni-doped CdSe nanorods

In this section, the series of $Cd_{1-x}Ni_xSe$ (x = 0.00, 0.05, 0.10 and 0.15) nanorods have been discussed. The details of synthesis procedure are described in chapter 2. The structural, optical and magnetic properties of pure and Ni-doped nanorods have been measured. The obtained results and their discussion have been given below:

3.6.1 Structural and phase analyses

Figure 3.39 shows XRD patterns of undoped and Ni-doped CdSe nanorods. The well-resolved peaks in XRD pattern indicate the crystalline nature of nanorods.

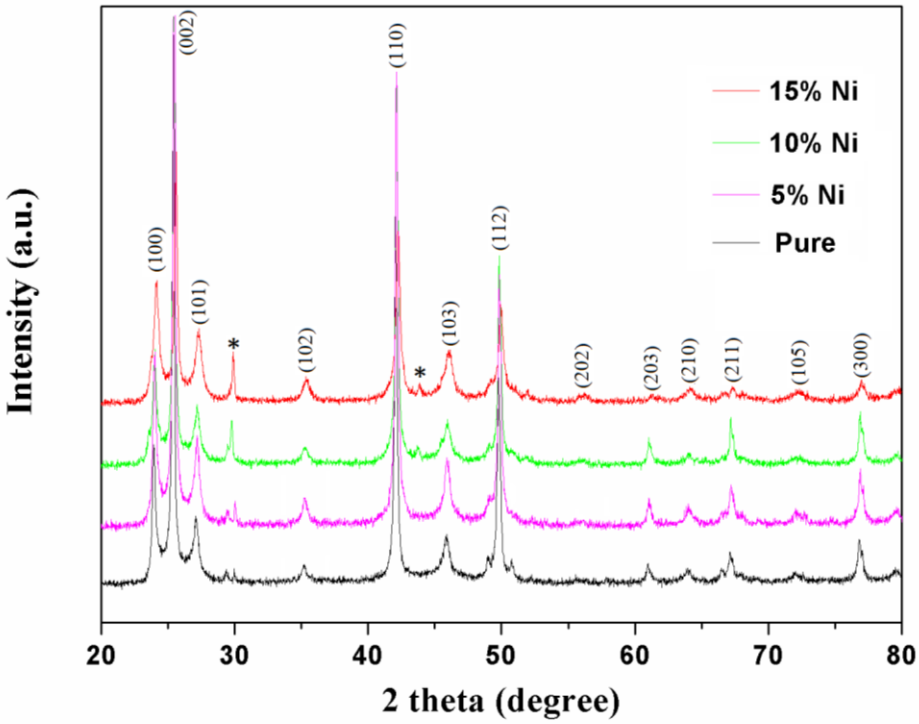

Figure 3.39 XRD spectra of pure and Ni-doped CdSe nanorods. The extra peaks are marked by asterisk (*)

The diffraction peaks are in agreement with hexagonal structure of CdSe (JCPDS card no. 77-2307) with lattice parameters a = 4.299 Å and c = 7.010 Å. Some additional peaks, as observed in Figure 3.39, marked by (*), are related to Se (JCPDS card no. 38-0768). With increase in Ni-doping concentration, peaks related to Se have been found to increase. The lattice parameters (a, c) has been calculated using equation [107]. The value of the lattice parameters have been found to decrease with increase of Ni-doping; this can be attributed to the smaller ionic radii of Ni^{2+} (0.69 Å) as compared to Cd^{2+} (0.97 Å). XRD peaks have been found to shift towards higher angle of diffraction, indicating the substitution of Ni^{2+} ions in host CdSe nanorods [193-195]. The 'η' in synthesized nanorods, has been calculated (Figure 3.40) from Williamson-Hall relation equation [152]. The effect of Ni-doping on effective strain has been tabulated in Table 3.8.

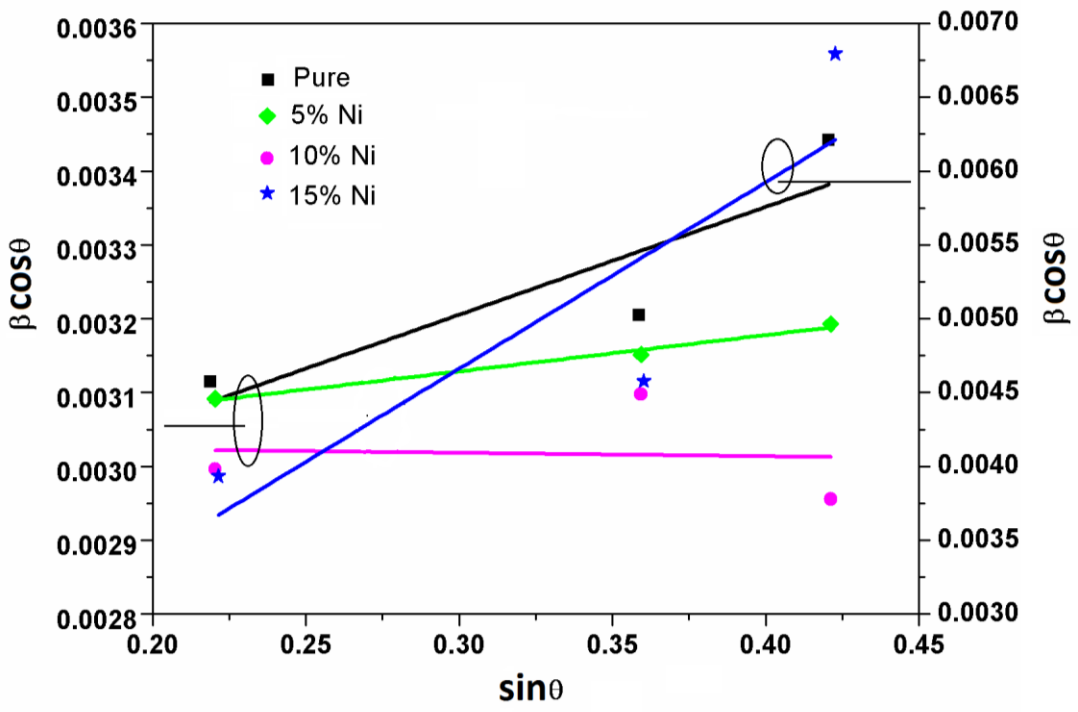

Figure 3.40 W-H plot for pure and Ni-doped CdSe nanorods

Table 3.8 $2\theta_{002}{}^{o}$, β, d-spacing, a, b, c and η of synthesized nanorods

Ni content in CdSe nanorods (at wt %)	**$2\theta_{002}$ (degree)**	**β**	**d-spacing (Å)**	**a=b (Å)**	**c (Å)**	**η**
0 %	25.399	0.18300	3.504	4.29	7.01	0.00146
5% Ni	25.465	0.18170	3.495	4.28	6.99	0.00049
10% Ni	25.472	0.17610	3.494	4.27	6.98	0.00004
15% Ni	25.590	0.23120	3.478	4.25	6.95	0.01262

The decrease of lattice strain, upto 10% Ni-doping, indicates the undoped CdSe nanorods being under considerable lattice strain. However, increase of strain at 15% Ni-doping could be attributed to interstitial incorporation of Ni at higher doping concentration [192]. This further establishes that solubility limit of Ni in CdSe nanorods is ≤ 10%, and beyond this concentration, interstitial incorporation of dopant takes place.

3.6.2 Morphological and elemental analysis

Figure 3.41 (a) and 3.41 (b) show the TEM and HRTEM images of undoped CdSe confirming the formation of nanorods having lengths in the range of 150-200 nm with diameters around 10-15 nm. The clear lattice fringes have been observed in HRTEM analysis and the *d*-spacing has been found to be 3.4Å. It also reveals that the nanorods growth direction is along (002) plane confirming that the nanorods are highly *c*-axis oriented. Figures 3.41 (c, d) show EDS spectra of 5% and 10% Ni-doped nanorods, which confirm the presence of Ni along with Cd and Se

elements. No additional peaks, related to other parasite impurity, have been observed in EDS spectra, confirming their purity.

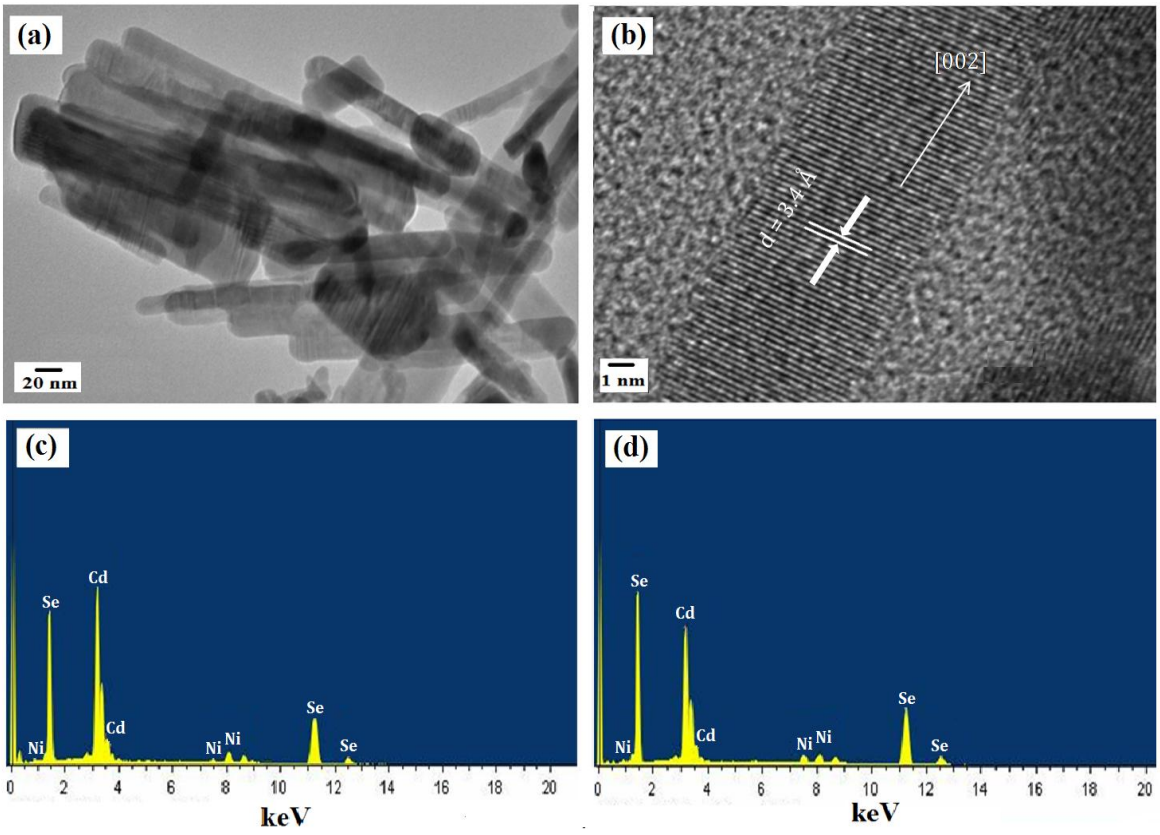

Figure 3.41 (a) TEM (b) HR-TEM micrograph of undoped CdSe nanorods (c), (d) EDS spectra of 5% and 10% Ni-doped CdSe nanorods

3.6.3 Optical analyses

3.6.3.1 UV-vis. analysis

Figure 3.42 shows UV–visible absorption spectra of undoped and Ni-doped CdSe nanorods. The band gap values have been estimated using the Kubelka-Munk function (F(R)) [168] and plotted as a function of photon energy (hν); on extrapolating the line for $(F(R)\ h\nu)^2 = 0$ gives the band

gap energy, as shown in inset of Figure 3.42. The band gap values have been found to be 1.62, 1.57, 1.54 and 1.52 eV, for undoped, 5%, 10% and 15% Ni-doping in CdSe nanorods, respectively. The absorption edge has been observed at 765 nm (E_g ~ 1.62 eV) for undoped CdSe nanorods indicating red-shift as compared to its bulk counterpart (720 nm, 1.72 eV). The observed red-shift can be attributed to intra-band gap defects present or strained anisotropic structure of undoped nanorods [155, 99].

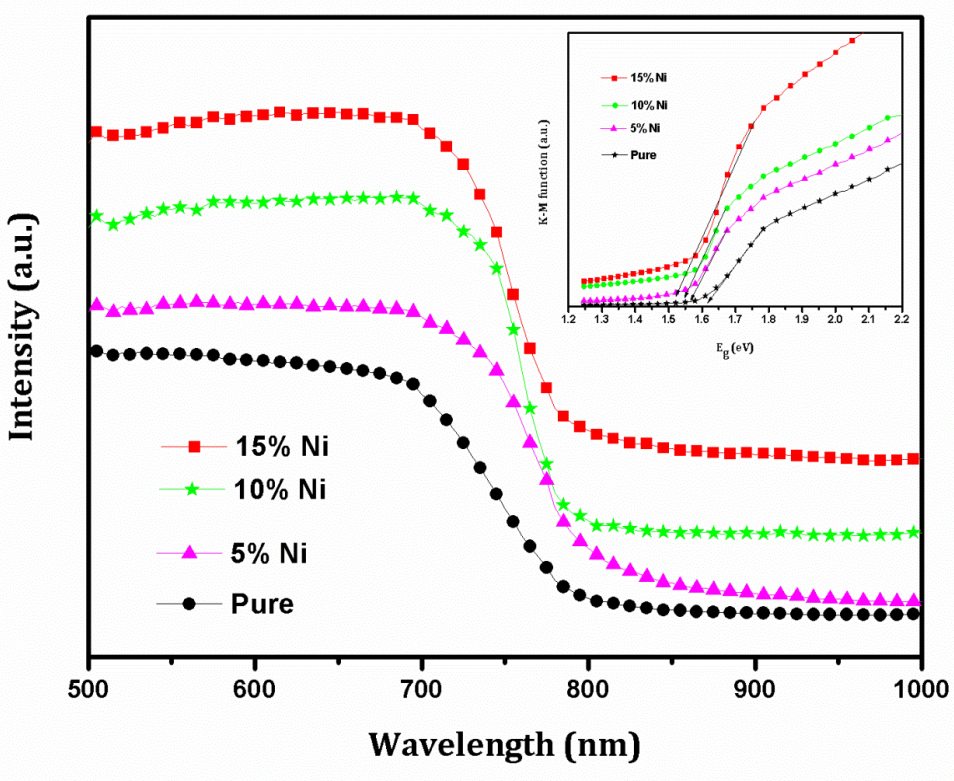

Figure 3.42 UV–visible absorption spectra of undoped CdSe and Ni (5%, 10% and 15%) doped CdSe nanorods and inset shows Kubelka-Munk plots for bandgap estimation

The shifting of absorption edge towards higher wavelength (i.e. decrease of E_g) has been observed with Ni-doping concentration. This may possibly be due to sp-d exchange interactions between localized *'d'* electrons of dopant ions, which substitute Cd^{2+} ions and band electrons of

host CdSe nanorods [196-198]; it confirms substitution of Ni^{2+} ions into Cd^{2+} sites of CdSe nanorods.

3.6.3.2 PL analysis

In order to investigate the various electronic transitions occurring between valence and conduction band, room temperature PL spectra of undoped and Ni-doped CdSe nanorods have been recorded by exciting the synthesized nanorods at 550 nm, as shown in Figure 3.43. The broad peak observed at 750 nm corresponds to near band edge or defects emission in the synthesized nanorods. However, emission intensity of observed peaks reduces with doping of Ni in CdSe nanorods.

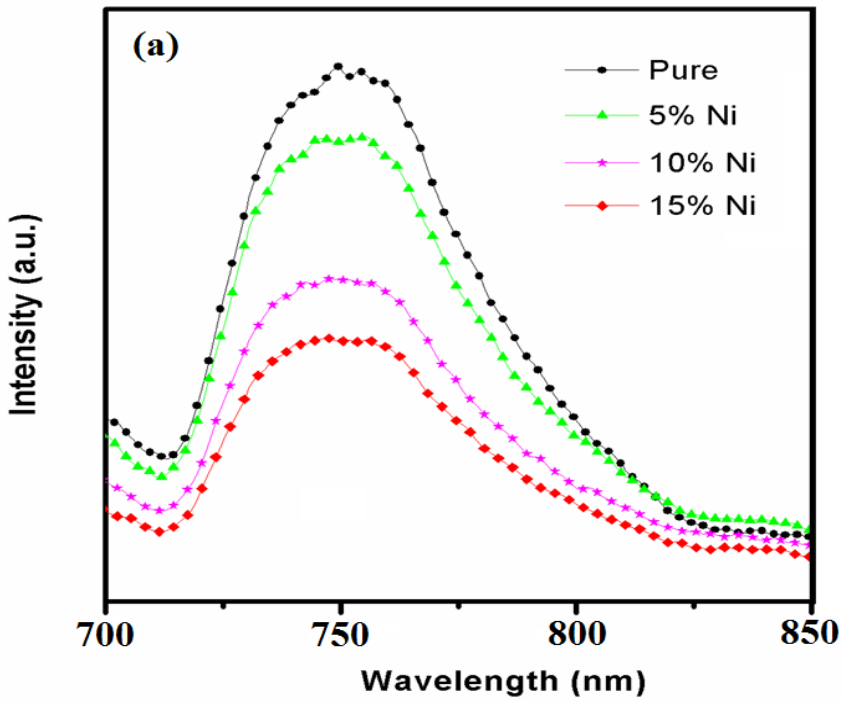

Figure 3.43 Room temperature PL emission spectra of pure and Ni-doped CdSe nanorods

The photo-excited electrons are preferentially transferred to defects or trap states resulting in non-radiative emission, and, therefore, showing that the emission intensity decreases with increase in Ni-doping concentration [171].

3.6.4 Raman analysis

Figure 3.44 shows the room temperature Raman spectra of undoped and Ni-doped CdSe nanorods. Phonon frequencies of 1LO and its overtones 2LO, 3LO modes of bulk CdSe have been reported in literature at 209 and 418, 627 cm^{-1}, respectively [142]. The blue-shift in frequency of 1LO and 2LO phonon mode has been observed in undoped CdSe nanorods. The most probable reason for the observed blue-shift is the presence of lattice strain in synthesized nanorods [141]. Subsequent to 1LO phonon mode in undoped and doped nanorods, additional Raman peaks marked by arrows have been observed. Their origin can be related to the structural disorder caused by dopant ions leading to activation of additional vibrational modes [62, 181]. In lower frequency side of 1LO phonon modes, noticeable peaks were observed at 214, 198 and 177 cm^{-1} due to surface optical (SO) and transversal optical (TO) phonon modes of CdSe [199]. However, Raman peaks marked by (*) cannot be readily assigned to SO, LO and TO vibrational phonon modes of CdSe lattice. These are localized vibrational modes (LVM), which have arisen due to Ni-doping in CdSe nanorods [62].

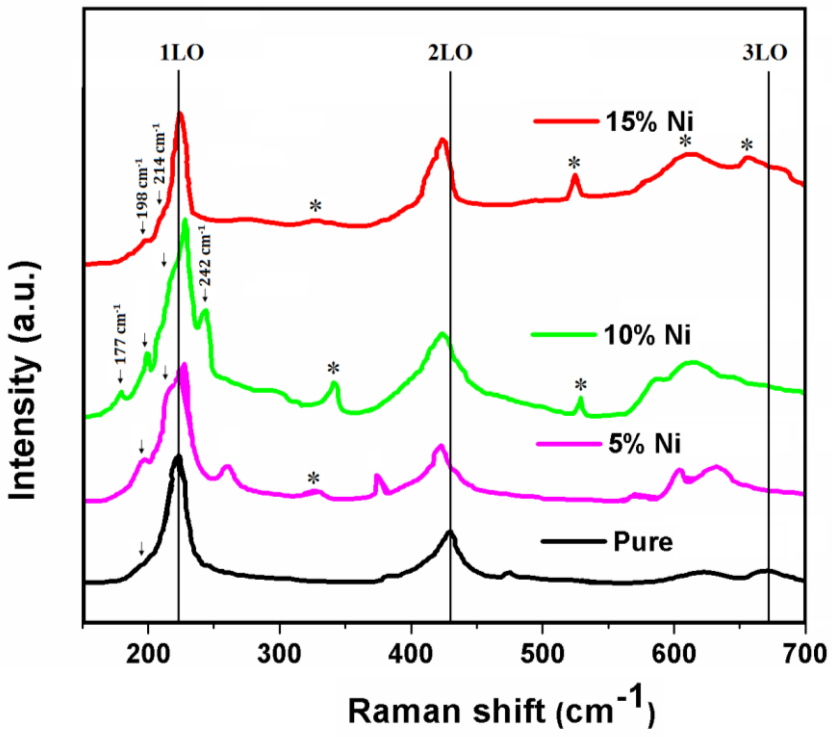

Figure 3.44 Raman spectra of pure and Ni-doped CdSe nanorods with argon source excitation

The red-shift in 2LO and 3LO phonon modes can be attributed to the decrease of strain well in agreement with XRD analysis. Further, higher Ni concentration upto 15% led to disappearance of some LVM modes which might have resulted from structural changes due to interstitial incorporation of Ni^{2+} in CdSe nanorods. Ni-doping increases electron-phonon coupling strength; this has been confirmed by *S*-parameter [173]. *S*-values have been found to be 1.10, 1.24, 1.33 and 1.79 for undoped, 5%, 10% and 15% Ni-doping concentration, respectively. Increase of *S*-factor shows enhanced electron-phonon coupling due to the changes in sp-d exchange interactions with Ni-doping in CdSe nanorods.

3.6.5 ESR analysis

Figure 3.45 shows ESR spectra of pure and Ni-doped CdSe nanorods, at room temperature. A weak broad resonance signal with *g*-value ~ 2.17 has been observed for pure CdSe nanorods. Different reasons are ascribed for the origin of such signal in literature such as, paramagnetic capping agent, impurities or defects [70, 138].

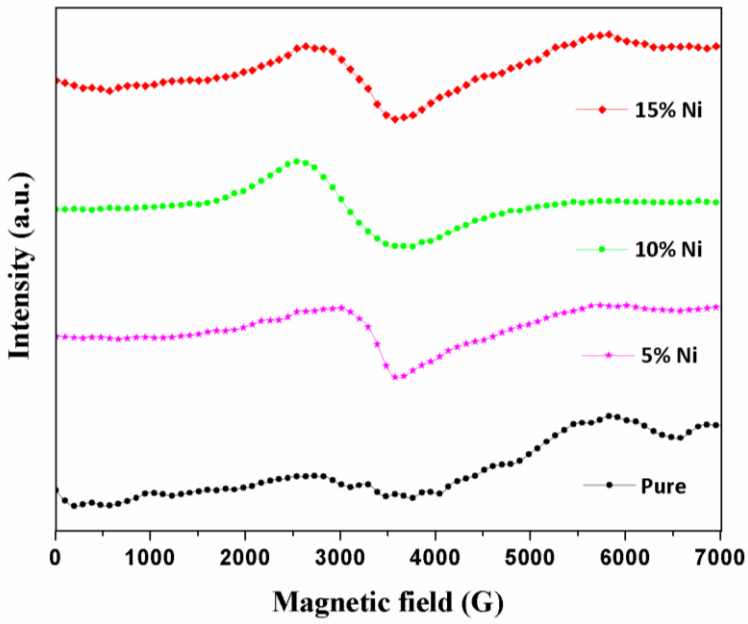

Figure 3.45 ESR spectra of $Cd_{1-x}Ni_xSe$ (x = 0.0, 0.05, 0.10, 0.15) nanorods

In present work, no capping agent is used and proper care has been taken during experimental work. So, the observed ESR signal can be ascribed to presence of defects in pure CdSe nanorods. ESR spectra of Ni-doped CdSe nanorods exhibit broad line width which could be attributed to ferromagnetic resonance due to long range exchange interactions.

Table 3.9 g-value, ΔH, peak to peak intensity and N_s of pure and Ni-doped CdSe nanoparticles

Samples	g-value	Line width, ΔH (G)	Peak to peak intensity	No. of spins, N_s
Pure	2.17	604	578	0.60×10^{8}
5% Co	2.25	900	1113	2.56×10^{8}
10% Co	2.32	1063	2083	6.70×10^{8}
15% Co	2.38	1000	8441	2.40×10^{8}

The decrease of resonance signal towards lower magnetic field has been observed with increase of Ni-doping concentration (Figure 3.45). As a consequence, *g*-value increases from 2.27 to 2.39 (Table 3.9). This could be attributed to increase of ferromagnetic interactions as Ni^{2+}- Ni^{2+} ions comes closer to each other with increase of doping concentration [200]. It has been observed (from Table 3.9) that number of spins participating in ferromagnetic resonance increases with increase of Ni-doping concentration upto 10% of Ni-doping concentration. Afterwards, decrease in N_s and peak to peak intensity has been observed. The interstitial incorporation of Ni^{2+} ions could be possible reason for such observations, at higher doping concentration [201]. This is in agreement with M_s which has been found to decrease at this concentration.

3.6.6 Magnetic analysis

Figure 3.46 shows room temperature M-H hysteresis loops of synthesized nanorods revealing their ferromagnetic nature. Increase in doping concentration leads to increase of saturation magnetization upto 10% Ni-doping concentration, but afterwards, it has been found to decrease (Table 3.10). The bulk CdSe shows diamagnetism with susceptibility, $\chi = -2.25 \times 10^{-7}$ emu g^{-1} Oe^{-1} [148]. However, undoped CdSe nanorods exhibit ferromagnetism at room temperature.

Origin of the observed ferromagnetism in undoped CdSe nanorods can be attributed to the presence of surface defects or charge transfer due to capping agent [67-69]. In the present study, no capping agent has been used, and, therefore, the observed ferromagnetism can be attributed to the presence of defects. The red-shift in absorption spectrum and shifting of phonon modes in Raman spectra support defect related ferromagnetism in the undoped CdSe nanorods.

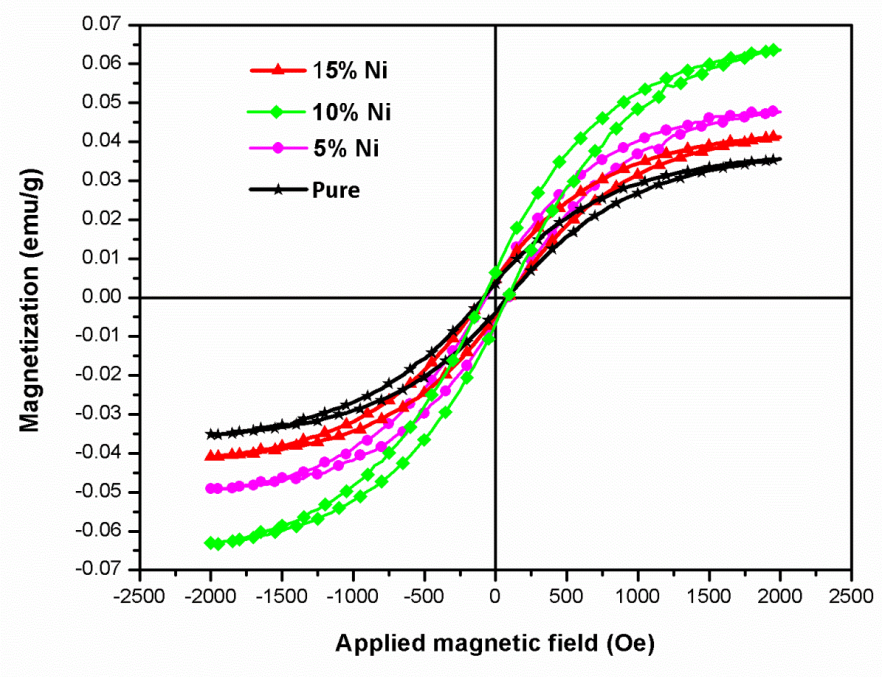

Figure 3.46 M-H hysteresis curves of undoped and Ni-doped CdSe nanorods after subtracting diamagnetic contribution from sample holder (background correction).

Table 3.10 The observed M_s, M_r and H_c of undoped and Ni-doped CdSe nanorods

Ni content in CdSe nanorods (at wt %)	$\boldsymbol{M_s}$ **(emu/g) × 10^{-2}**	$\boldsymbol{H_c}$ **(Oe)**	$\boldsymbol{M_r}$ **(emu/g) × 10^{-3}**
0 %	3.522	79.83	3.667
5 %	4.787	82.92	5.112
10 %	6.334	87.18	6.569
15 %	4.176	85.40	4.696

The ferromagnetism in doped nanorods could arise from number of possibilities such as Ni metal, its extra phases or intrinsic ferromagnetism in doped nanorods. Metallic Ni is a ferromagnetic element in free state, but it is unable to retain its metallic nature during the synthesis, leading to formation of secondary phases of Ni such as NiSe, NiO, NiO_2 and Ni_2O_3. NiSe is diamagnetic in bulk, whereas bulk NiO exhibits antiferromagnetism (Neel temperature ~ 520 K) or superparamagnetism at nanocrystalline range [175]. No peaks, related to secondary phases or its other compounds have been observed in XRD and Raman analysis.

The observed ferromagnetism with Ni-doping can be explained by defects or doping in CdSe nanorods. The doping of Ni enhances defects as evident from PL analysis leading to entrapment of charge carriers in defects. First, it leads to increased ferromagnetism in Ni-doped CdSe nanorods. Second, the enhanced coupling between Ni^{2+}-Ni^{2+} ions via trapped charge carriers also contributes to increased ferromagnetism. Both of these factors play a very crucial role in the observed ferromagnetism in doped CdSe nanorods. There is a competition between indirect and direct ferromagnetic coupling in doped nanorods. The decrease of ferromagnetism at 15% Ni-

doping can be attributed to direct coupling (super-exchange interactions) between Ni^{2+} ions [192, 197]. At higher doping concentration, Ni ions come closer to each other and interact directly. The direct exchange interactions (or super-exchange interactions) are antiferromagnetic in nature, which lead to decrease in magnetization. This establishes that the ferromagnetism in the DMS nanorods is intrinsic in nature. This is useful for future spintronic device applications.

Chapter 4

Conclusions

Chapter 4

Conclusions

This chapter concludes the present thesis work. The summary of key results has been given, along with an insight into the future scope of the present research work.

4.1 Conclusions

In present thesis, transition metals (Fe, Ni and Co) doped CdSe nanostructures have been studied in detail. The work has been divided into two parts:

(a) Fe, Co and Ni-doped CdSe nanoparticles

(b) Fe, Co, and Ni-doped CdSe nanorods

The main outcome of the research work has been given below:

4.1.1 Fe-doped CdSe nanoparticles

- Fe-doped CdSe nanoparticles have been successfully synthesized by hydrothermal method.
- The solubility limit of Fe in CdSe nanoparticles from XRD analysis has been found to be less than 6 % and with increase in doping concentration at and above it, secondary phase of $FeSe_2$ starts appearing.
- The presence of Cd, Se, and Fe has been confirmed by EDS.

- TEM study shows the spherical nature of nanoparticles having average size of 14 nm for pure and 10 nm for 6% Fe-doped CdSe nanoparticles.
- Blue-shift in UV-vis. spectra (1.90-1.97eV) and variation in PL emission intensity further indicates the incorporation of Fe in CdSe.
- The phonon confinement has been observed in Raman spectra with increase of Fe-doping concentration. The spectra also show presence of extra phase in agreement with XRD.
- ESR analysis indicates the presence of Fe ions in mixed oxidation states via Fe^{2+} / Fe^{3+}. It also shows the ferromagnetic resonance interactions in pure and Fe-doped CdSe nanoparticles.
- M–H hysteresis loop indicates that pure as well as Fe-doped CdSe nanoparticles exhibited room-temperature ferromagnetism and saturation magnetization was found to increase with Fe doping concentration. The value of saturation magnetization was found to be 0.002, 0.520 and 1.007 emu/g for pure, 6%, and 10% Fe-doped CdSe nanoparticles, respectively. The observed ferromagnetism in pure CdSe nanoparticles may be attributed to capping agent, defects or particle size. The increase in saturation magnetization due to Fe-doping could be attributed to exchange interaction between Fe^{2+}-Fe^{2+} ions or bound magnetic polarons (F-centers) in doped nanoparticles. Also, large surface area of nanoparticles can leads to alignment of more number of magnetic dipoles in same direction, resulting in increase of saturation magnetization.

4.1.2 Co-doped CdSe nanoparticles

- Our investigations on hydrothermally synthesized pure and Co-doped CdSe nanoparticles reveal that the dopant concentration causes distinctive changes in the structural, optical, morphological, and magnetic properties of CdSe nanoparticles.
- Pure CdSe nanoparticles possess polycrystalline cubic structure having zinc blende phase; whereas the additional peaks of $CoSe_2$ have been observed due to Co doping. The average crystallite size from XRD analysis have been found to be 20.7, 3.8, 3.6 and 3.1 nm for pure, 5, 10 and 15 % Co doped CdSe, respectively.
- The blue-shift (1.65-1.83eV) and luminescence quenching with doping concentration indicates the presence of Co ions in CdSe nanoparticles.
- From TEM analysis, average particle size comes out to be 41.2, 9.5, 8.9 and 7.5 nm for pure, 5, 10 and 15 % Co doped CdSe, respectively. It has been observed that the pure CdSe nanoparticles formed were of irregular shapes, whereas Co doping results in spherical morphology with decreased particle size.
- Raman spectra indicate substitution of Co in CdSe nanoparticles along with appearance of secondary phase. The observed Raman-shift can be related to phonon confinement and lattice strain in doped nanoparticles.
- ESR show strong exchange interactions between Co^{2+}- Co^{2+} ions which are increasing with doping concentration.
- M-H analysis reveals the transformation of diamagnetic pure CdSe nanoparticles to ferromagnetic Co-doped nanoparticles at lower doping concentrations. The magnetic analysis shows the ferromagnetic behaviour up to 10% of Co- doping concentration. The increase of Co content beyond 10% doping concentration leads to antiferromagnetic

interactions between the Co ions, which suppress the ferromagnetism. The transition from ferromagnetism to antiferromagnetism is credited to the distance-dependent magnetic interaction between the two Co ions.

4.1.3 Ni-doped CdSe nanoparticles

- Pure and Ni-doped CdSe nanoparticles have been synthesized by hydrothermal method.
- XRD pattern reveal the formation of hexagonal structure and wurtzite phase of synthesized nanoparticles.
- TEM images show the spherical morphology of nanoparticles. The average particle size has been comes out to be 24.3 nm for pure and 17.6 nm for 10% Ni-doped nanoparticles.
- The diffuse reflectance study shows the blue-shift in band gap with increase of Ni-doping concentration. The band gap values have been calculated to be 1.77, 1.80, 1.82, 1.85 eV for pure, 2%, 5% and 10% Ni-doped CdSe nanoparticles.
- The intrinsic defects or deep level vacancies (V_{Cd} –V_{Se}) have been observed in CdSe nanoparticles, which are characteristics of wurtzite structure. These can be explained via two different types of V_{Cd} – V_{Se} associates in wurtzite structure. One is oriented along the hexagonal *c*-axis and other is oriented along the basal Cd–Se bond direction.
- Raman spectra show the enhanced electron-phonon coupling strength with increase of Ni-doping in CdSe nanoparticles. Also, no indication of any secondary phases related to Ni or Cd have been observed in Raman spectra.
- The g-value >2 (from ESR spectra) indicate ferromagnetism in pure and Ni-doped CdSe nanoparticles.
- The ferromagnetic M-H curves have been obtained for pure and doped nanoparticles. PL study shows the presence of defects in pure and doped nanoparticles. The trapped

charge carriers in defects lead to ferromagnetic ordering in pure CdSe nanoparticles. Also, trapped carriers can acts as a medium for indirect ferromagnetic resonance between Ni^{2+} ions. This leads to increase of ferromagnetism in Ni-doped CdSe nanoparticles, which arises from the long range ferromagnetic resonance between Ni^{2+}-Ni^{2+} ions. The ferromagnetic ordering has been further supported by ESR analysis. We conclude that the intrinsic defects and indirect ferromagnetic coupling between Ni^{2+}-Ni^{2+} ions both are responsible for observed ferromagnetism in the present study. Therefore, the observed RTFM in Ni-doped CdSe nanoparticles is intrinsic in nature; this can be useful for future spintronics device applications.

Table 4.1 The comparison of various properties observed for common doping concentration of Fe, Co and Ni-doped CdSe nanoparticles (** % doping in case of Fe : CdSe is 6% and not 5%)*

→ **Dopant** **Properties** ↓	**Fe-doped CdSe nanoparticles**			**Co-doped CdSe nanoparticles**			**Ni-doped CdSe nanoparticles**		
	0%	**5%***	**10%**	**0%**	**5%**	**10%**	**0%**	**5%**	**10%**
Structure and Phase	Hexagonal structure and wurtzite phase			Cubic structure and zinc blende phase			Hexagonal structure and wurtzite phase		
Average particle size (nm)	14	10	….	41	9.5	9	24	….	17
E_g (eV)	1.90	1.95	1.97	1.65	1.78	1.80	1.77	1.82	1.85
Magnetic behavior	Ferro-magnetic	Ferro-magnetic	Ferro-magnetic	Diamag-netic	Ferro-magnetic	Antiferro-magnetic	Ferro-magnetic	Ferro-magnetic	Ferro-magnetic
M_s (emu/g)	0.002	0.520	1.007	….	0.0001	….	0.0005	0.0018	0.0025

4.1.4 Fe-doped CdSe nanorods

- The present work deals with the role played by structural defects and doping concentration on the observed ferromagnetic behaviour in pure and Fe-doped CdSe nanorods.
- The successful syntheses of pure and Fe-doped CdSe nanorods have been carried out by solvothermal route.
- XRD and Raman analyses reveal the formation of wurtzite phase hexagonal structure of the pure and Fe-doped CdSe nanorods, without any additional parasitic secondary phases.
- SAED, TEM and HRTEM results show the single crystalline nature of the synthesized nanorods, possessing diameter and length around 8–15 nm and 100-140 nm, respectively.
- ESR and Raman spectra reveal the enhanced ferromagnetic exchange interaction with doping in the CdSe nanorods. Further, the ESR spectra indicate that the doped Fe ions exist in +3 oxidation state.
- The charge imbalance between Fe^{3+} and Cd^{2+} leads to increase of lattice defects in the host nanorods in order to maintain the charge neutrality.
- The observed red-shift in band gap of pure CdSe nanorods (1.57 eV) as compared with their bulk counterpart (1.72 eV), confirms the presence of defects.
- The observed increase in M_s values, from 0.026, 0.143, 0.263 and 0.415 emu/g for 0, 2, 5, and 10% Fe-doping concentration arises due to exchange interaction between Fe ions through defect states present in the host nanorods. The origin of magnetism in pure CdSe nanorods can be related to defects and increase of saturation magnetization with Fe-

doping concentration can be explained by the bound magnetic polaron (F-center exchange mechanism) at defect sites in the host CdSe nanorods.

4.1.5 Co-doped CdSe nanorods

- The present study deals with the investigation on the structural and magnetic properties of pure and Co-doped CdSe nanorods synthesized.
- The syntheses of nanorods with length of 80-150 nm and diameter of 10-20 nm have been carried out using solvothermal technique.
- XRD, HRTEM and Raman spectroscopy analysis confirm the absence of any secondary phases in pure and doped nanorods.
- Raman analysis indicates that there is no considerable enhancement of el-ph coupling strength with Co-doping in CdSe nanorods.
- ESR analysis further confirms the absence of exchange interaction between Co^{2+} ions.
- In the light of above observations, origin of ferromagnetism has been related to the structural changes arising due to Co-doping in CdSe nanorods, which is well in agreement with the lattice parameters from XRD patterns and the strain related peak shifting in Raman spectra. In the present study, increase of ferromagnetism has been related to the lattice contraction upto 5% Co-doping while the lattice expansion leads to destruction of ferromagnetism at 10% Co-doping, which is due to the interstitial incorporation of Co ions in host CdSe nanorods. The study reveals that there is a strong correlation between structural and magnetic properties of Co-doped CdSe nanorods.

4.1.6 Ni-doped CdSe nanorods

- $Cd_{1-x}Ni_xSe$ (x = 0.00, 0.05, 0.10, 0.15) nanorods have been synthesized by solvothermal route. The Ni-doping has considerable influence on the structural, optical, and magnetic properties of the synthesized CdSe nanorods.
- XRD confirms that synthesized nanorods possess wurtzite phase with hexagonal structure.
- The formation of CdSe nanorods with length in the range of 150-200 nm and diameter around 10-15 nm has been estimated from TEM images.
- The defect related emission in PL, red-shift in UV-visible and shifting of LO in Raman spectra indicate the presence of defects in pure and doped CdSe nanorods.
- ESR study shows the decrease of resonance signal towards lower magnetic field with increase of Ni-doping concentration. As a consequence, *g*-value increases from 2.27 to 2.39. This could be attributed to increase of ferromagnetic interactions as Ni^{2+}- Ni^{2+} ions comes closer to each other with increase of Ni-doping concentration.
- Magnetic study confirmed that the pure as well as Ni-doped CdSe nanorods exhibit ferromagnetism at room temperature. The observed ferromagnetism with Ni-doping can be explained by defects or doping in CdSe nanorods. Both of these factors play a very crucial role in the observed ferromagnetism in doped CdSe nanorods. There is a competition between indirect and direct ferromagnetic coupling in doped nanorods. The decrease of ferromagnetism at 15% Ni-doping can be attributed to direct coupling (super-exchange interactions) between Ni^{2+} ions. At higher doping concentration, Ni ions come closer to each other and interact directly. The direct exchange interactions (or super-

exchange interactions) are antiferromagnetic in nature, which lead to decrease in magnetization. This establishes that the ferromagnetism in the DMS nanorods is intrinsic in nature. This is useful for future spintronic device applications.

Table 4.2 The comparison of various properties observed for common doping concentration of Fe, Co and Ni-doped CdSe nanorods

Dopant → / **Properties ↓**	**Fe-doped CdSe nanorods**			**Co-doped CdSe nanorods**			**Ni-doped CdSe nanorods**		
	0%	**5%**	**10%**	**0%**	**5%**	**10%**	**0%**	**5%**	**10%**
Structure and Phase	Hexagonal structure and wurtzite phase			Hexagonal structure and wurtzite phase			Hexagonal structure and wurtzite phase		
Average particle size (nm)	Length 100-140 nm and diameter 8-15 nm			Length 80-150 nm and diameter 10-20 nm			Length 100-200 nm and diameter 10-30 nm		
E_g *(eV)*	1.57	1.60	1.61	1.66	1.76	1.71	1.65	1.63	1.62
Magnetic behavior	Ferro-magnetic	Ferro-magnetic	Ferro-magnetic	Ferro-magnetic	Ferro-magnetic	Ferro-magnetic	Ferro-magnetic	Ferro-magnetic	Ferro-magnetic
M_s *(emu/g)*	0.026	0.263	0.415	0.045	0.100	0.072	0.048	0.041	0.035

4.2 Future scope of research

- The exact mechanism behind the observed magnetism needs to be further explored in transition metal doped CdSe nanoparticles and the work can be further extended to other nanostructures such as quantum dots or nanowires as DMS materials.

- The other sophisticated instruments could be used for characterization in order to completely understand the origin of magnetism such as magnetic circular dichroism (MCD), x-ray absorption spectroscopy (XAS), x- ray photon spectroscopy (XPS).
- The work can be extended to the doping of other transition metals such as (Cu, Mn) or rare earth elements (Gd, Tb, Eu).

References

[1] W. F. Brinkman, D. E. Haggan, W. W. Troutman, IEEE J. Solid-St. Circ. **32**, (1997) 1858-1865.

[2] T. Ito, S. Okazaki, Nature **406**, (2000) 1027-1031.

[3] R. R. Schaller, IEEE, Spectrum **34,** (1997) 52-59.

[4] S. D. Sarma, Am. Sci. **89**, (2001) 516-523.

[5] S. A. Wolf, D. D. Awschalom, R. A. Buhrman, J. M. Daughton, S. Von Molnar, M. L. Roukes, A. Yu Chtchelkanova, D. M. Treger. Science **294**, (2001) 1488-1495.

[6] I. Žutić, J. Fabian, S. D. Sarma, Rev. Mod. Phys. **76**, (2004) 323.

[7] D. D. Awschalom, M. E. Flatté, Nat. Phys. **3**, (2007) 153-159.

[8] G. Binash, P. Grunberg, F. Saurenbach, W. Zinn, Phys. Rev. B **39**, (1989) 2527.

[9] A. Fert, Thin Solid Films **517**, (2008) 2.

[10] S. Datta, B. Das, Appl. Phys. Lett. **56**, (1990) 665-667.

[11] J. K. Furdyna, J. Appl. Phys. **64**, (1988) R29-R64.

[12] S. J. Pearton, C. R. Abernathy, D. P. Norton, A. F. Hebard, Y. D. Park, L. A. Boatner, J. D. Budai, Mat. Sci. Eng. R **40**, (2003) 137-168.

[13] M. A. Ruderman, C. Kittel, Phys. Rev. **96**, (1954) 99.

[14] K. Yosida, Phys. Rev. **106**, (1957) 893.

[15] N. W. Ashcroft, N. D. Mermin, *Solid State Physics*, Holt-Saunders, Philadelphia, (1976) 29.

[16] C. Zener, Phys. Rev. **83**, (1951) 299.

[17] K. Sato, H. Katayama-Yoshida, Jpn. J. Appl. Phys. **39**, (2000) L555.

[18] H. A. Kramers, Physica **1**, (1934) 182.

[19] P. W. Anderson, Phys. Rev. **79**, (1950) 350.

[20] J. M. D. Coey, M. Venkatesan, C. B. Fitzgerald, Nat. Mater. **4**, (2005) 173-179.

[21] V. A. Ivanov, Bull. Russ. Acad. Sci. Phys. **71**, (2007) 1610-1612.

[22] T. Dietl, H. Ohno, Mater. Res. Soc. Bull. **28**, (2003) 714.

[23] J. M. D. Coey, J. Curr. Opin. Solid State Mater. Sci.**10**, (2006) 83.

[24] V. A. Ivanov, E. A. Ugolkova, O. N. Pashkova, V. P. Sanygin, A. G. Padalko, J Magn. Magn. Mater. **300**, (2006) e32-e36.

[25] C. Liu, Fi Yun, and H. Morkoc, J. Mater. Sci.: Mater. Electron. **16**, (2005): 555-597.

[26] A. J. Blattner, J. Lensch, B. W. Wessels, J. Elec. Mater. **30**, (2001) 1408.

[27] Y. Ohno, D. K. Young, B. Beschoten, F. Matsukura, H. Ohno, D. D. Awschalom, Nat. 402 (1999) 790-792.

[28] S. Sonoda, S. Shimizu, T. Sasaki, Y. Yamamoto, H. Hori, J. Cryst. Growth **237**, (2002) 1358-1362.

[29] R. Frazier, G. Thaler , M. Overberg , B . Gila, C. R. Albernathy, S. J. Pearton, Appl. Phys. Lett. **83**, (2003) 1758.

[30] H. X. Liu, S. Y. Wu, R. K. Singh, L. Gu, D. J. Smith , N. Newman, M. R. Dilley, L. Montes, M. B. Simmonds, Appl. Phys. Lett. **85**, (2004) 4076.

[31] S. E. Park, H. J. Lee, Y. C. Cho, S .Y. Jeong, C. R. Cho, S. Cho, Appl. Phys. Lett. **80,** (2002) 4187.

[32] H. X. Liu, S. Y. Wu, R. K. Singh, L. Gu, D. J. Smith , N. Newman, M. R. Dilley, L. Montes, M. B. Simmonds, Appl. Phys. Lett. **85**, (2004) 4076.

[33] J. S. Lee, J. D. Lim, Z. G. Khim, Y. D. Park, S. J. Pearton, S . N. G.Chu, J. Appl. Phys. 93 (2003) 4512.

[34] Y. Shon, Y. H. Kwon, Y. S. Park, S. U., Yuldashev, S. J. Lee, C. S. Park, H. T. Oh, J. Appl. Phys. **95**, (2003) 761-763.

[35] R. P. Davies, C. R. Abernathy, S. J. Pearton, D. P. Norton, M. P. Ivill, F. Ren, J. Chem. Eng. Comm. **196**, (2009) 1030.

[36] S. Cho, S. Choi, S. C. Hong, Y. Kim, J. B. Ketterson, B. J. Kim, Y. C. Kim, J. H. Jung, Phys. Rev. B **66**, (2002) 133313.

[37] Y. Matsumoto, M. Murakami, T. Shono, T. Hasegawa, T. Fukumura, M. Kawasaki, P. Ahmet,T. Chikyow, S. Koshihara, H. Koinuma, Science **291**, (2001) 854.

[38] H. J. Lee, S. Y. Jeong, C. R. Cho, C. H. Park, Appl. Phys. Lett. **81**, (2002) 4020.

[39] H. Ohno, Science **281**, (1998) 951.

[40] R. Beaulac, P. I. Archer, S. T. Ochsenbein, D. R. Gamlin, Adv. Funct. Mater. **18**, (2008) 3873.

[41] S. Delikanli, S. He, Y. Qin, P. Zhang, H. Zeng, H. Zhang, M. Swihart, Appl. Phys. Lett. **93**, (2008) 132501.

[42] A. D. Lad, C. Rajesh, J. Appl. Phys **101**, (2007) 103906.

[43] S. Sambasivam, D. Pauljoseph, J. G. Lin, C. Venkateswaran, J. Solid State Chem. **182**, (2009) 2598.

[44] K. Y. Ko, M. G. Blamire, Appl. Phys. Lett. **88**, (2006) 172101-172101.

[45] Y. Niwayama, H. Kura, T. Sato, M. Takahashi, T. Ogawa, Appl. Phys. Lett. **92**, (2008) 202502.

[46] R. R. Galazka, Proc. 14th Int. Conf. on Physics of Semiconductors, Inst. Phys. Conf. Ser. 43, edited by B.L.H. Wilson (Institute of Physics, Bristol, 1978) p. 133.

[47] J. K. Furdyna, J. Appl. Phys. **53**, (1982) 7637.

[48] J. K. Furdyna, J. Vac. Sci. Technol. **4**, (1986) 2002.

[49] X. Wang, Y. Li, Chem. Comm. **(28)**, (2007) 2901-2910.

[50] G. Demazeau, J. Mater. Chem. **9**, (1999) 15-18.

[51] G. Demazeau, J. Mater. Sci. **43**, (2008) 2104-2114.

[52] J. Eastoe, M. J. Hollamby, L. Hudson, Adv. Colloid. Interface. Sci. **128**, (2006) 5-15.

[53] M. A. Lopez-Quintela, Curr. Opin. Colloid Interface Sci. **8**, (2003) 137-144.

[54] J. D. Mackenzie, E. P. Bescher, Acc. Chem. Res. **40**, (2007) 810-818.

[55] C. B. Murray, S. Sun, W. Gaschler, H. DoyLe, T. A. Betley, C. R. Kagan, IBM J. Res. Dev. **45**, (2001) 47-56.

[56] Y. Yin, A. P. Alivisatos, Nature **437**, (2005) 664-670.

[57] G. Cao, D. Liu, Adv. Colloid Interface Sci. **136**, (2008) 45-64.

[58] A. Huczko, Appl. Phys. A **70**, (2000) 365-376.

[59] I. Bilecka, M. Niederberger, Nanoscale **2**, (2010) 1358-1374.

[60] B. Vaidhyanathan, D. K. Agrawal, T. R. Shrout, Y. Fang, Mater. Lett. **42** (2000) 207-211.

[61] F. V. Mikulec, M. Kuno, M. Bennati, D. A. Hall, R. G. Griffin, M. G. Bawendi, J. Am. Chem. Soc. **122**, (2000) 2532.

[62] K. M. Hanif, R. W. Meulenberg, G. F. Strouse, J. Am. Chem. Soc. **124**, (2002) 11495.

[63] W. B. Jian, J. Fang, T. Ji, Appl. Phys. Lett. **83**, (2003) 3377.

[64] R. W. Meulenberg, T. V. Buuren, K. M. Hanif, T. M. Willey, G. F. Strouse, L. J. Terminello, Nano Lett. **4**, (2004) 2277.

[65] D. Magana, S. C. Perera, A. G. Harter, N. S. Dalal, G. F. Strouse, J. Am. Chem. Soc. **128**, (2006) 2931.

[66] P. I. Archer, S. A. Santangelo, D. R. Gamelin, Nano Lett. **7**, (2007) 1037.

[67] S. B. Singh, M. V. Limaye, S. K. Date, S. K. Kulkarni, J. Chem. Phys. Lett. **464**, (2008) 208.

[68] M. S. Seehra, P. Dutta, S Neeleshwar, Y. Y Chen, C. L. Chen, S. W. Chou, C. C. Chen, C. L. Dong, C. L. Chang, J. Adv. Mater. **20**, (2008) 1656.

[69] A. Sundaresan, C.N.R. Rao, Nano Today **4**, (2009) 96.

[70] S. B. Singh, M. V. Limaye, S. K. Date, S. Gokhle, S. K. Kulkarni, J. Phys. Rev. B **80**, (2009) 235421.

[71] S. Kumar, S. Kumar, N. K. Verma, S. K. Chakarvarti, J. Mater Sci: Mater. Electron. **22**, (2011) 901-904.

[72] R. W. Meulenberg, J. R. I. Lee, S. K. McCall, D. Haskel, J. C. Lang, L. J. Terminello, T. V. Buuren, J. Electrochem. Soc. **28** (2010) 203.

[73] L. Jun, C. Li, L. Yu, D. H. Ning, Z. R. Lun, J. Chin. Phys. B **19** (2010) 037103.

[74] W. Zheng, G. F. Strouse, J. Am. Chem. Soc. **133**, (2011) 7482-7489.

[75] Z. Li, A. J. Du, Q. Sun, M. Aljada, L. N. Cheng, M. J. Riley, Z. H. Zhu, Z. X. Cheng, X. L. Wang, J. Hall, E. Krausz, S. Z. Qiao, S. C. Smith, G. Q. M. Lu, Chem. Commun. **47**, (2011) 11894-11896.

[76] S. Kumar, S. Kumar, N. K. Verma, S. K. Chakravarti, J. Mater. Sci.: Mater. Electron. **22**, (2011) 1456-1459.

[77] R. Fainblat, J. Frohleiks, F. Muckel, J. H. Yu, J. Yang, T. Hyeon, G. Bacher, Nano lett. **12**, (2012) 5311-5317.

[78] S. Kumar, T. Nann, Small **2**, (2006) 316-329.

[79] S. Kumar, N. K. Verma, M. L. Singla, J. Mater. Res. **28**, **(**2013) 521-528.

[80] P. Kaur, M. S. Shin, A. Joshi, N. Kaur, N. Sharma, J. S. Park, S. S. Sekhon, J. Phys. Chem. B **117**, (2013) 3161-3166.

[81] C. N. R., Rao, A. Müller, A. K. Cheetham, (Eds.), *The chemistry of nanomaterials: synthesis, properties and applications*, John Wiley & Sons **1**, (2006).

[82] C. M. Cheng, K. C. W. Wu, Sci. Technol. Adv. Mater. **14**, (2013) 040301.

[83] N. Suri, K. S. Bindra, M. Ahmad, J. Kumar, R. Thangaraj, Appl. Phys. A **90**, (2008) 149-151.

[84] N. Singh, A. Agarwal, S. Sanghi, P. Singh, J. Magn. Magn. Mater. **323** (2011) 486-492.

[85] L. Zhao, L. Hu, X. Fang, Adv. Fun. Mater. **22**, (2012) 1551-1566.

[86] N. Matsumura, H. Endo, J. Saraie, Phys. Status Solidi (b) **229**, (2002) 1039-1042.

[87] A. B. Kashyout, H. Soliman, M. Fathy, E. A. Gomaa, A. A. Zidan, Int. J. Photoenergy **2012**, (2012) 952610.

[88] J. M. Klostranec, W. C. Chan, Adv. Mater. **18**, (2006) 1953-1964.

[89] C. Ma, Z. L. Wang, Adv. Mater. **17**, (2005) 2635-2639.

[90] X. Jiang, B. Mayers, T. Herricks, Y. Xia, Adv. Mater. **15**, (2003) 1740-1743.

[91] Y. Zhang, Y. Tang, K. Lee, M. Ouyang, Nano Lett. **9**, (2008) 437-441.

[92] L. Manna, E. C. Scher, A. P. Alivisatos, J. Am. Chem. Soc. **122**, (2000) 12700-12706.

[93] http://www.nanoshel.in/quantum-dots.html (last accessed on 21/12/2013)

[94] http://en.wikipedia.org/wiki/Cadmium_selenide (last accessed on 21/12/2013)

[95] http://en.wikipedia.org/wiki/File:Wurtzite_polyhedra.png (last accessed on 21/12/2013)

[96] http://en.wikipedia.org/wiki/File:Sphalerite-unit-cell-depth-fade-3D-balls.png (last accessed on 21/12/2013)

[97] T. Trindade, P. O'Brien, N. L. Pickett, Chem. Mater. **13**, (2001) 3843-3858.

[98] M. Chen, L. Gao, J. Am. Ceram. Soc. **88**, (2005) 1643-1646.

[99] Y. Liu, H. Y. Qiu, Y. Xu, D. Wu, M. J. Li, J. X. Jiang, G. Q. Lai, J. Nanopart. Res. **9**, (2007) 745-752.

[100] J. V. Williams, C. N. Adams, N. A. Kotov, P. E. Savage, Ind. Eng. Chem. Res. **46**, (2007) 4358-4362.

[101] B. Gao, C. Shen, S. Yuan, Y. Yang, G. Chen, J. Nanomater. **2013**, (2013) 138526

[102] A. L. Rogach, A. Kornowski, M. Gao, A. Eychmüller, H. Weller, J. Phys. Chem. B **103**, (1999) 3065-3069.

[103] G. Demazeau, J. Mater. Sci. **43**, (2008) 2104-2114.

[104] M. N. Kalasad, M. K. Rabinal, B. G. Mulimani, Langmuir **25**, (2009)12729-12735.

[105] C. R. Bullen, P. Mulvaney, Nano Lett. **4**, (2004) 2303-2307.

[106] Z. X. Deng, L. Li, Y. Li, Inorg. Chem. **42**, (2003) 2331-2341.

[107] B. D. Cullity, *Elements of X-ray Diffraction*, 2nd Ed., by Addison-Wesley (1978).

[108] L. Brügemann, E. K. Gerndt, Nucl. Instrum. Methods Phys. Res. Sect. A **531**, (2004) 292-301.

[109] A. E. Owen, *Fundamentals of UV-visible spectroscopy* (1996).

[110] http://www.nrel.gov/pv/measurements/photoluminescence_spectroscopy.html (last ccessed on 22/12/2013)

[111] http://micro.magnet.fsu.edu/optics/timeline/people/ruska.html (last accessed on 2/12/2013)

[112] http://micron.ucr.edu/public/manuals/Tem-intro.pdf (last accessed on 22/12/2013)

[113] http://www.hk-phy.org/atomic_world/tem/tem02_e.html (last accessed on 22/12/2013)

[114] http://www.jnu.ac.in/AIRF/photogallery/tem.jpg (last accessed on 23/12/2013)

[115] http://micron.ucr.edu/public/manuals/EDS-intro.pdf (last accessed on 23/12/2013)

[116] http://www.aspexcorp.com/solutions/omegamax/edxspectroscopy.aspx (last accessed on 23/12/2013)

[117] G. Gouadec, P. Colomban, Prog. Cryst. Growth Ch. **53**, (2007) 1.

[118] http://en.wikipedia.org/wiki/File:Raman_energy_levels.svg (last accessed on 5/4/2014)

[119] http://www.americanpharmaceuticalreview.com/Featured-Articles/116920-Raman-Spectroscopy-to-Analyze-Intact-Pharmaceutical-Tablets-Factors-Influencing-MVPM-based-PAT-Methods/ (last accessed on 5/4/2014)

[120] http://nestlaboratory.com/images/contentimages/68.jpg (last accessed on 5/4/2014)

[121] E. Zavoisky, J. Phys. USSR **9**, (1945) 211.

[122] E. Zavoisky, J. Phys. USSR **9**, (1945) 245.

[123] A. Lund, M. Shiotani, S. Shimada, *Principles and applications of ESR spectroscopy*, Dordrecht, Springer 76, (2011).

[124] http://epr.cm.utexas.edu/WhatIsEPR.html (last accessed on 5/4/2014)

[125]http://www.globalspec.com/learnmore/labware_scientific_instruments/spectrometers_analytical_photometers/esrepr_spectrometers (last accessed on 5/4/2014)

[126] S. Foner, Rev. Sci. Instrum. **30**, (1959) 548-557.

[127] http://upload.wikimedia.org/wikipedia/commons/f/f2/VSM_en.svg (last accessed on 24/12/2013)

[128]http://www.lakeshore.com/Documents/The%20Performance%20of%20the%20Model%207404 00%20VSM%20Sensitivity.pdf (last accessed on 24/12/2013)

[129] http://matxrz.net/uploads/3/3/1/7/3317090/7047690.gif (last accessed on 24/12/2013)

[130] B. D. Josephson, Phys. Lett. **1**, (1962) 251-253.

[131] R. L. Fagaly, Rev. Sci. Instrum. **77**, (2006) 101101-101101.

[132] http://www.aldebaran.cz/bulletin/2006_36/squide.gif (last accessed on 24/12/2013)

[133] http://cnx.org/content/m22968/latest/graphics2.png (last accessed on 24/12/2013)

[134] http://www.uta.edu/cos/cnm/img/equipment/Quantum_Design_MPMS.jpg (last accessed on 24/12/2013)

[135] R. Adhikari, A. K. Das, D. Karmakar, T. V. C. Rao, J. Ghatak, Phys. Rev. B **78**, (2008) 024404.

[136] P. Kumar, J. P. Singh, Y. Kumar, A. Gaur, H. K. Malik, K. Asokan, Curr. Appl. Phys. **12**, (2012) 1166-1172

[137] X. Peng, L. Manna, W. Yang, J. Wickham, E. Scher, A. Kada-vanich, A.P. Alivisatos, Nature **404**, (2000) 59–61.

[138] H. Sekhar, D. N. Rao, J. Alloys Compd. **517**, (2012) 103–110.

[139] S. M. Taheri, M. H. Yousefi, A. A. Khosravi, Braz. J. Phys. **40**, (2010) 301–305.

[140] W. F. Zhang, Y. L. He, M. S. Zhang, Z. Yin, Q. Chen, J. Phys. D: Appl. Phys. **33**, (2000) 912.

[141] M. Pal, U. Pal, J. M. G. Y. Jiménez, F. Pérez-Rodríguez, Nanoscale Res. Lett. **7**, (2012) 1-12.

[142] L. Xi, Y. M. Lam, Y. P. Xu, L. J. Li, J. Colloid Interf. Sci. **320**, (2008) 491-500.

[143] M. F. Kotkata, A. E. Masoud, M. B. Mohamed, E. A. Mahmoud, Physica E Low Dimens. Syst. Nanostruct. **41**, (2009) 640-645.

[144] C. E. M. Campos, J. C. De Lima, T. A. Grandi, K. D. Machado, P. S. Pizani, Solid Stat. Commun. **123**, (2002) 179-184.

[145] O. D. Jayakumar, H. G. Salunke, R. M. Kadam, M. Mohapatra, G. Yaswant, S. K. Kulshreshtha, Nanotechnol. **17**, (2006) 1278.

[146] D. Karmakar, S. K. Mandal, R. M. Kadam, P. L. Paulose, A. K. Rajarajan, T. K. Nath, A. K. Das, I. Dasgupta, G. P. Das. Phys. Rev. B **75**, (2007) 144404.

[147] R. Saleh, S. P. Prakoso, A. Fishli, J. Magn. Magn. Mater. **324**, (2012) 665-670.

[148] D. J. Chadi, R. M. White, W. A. Harrison, Phys. Rev. Lett. **35**, (1975) 1372–1375.

[149] R. W. Mulenberg, J. R. I. Lee, S. K. MvCall, K. M. Hanif, D. Haskel, J. C. Lang, L. J. Terminello, T. van Buuren, J. Am. Chem. Soc. **131**, (2009) 6888–6889.

[150] S. K. S. Patel, S. Kurian, N. S. Gajbhiye, AIP Adv. **2**, (2012) 012107.

[151] Y. Xie, L. Zhu, X. Jiang, J. Lu, X. Zheng, W. He, Y. Li, Chem. Mater. **13**, (2001) 3927–3932.

[152] G. K. Williamson, W. H. Hall, Acta Metall. **1**, (1953) 22.

[153] Q. Wang, D. Pan, S. Jiang. X. Ji, L. An, B. Jiang, J. Cryst. Growth **286**, (2006) 83.

[154] X. Peng, J. Wickham, A. P. Alivisatos, J. Am. Chem. Soc. **120**, (1998) 5343.

[155] Y. Jin, Q. Cui, K. Wang, J. Hao, Q. Wang, J. Zhang, J. Appl. Phys. **109**, (2011) 053521.

[156] M. V. Limaye, S. B. Singh, R. Das, P. Poddar, S. K. Kulkarni, J. Solid State Chem. **184**, (2011) 391.

[157] A. I. Ekimov, F. Hache, M. C. Schanneklein, D. Ricard, C. Flytzanis, I. A. Kudryavtsev, T. V. Yazeva, A. V. Rodina, A. L. Efros, J. Opt. Soc. Am. B **10**, (1993) 100.

[158] M. G. Bawendi, P. J. Carroll, W. L. Wilson, L. E. Brus, J. Chem. Phys. **96**, (1992) 946.

[159] J. Hasanzadeh, S. F. Shayesteh, Optica Applicata. **XLI**, (2011) 921.

[160] C. E. M. Campos, J. C. de Lima, T. A. Grandi, K. D. Machado, P. S. Pizani, Phys. B: Condens. Matt. **324**, (2002) 409-418.

[161] M. Luo, Y. Jiang, C. Xu, X. Yang, A. Burger, N. C. Giles. J. Phys. Chem. Solids **67**, (2006) 2596-2602.

[162] A. Manivannan, G. Glaspell, P. Dutta, M. S. Seehra, J. Appl. Phys. **97**, (2005) 10D325.

[163] L. Saravanan, A. Pandurangan, R. Jayavel, J. Nanopart. Res. **13**, (2011) 1621.

[164] S. Furuseth, A. Kjekshus, J. Acta Chem. Scand. **23**, (1969) 2325.

[165] X. Zhang, J. Zhang, J. Zhao, B. Pan, M. Kong, J. Chen, Y. Xie, J. Am. Chem. Soc. **134**, (2012) 11908.

[166] M. Elango, D. Nataraj, K. Prem Nazeer, M. Thamilselvan. Mater. Res. Bull. **47**, (2012) 1533

[167] M. Thambidurai, N. Muthukumarasamy, S. Agilan, N. Sabari Arul, N. Murugan, R. Balasundaraprabhu. J. Mater. Sci. **46**, (2011) 3200.

[168] G. Kortüm, *Reflectance Spectroscopy: Principles, Methods, Application*, New York, Springer (1969).

[169] A.I. Ekimov, F. Hache, M. C. Schanne-Klein, D. Ricard, Christopher Flytzanis, I. A. Kudryavtsev, T. V. Yazeva, A. V. Rodina, A. L. Efros, J. Opt. Soc. Am. B **10,** (1993) 100.

[170] V. Babentsov, J. Riegler, J. Schneider, O. Ehlert, T. Nann, M. Fiederle, J. Cryst. Growth, **280,** (2005) 502.

[171] P. H. Borse, N. Deshmukh, R. F. Shinde, S. K. Date, S. K. Kulkarni, J. Mater. Sci. **34,** (1999) 6087.

[172] C. Y. Xu, P. X. Zhang, L. Yan. J. Raman Spectrosc. **32**, (2001) 862-865.

[173] A. J. Sievers, S. Takeno, Phys. Rev. Lett. **61,** (1998) 970.

[174] J. A. Weil, J. R. Bolton, J. E. Wertz, *Electron Paramagnetic Resonance: Elementary Theory and Practical Applications*, Wiley, New York, (1994).

[175] R. H. Kodama, S.A. Makhlouf, A.E. Berkowitz, Phys. Rev. Lett. **79,** (1997) 1393.

[176] X. He, W. Zhong, C.T. Au, Y. Du, Nanoscale Res. Lett. **8,** (2013) 446.

[177] A. K. Mishra, D. Das, Mater. Sci. Eng. B **171,** (2010) 5.

[178] L. F. Xi, Y. M. Lam, J. Colloid Interf. Sci. **316**, (2007) 771-778.

[179] R. Sethi, L. Kumar, P. K. Sharma, A. C. Pandey. Nanoscale Res. Lett. **5**, (2010): 96-102.

[180] G. Scamarcio, M. Lugara, D. Manno, Phys. Rev. B **45,** (1992) 13792.

[181] J. Y. Zhang, X.Y. Wang, M. Xiao, L. Qu, X. Peng, Appl. Phys. Lett. **81,** (2002) 2076.

[182] A. J. Mayur, M. D. Sciacca, H. Kim, I. Miotkowski, A. K. Ramdas, S. Rodriguez, G. C. La Rocca, Phys. Rev. B **53,** (1996) 12884.

[183] A. Singhal, S. N. Achary, J. Manjanna, O. D. Jayakumar, R. M. Kadam, A. K. Tyagi, J. Phys. Chem. C **113,** 3600 (2009)

[183] S. Sambasivam, B. K. Reddy, A. Divya, N. Madhusudhana Rao, C. K. Jayasankar, B. Sreedhar, Phys. Lett. A **373**, (2009) 1465.

[184] W. L. Roth, Phys. Rev. **110,** (1958) 1333.

[185] K. Woo, J. Hong, S. Choi, H.W. Lee, J.P. Ahn, C. Kim, S.W. Lee, Chem. Mater. **16**, (2004) 2814.

[186] A. Fouchet, W. Prellier, P. Padhan, C. Simon, B. Mercey, V. N. Kulkarni, T. Venkatesan, J. Appl. Phys. **95**, (2004) 7187.

[187] H. Kimura, T. Fukumura, M. Kawasaki, K. Inaba, T. Hasegawa, H. Koinuma, Appl. Phys. Lett. **80**, (2002) 94-96.

[188] C. Van Komen, A. Thurber, K. M. Reddy, J. Hays, A. Punnoose, J. Appl. Phys. **103**, (2008) 07D141-07D141.

[189] B. Santara, B. Pal, P. K. Giri, J. Appl. Phys. **110**, (2011) 114322-114322.

[190] J. Hays, K. M. Reddy, N. Y. Graces, M. H. Engelhard, V. Shutthanandan, M. Luo, C. Xu, N. C. Giles, C. Wang, S. Thevuthasan, A. Punnoose, J. Phys: Condens. Matt. **19**, (2007) 266203.

[191] J. Hays, A. Punnoose, R. Baldner, M. H. Engelhard, J. Peloquin, K. M. Reddy, Phys. Rev. B **72** (2005) 075203.

[192] Thurber, A. Reddy, K. M. Shutthanandan, V. Engelhard, M. H. Wang, C. Hays, J.

Punnoose, A. Phys. Rev. B **76**, (2007) 165206.

[193] F. Ahmed, N. Arshi, M.S. Anwar, S.H. Lee, E.S. Byon, N.J. Lyu, B.H. Koo, Curr. Appl. Phys. **12,** (2012) S174-S177.

[194] Q. Sun, Y. Zeng, D. Jiang, Cryst. Eng. Comm. **14**, (2012) 713-718.

[195] S. Kumar, C. L. Chen, C. L. Dong, Y. K. Ho, J. F. Lee, T. S. Chan, R. Thangavel, T. K. Chen, B. H. Mok, S. M. Rao, M. K. Wu, J. Alloy. Compd. **554**, (2013) 357-362.

[196] S. V. Bhat, F. L. Deepak, Solid Stat. Comm. **135**, (2005) 345-347.

[197] B. Poornaprakash, S. Sambasivam, D. Amaranatha Reddy, G. Murali, R. P. Vijayalakshmi, B. K. Reddy. Ceram. Int. **40,** (2014) 2677-2684.

[198] A. Bouaine, N. Brihi, G. Schmerber, C. Ulhaq-Bouillet, S. Colis, and A. Dinia, J. Phys. Chem. C. **111**, (2007) 2924-2928.

[199] S. Das, A. Dutta, S. Banerjee, T. P. Sinha, Mater. Sci. Semicond. Process. **18**, (2014) 152-159.

[200] S. Thota, T. Dutta, J. Kumar, J. Phys.: Condens. Matt. **18,** (2006) 2473.

[201] S. K. Misra, S. I. Andronenko, M. H. Engelhard, A. Thurber, K. M. Reddy, A. Punnoose, J. Appl. Phys. **103**, (2008) 07D122.